

# **A Measurement of the Neutrino Magnetic Moment at the Bugey Nuclear Reactor**

**Dissertation**

zur

Erlangung der naturwissenschaftlichen Doktorwürde  
(Dr. sc. nat.)

vorgelegt der

Mathematisch-naturwissenschaftlichen Fakultät

der

Universität Zürich

von

**Oliver Link**

von

Zürich ZH

Begutachtet von

**Prof. Dr. Claude Amsler**

**Prof. Dr. Jean-Luc Vuilleumier**

Zürich 2003

Die vorliegende Arbeit wurde von der Mathematisch-naturwissenschaftlichen Fakultät der Universität Zürich auf Antrag von Prof. Dr. C. Amsler als Dissertation angenommen.

## *SUMMARY*

The aim of the MUNU experiment is the measurement of the neutrino magnetic moment. For this purpose, we have built a detector close to the core of the Bugey nuclear reactor, which is an intense source of low energy antineutrinos. The low background detector consists of a time projection chamber for the electron tracking, surrounded by an active shielding to veto cosmic muons and Compton events, and a passive shielding against neutrons and  $\gamma$ -rays. We measured 66 days with reactor ON, and the background isotropy was controlled in the following 19 days during the reactor shutdown.

An algorithm for the reconstruction of the electron track, its angle, its energy and the precise neutrino-electron interaction point was developed and tested with real and simulated data. The data collected at the reactor were then processed with this code.

The measured electron recoil spectrum and the angular distribution of the scattering angle are presented. The result is in good agreement with weak interaction and there is no indication for a finite neutrino magnetic moment. An upper limit on the neutrino magnetic moment of  $1.7 \cdot 10^{-10} \mu_B$  was derived at a 300 keV detection threshold.



## ZUSAMMENFASSUNG

Das Ziel des MUNU Experiments ist die Messung des magnetischen Moments von Neutrinos. Zu diesem Zweck wurde ein Detektor in der Nähe des Kerns des nuklearen Reaktors in Bugey gebaut, welcher eine intensive Quelle an niederenergetischen Neutrinos ist. Der Detektor besteht aus einer Zeitprojektionskammer, und ist umgeben von einer aktiven Abschirmung gegen kosmische Muonen und Compton Ereignissen, und von einer passiven Abschirmung gegen Neutronen und  $\gamma$ -Strahlung. Wir haben 66 Tage mit Reaktor ON gemessen, und die Isotropie des Untergrunds wurde in den 19 darauf folgenden Tagen der Reaktor Abschaltung kontrolliert.

Ein Algorithmus für die Rekonstruktion der Spur von Elektronen, ihrer Winkel, ihrer Energie und ihres genauen Neutrino-Elektron Wechselwirkungspunkts wurde entwickelt und getestet mit realen und simulierten Daten. Die am Reaktor gesammelten Daten wurden anschliessend mit dem Programm rekonstruiert.

Das gemessene Spektrum der gestreuten Elektronen und die Winkelverteilung des Streuwinkels werden vorgestellt. Das Resultat ist in guter Übereinstimmung mit der schwachen Wechselwirkung und es wurde kein Hinweis auf ein endliches magnetisches Moment festgestellt. Ein oberes Limit für das magnetische Moment des Neutrinos von  $1.7 \cdot 10^{-10} \mu_B$  wurde bei einer Detektionsschwelle von 300 keV erhalten.



## CONTENTS

<b>1</b>	<b>Introduction</b>	<b>1</b>
1.1	Elastic $\bar{\nu}_e e^-$ scattering . . . . .	2
1.2	Previous experiments . . . . .	8
<b>2</b>	<b>The Munu Experiment</b>	<b>11</b>
2.1	The MUNU detector . . . . .	11
2.1.1	Time Projection Chamber . . . . .	12
2.1.1.1	Drift gas $\text{CF}_4$ . . . . .	15
2.1.1.2	Drift region . . . . .	16
2.1.1.3	Signal amplification . . . . .	16
2.1.2	Active shielding: Anti-Compton . . . . .	17
2.1.3	Passive shielding: Lead and borated polyethylene . . . . .	18
2.1.4	Background and radiochemical purity . . . . .	19
2.2	The trigger of the MUNU experiment . . . . .	19
2.2.1	Neutrino hardware trigger . . . . .	20
2.2.2	Online filter against electrical discharges . . . . .	21
2.2.3	Summary . . . . .	23
2.3	The data acquisition . . . . .	23
2.3.1	VME crate and main control . . . . .	24
2.3.2	Flash-ADC crates to digitize signals at high speed . . . . .	24
2.3.3	NIM crate to convert and forward the hardware trigger . . . . .	25

2.3.4	CAMAC crate for the trigger system and dead time measurement . . . . .	26
2.3.5	Run control . . . . .	26
2.4	Typical events in the MUNU experiment . . . . .	27
<b>3</b>	<b>Offline filtering and calibration</b>	<b>31</b>
3.1	Offline Filtering . . . . .	31
3.1.1	Asymmetry filter against electrical discharges . . . . .	33
3.1.2	Filter against electrons crossing the anode plane . . . . .	33
3.1.3	Veto against electrons from Compton scattering . . . . .	36
3.1.4	Containment filter . . . . .	37
3.1.5	Accepted events . . . . .	38
3.1.6	Summary and conclusion . . . . .	39
3.2	Detector calibration and slow-control . . . . .	39
3.2.1	Energy calibration . . . . .	40
3.2.2	Drift time in the TPC and z-bin conversion . . . . .	41
3.2.3	Determination of dead time . . . . .	42
3.2.4	Measurement of the electron density . . . . .	43
3.2.5	Thermal reactor power . . . . .	44
<b>4</b>	<b>Track reconstruction</b>	<b>47</b>
4.1	Automatic tracking . . . . .	48
4.1.1	Event region finding . . . . .	48
4.1.2	Iterative reconstruction of the trajectory . . . . .	48
4.1.3	Vertex reconstruction . . . . .	52
4.1.4	Spatial resolution of the vertex . . . . .	54
4.2	Angular fit in 3D . . . . .	55
4.2.1	Boundaries and convergence of the fit . . . . .	56
4.2.2	Peaks in the $\phi_{\text{det}}$ distribution . . . . .	57
4.2.3	Angular resolution in space . . . . .	58
4.2.4	Energy dependence of the angular resolution . . . . .	59

---

4.2.5	Anisotropy of the angular resolution . . . . .	59
4.2.6	Reconstruction of the scattering angle $\theta$ . . . . .	61
4.3	Real data angular distributions . . . . .	63
4.4	Discussion . . . . .	65
<b>5</b>	<b>Monte Carlo</b> . . . . .	<b>69</b>
5.1	The Monte Carlo simulation . . . . .	69
5.1.1	Event generation . . . . .	71
5.1.1.1	Antineutrinos from a nuclear reactor . . . . .	71
5.1.1.2	Antineutrino energy spectrum . . . . .	73
5.1.1.3	Counting rate prediction . . . . .	74
5.1.2	Track simulation with GEANT . . . . .	75
5.1.3	Track digitisation . . . . .	77
5.2	Acceptance of the automatic tracking . . . . .	77
5.3	Discussion . . . . .	81
<b>6</b>	<b>Data Analysis</b> . . . . .	<b>83</b>
6.1	Event selection . . . . .	83
6.1.1	Hardware trigger and online filtering . . . . .	83
6.1.2	Offline filtering . . . . .	84
6.1.3	Track reconstruction and kinematic cut . . . . .	85
6.2	Isotropy of the background: Reactor OFF . . . . .	85
6.3	Analysis of reactor ON data . . . . .	88
6.3.1	Forward minus backward comparison . . . . .	88
6.3.2	Upper limit on the neutrino magnetic moment . . . . .	89
6.3.3	Total cross section measurement . . . . .	93
6.4	Conclusions . . . . .	94

---

<b>A</b>	<b>Counting rates</b>	<b>97</b>
A.1	Anti Compton . . . . .	97
A.2	The neutrino hardware trigger . . . . .	99
A.3	Compton electrons . . . . .	100
A.4	Electrons crossing the anode . . . . .	102
A.5	Electrons outside the containment . . . . .	104
<b>B</b>	<b>Parameter optimisation</b>	<b>107</b>
B.6	Step size: RSTEP . . . . .	108
B.7	Length of the rotating box: RLENGTH . . . . .	109
B.8	Reconstruction threshold: IXYCUT . . . . .	110
B.9	Fit radius: RCIRCLE . . . . .	112
<b>C</b>	<b>Visual Scanning</b>	<b>113</b>
C.10	Comparison between the eye and the automatic classification	113
C.10.1	Electrons outside the containment . . . . .	113
C.10.2	Electrons inside the containment . . . . .	115
C.11	Angular distributions . . . . .	116
C.12	Filtering for the visual scanning . . . . .	119
<b>D</b>	<b>Bibliography</b>	<b>123</b>
	<b>Acknowledgement</b>	<b>127</b>
	<b>Curriculum Vitae</b>	<b>129</b>

*Introduction*

The neutrino is a unique probe for particle physics and cosmology. There are three kinds of light neutrinos  $\nu_e$ ,  $\nu_\mu$  and  $\nu_\tau$ , corresponding to the three leptons  $e^-$ ,  $\mu^-$  and  $\tau^-$ . Each flavour state  $\nu_e$ ,  $\nu_\mu$  and  $\nu_\tau$  is a superposition of the mass eigenstates  $\nu_1$ ,  $\nu_2$  and  $\nu_3$ . As the latter do not have the same mass, there must be an oscillation of the three neutrino flavours, described by the Pontecorvo MNS mixing matrix  $U$ .

$$U = \begin{pmatrix} 1 & 0 & 0 \\ 0 & c_{23} & s_{23} \\ 0 & -s_{23} & c_{23} \end{pmatrix} \begin{pmatrix} c_{13} & 0 & s_{13}e^{-i\delta} \\ 0 & 1 & 0 \\ -s_{13}e^{i\delta} & 0 & c_{13} \end{pmatrix} \begin{pmatrix} c_{12} & s_{12} & 0 \\ -s_{12} & c_{12} & 0 \\ 0 & 0 & 1 \end{pmatrix}$$

For flavour oscillation, we have three mixing angles and one phase. The mixing angles are an important intrinsic property of the neutrinos. The last matrix describes the  $\nu_e$  to  $\nu_\mu$  oscillation, hence the physics of the solar neutrino problem. The first matrix is important for atmospheric oscillation between  $\nu_\mu$  and  $\nu_\tau$ , and can be measured with long-baseline (LBL) beam experiments. The second matrix is interesting for the disappearance channel  $\nu_e$  to  $\nu_\tau$ , which can be probed at reactors.

The presently solar and atmospheric neutrino data are described well with oscillation alone. A contribution from neutrino magnetic moments complicating the oscillation pattern is however possible. The observed reduction of the solar neutrino flux of  $\nu_e$  could be explained by a helicity flip of the neutrino due to the interaction of the magnetic moment with the solar magnetic field. The resulting sterile right-handed neutrino  $\nu_R$  is not detectable, leading to a reduction of the observable neutrino flux from the sun. The existence of the neutrino magnetic moment is only possible for massive neutrinos, however. In the SM, the neutrino magnetic moment is proportional to the neutrino mass, see ref. [1]:

$$\mu_\nu = \frac{3m_e G_F}{4\pi^2 \sqrt{2}} m_\nu \mu_B \simeq 3.2 \times 10^{-19} \left( \frac{m_\nu}{1 \text{ eV}} \right) \mu_B \quad , \quad (1.1)$$

where  $\mu_B = e\hbar/2m_e$  is the electron Bohr magneton. With the current 95% C.L. upper limit for the Neutrino mass,  $m_\nu < 2.2 \text{ eV}$  (see ref. [2],[3]), the upper limit on the magnetic moment in the extended standard model becomes

$$\mu_\nu < 1 \times 10^{-18} \mu_B \quad .$$

The present experiments are not able to probe this limit, but any evidence for a large neutrino magnetic moment would be an indication for new physics beyond the standard model. Informations about standard model extensions and the electromagnetic properties of neutrinos can be found in ref. [4].

However, to explain the observed deficit of solar neutrinos, the neutrino magnetic moment would have to be in the order of  $10^{-9}$  to  $10^{-12} \mu_B$ . This was the motivation of the MUNU experiment, see 1992[5].

### 1.1 Elastic $\bar{\nu}_e e^-$ scattering

The MUNU experiment studies  $\bar{\nu}_e e^-$  elastic scattering with neutrino energies ranging up to about 10 MeV. In first order, this scattering is described by a neutral current (NC) interaction with  $Z^0$  as propagator, and a charged current (CC) interaction with a  $W$  propagator. The corresponding Feynman diagrams are shown in figure 1.1. The neutrino is not charged; hence, a coupling with the photon-field is only feasible through higher order virtual loops, containing charged leptons and bosons (the third diagram in figure 1.1). An effective scattering amplitude is the sum of the pure weak

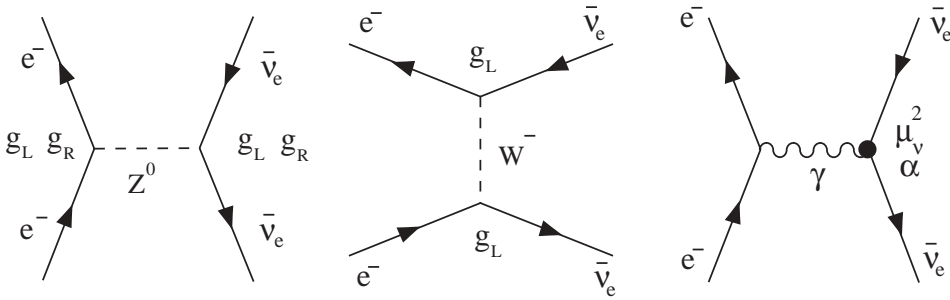


**Figure 1.1:**  $\bar{\nu}_e e^-$  elastic scattering. The diagrams are from left to right: NC, CC and higher order electromagnetic coupling.

currents and the electromagnetic currents, see ref. [6]. For the differential cross section of the weak interaction, we obtain

$$\frac{d\sigma^W}{dT} = \frac{2G_F^2 m_e}{\pi} \left[ g_R^2 + g_L^2 \left( 1 - \frac{T}{E_\nu} \right)^2 - g_L g_R \frac{m_e T}{E_\nu^2} \right] \quad . \quad (1.2)$$

The differential cross section of the electromagnetic interaction is proportional to the squared neutrino magnetic moment:

$$\frac{d\sigma^M}{dT} = \frac{\pi\alpha^2}{m_e^2} \left( \frac{\mu_\nu}{\mu_B} \right)^2 \frac{1 - T/E_\nu}{T}. \quad (1.3)$$

The pure weak interaction gives a coherent contribution to the scattering, whereas the magnetic moment is incoherent. In the  $\gamma$ -exchange the neutrino undergoes a spin flip, but not in the NC and CC interactions. Therefore, there is no interference between the two contributions, and the cross sections can simply be added:

$$\frac{d\sigma}{dT} = \frac{d\sigma^W}{dT} + \frac{d\sigma^M}{dT} \quad . \quad (1.4)$$

In the formulas 1.2 and 1.3, the incident neutrino energy is denoted with  $E_\nu$  and the kinetic energy of the scattered electron with  $T$ . Further,  $G_F$  stands for the Fermi coupling constant, and  $\alpha$  for the fine-structure constant. The chiral couplings  $g_L$ ,  $g_R$  to a left, and right-handed electron respectively depend on the couplings of the electroweak interaction  $g_A$  and  $g_V$ .

$$\begin{aligned} g_L &= \frac{1}{2} [g_V + g_A], \\ g_R &= \frac{1}{2} [g_V - g_A]. \end{aligned} \quad (1.5)$$

The coupling constant  $g_V$  depends on the Weinberg angle  $\sin^2 \theta_W$ , and is given for  $\bar{\nu}_e e^-$  elastic scattering by:

$$g_V = 2 \sin^2 \theta_W + 1/2 \quad . \quad (1.6)$$

For  $\bar{\nu}_e e^-$  scattering the coupling constant  $g_A$  is -1/2. Thus, we obtain with formula (1.5) the two couplings

$$\begin{aligned} g_L &= \sin^2 \theta_W, \\ g_R &= g_L + 1 \quad . \end{aligned} \quad (1.7)$$

Let us now calculate the kinematic of the  $\bar{\nu}_e e^-$  scattering. In the MUNU experiment we measure simultaneously both the electron energy  $T$  and the scattering angle  $\theta$ , as illustrated in figure 1.2. From the conservation of the total energy-momentum vector  $p^\mu$  and the invariance of its norm, we find for  $E_\nu \gg m_\nu$  the electron energy

$$T = \frac{E_\nu^2 \cos^2 \theta}{E_\nu + m_e/2 + (E_\nu^2 \sin^2 \theta)/2m_e} \quad . \quad (1.8)$$

For electrons in the forward direction with  $\theta = 0^\circ$ , the kinetic energy  $T$  is maximal,

$$T^{max} = \frac{2E_\nu^2}{2E_\nu + m_e} \quad , \quad (1.9)$$

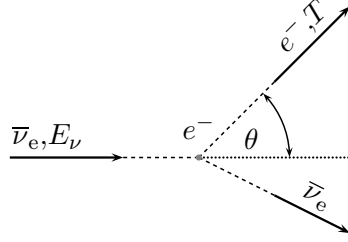


**Figure 1.2:**  $\bar{\nu}_e e^-$  - Scattering.

which reminds of the Compton edge energy in  $e\gamma$  scattering. The maximal electron energy  $T^{max}$  is 331 keV for  $E_\nu = 0.5$  MeV, 796 keV for  $E_\nu = 1$  MeV and 1.78 MeV for  $E_\nu = 2$  MeV respectively.

In figure 1.3, the differential cross sections for a weak (dotted line) and for an additional electromagnetic (solid line) interaction are shown as a function of the electron energy  $T$  for the neutrino energies  $E_\nu = 0.5, 1.0$  and  $2.0$  MeV. The differential cross sections are vanishing above the maximal electron energies  $T^{max}$ . With decreasing electron energies, the differential cross section of the electromagnetic interaction increases more compared to the weak interaction contribution. This explains why the detection of electrons with a low threshold is crucial to a good measurement.

The importance of the low detection threshold can also be understood by calculating the differential cross section versus the scattering angle  $\cos\theta$ :

$$\frac{d\sigma}{d\Omega} = \frac{d\sigma}{dT} \cdot \frac{p_e^2}{2\pi \cos\theta} \quad , \quad (1.10)$$

where  $p_e$  denotes the momentum of the recoil electron which is given by

$$p_e = \frac{2E_\nu \cos\theta m_e (E_\nu + m_e)}{(E_\nu + m_e)^2 - E_\nu^2 \cos^2\theta} \quad . \quad (1.11)$$

In figure 1.4, the differential cross sections for a weak (blue line) and for an additional electromagnetic (red line) interaction are shown as a function of  $\cos\theta$  for  $E_\nu = 0.5, 1.0$  and  $2.0$  MeV. The solid dotted lines are calculated without detection threshold on the electron energy, whereas the solid lines are calculated for a 300 keV detection threshold. At scattering angles  $\theta$  close to  $90^\circ$ , the energy of the recoil electrons decreases, and the differential cross section for the magnetic interaction increases rapidly. Therefore, a measurement of the neutrino magnetic moment is especially sensitive at large scattering angles and at low electron energies. This favours sub MeV neutrinos from a nuclear reactor.

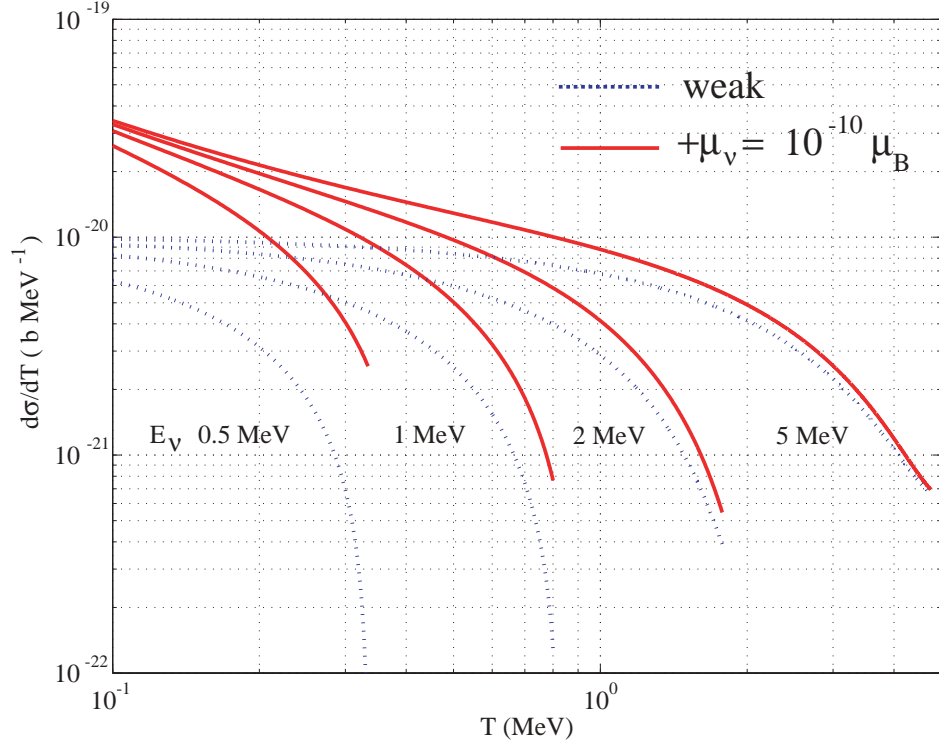


**Figure 1.3:**  $\bar{\nu}_e e^-$  differential cross section  $d\sigma/dT$  for neutrino energies  $E_\nu = 0.5, 1.0, 2.0$  and  $5.0$  MeV.

The Bugey nuclear  $^{235}\text{U}$  reactor emits  $\bar{\nu}$  between 0 and 10 MeV, produced by  $\beta$ -decay of fission products. The  $\beta$ -decay contribution from other elements is also present, but small. Figure 1.5 shows the experimentally well known (see chapter 5 for details) neutrino reactor spectrum.

For a comparison of predictions with experimental results, the differential cross section 1.4 has to be averaged with the reactor neutrino spectrum:

$$\langle \frac{d\sigma}{dT} \rangle = \int_{E_\nu^{\min}(T)}^{\infty} \frac{dN_\nu}{dE_\nu} \frac{d\sigma}{dT} dE_\nu \quad . \quad (1.12)$$

In this expression,  $E_\nu^{\min}(T)$  is the minimum energy of the neutrino at which a recoil electron with kinetic energy  $T$  can be generated:

$$E_\nu^{\min}(T) = \frac{T}{2} \left( 1 + \sqrt{1 + \frac{2m_e}{T}} \right) \quad . \quad (1.13)$$

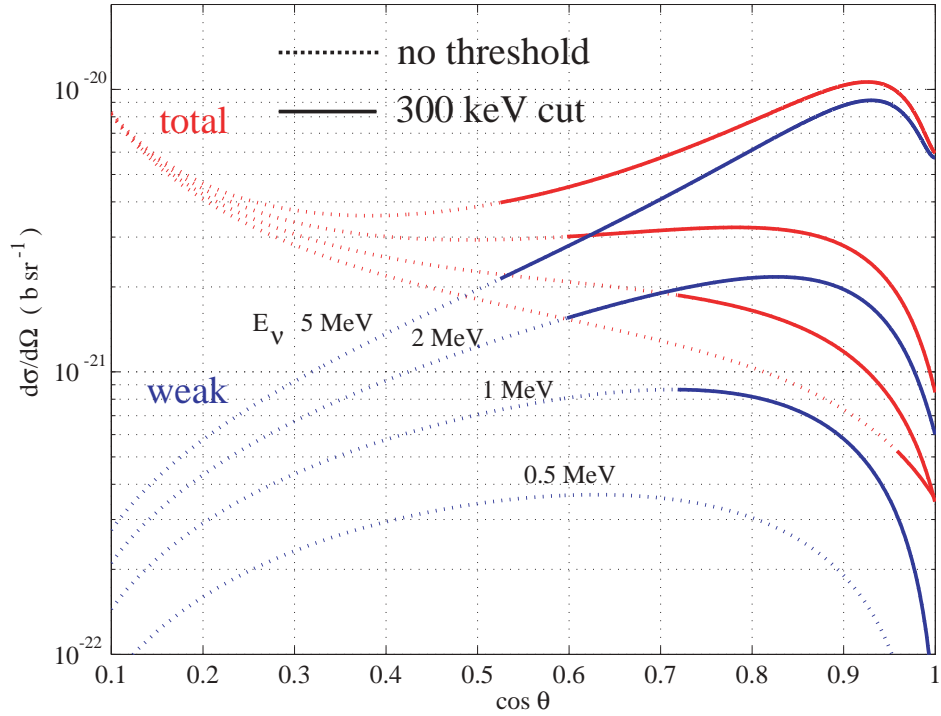


**Figure 1.4:**  $\bar{\nu}_e e^-$  differential cross section  $d\sigma/d\Omega$  for neutrino energies  $E_\nu = 0.5, 1.0, 2.0$  and  $5.0$  MeV.

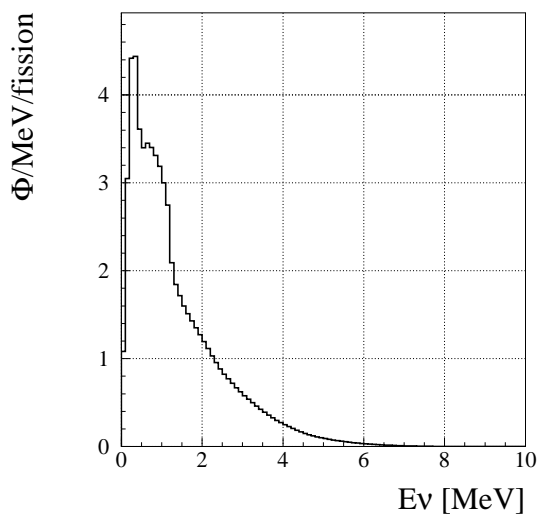


**Figure 1.5:** Antineutrino reactor flux per MeV and per fission. See section 5.1.1.2 for explanations and references.

Figure 1.6 shows the differential cross sections for the weak (dotted line)

and magnetic (solid line) interaction averaged over the spectrum of reactor neutrinos. At an energy of 320 keV, the two contributions for the magnetic moment of  $10^{-10} \mu_B$  and  $\sin^2 \theta_W$  becomes even. The steep decrease at electron energies above 1 MeV is due to the drop in the reactor antineutrino spectrum. Note that integral of the neutrino spectrum  $dN_\nu/dE_\nu$  in 1.12 corresponds to the number of neutrinos per fission, and therefore the averaged differential cross section is given in barn per MeV and per fission.

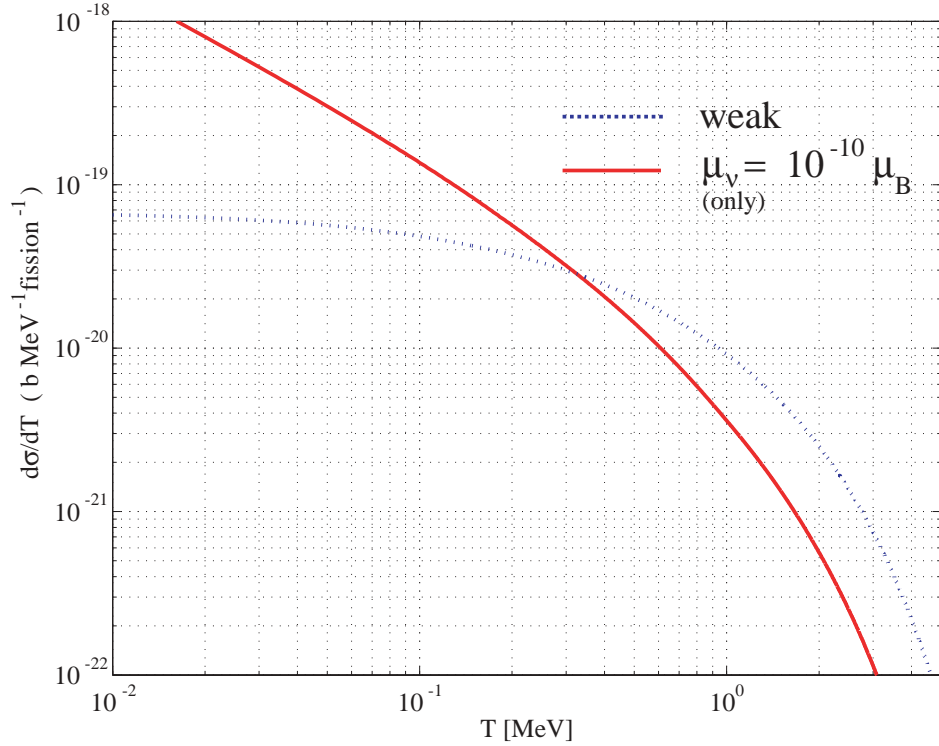


**Figure 1.6:** Differential cross section  $d\sigma/dT$  of  $\bar{\nu}_e e^-$  elastic scattering weighted with the reactor spectrum of an  $^{235}\text{U}$  reactor.

The total cross section is obtained from the averaged differential cross section by integration

$$\sigma = \int_{T_{\min}}^{T_{\max}} \left\langle \frac{d\sigma}{dT} \right\rangle dT \quad (1.14)$$

from the detection threshold  $T_{\min}$  (300 keV) to the superior limit  $T_{\max}$  (1800 keV) where the differential cross section becomes small. The cross section for the weak interaction is  $1.64 \cdot 10^{-20}$  b per fission, and  $0.95 \cdot 10^{-20}$  b per fission for the magnetic interaction. Therefore, we can calculate the total cross section for the interval 300 keV to 1800 keV as a function of the magnetic moment  $\mu_\nu^2$ :

$$\sigma = (1.64 + 0.95 \cdot \mu_\nu^2) \cdot 10^{-20} \text{ b/fission} \quad , \quad (1.15)$$

where the magnetic moment is in  $10^{-10}\mu_B$  units. This value has to be divided by the number of neutrinos per fission ( $= 6.71$ ) in order to obtain the total cross section. For instance, the total cross section for a pure weak interaction is  $2.45 \cdot 10^{-21}$  b in the interval 300 keV to 1800 keV.

## 1.2 Previous experiments

The present experiments probe the magnetic moment of the neutrino  $\bar{\nu}_e$  in the order of  $10^{-10}\mu_B$ . This value is eight orders of magnitude higher than the value predicted by the SM. The elastic scattering of an antineutrino by an electron is the most sensitive reaction to probe a nonzero magnetic moment.

The present limits are obtained by the following reactor experiments:

- $\mu_\nu = (2 - 4) \cdot 10^{-10}\mu_B$  is based on the Savannah River reactor experiment by Reines et al. [7]. The experiment used a segmented 15.9 kg plastic scintillator ( $\text{CH}_2$ ), surrounded by an 300 kg anti-Compton (NaI) to veto  $\gamma$  background, a lead passive shield and a 2000l liquid scintillator to veto cosmics. The counting rate of the inverse  $\beta$  decay reaction  $\bar{\nu}_e + p \rightarrow e^+ + n$  was 30 times higher than that for the  $\bar{\nu}_e e^-$  scattering in the electron detection range 1.5 - 4.5 MeV. Analysing the recoil electron data with an improved knowledge of the reactor spectrum, Vogel and Engel [6] found a slight excess of events, which can be explained by a magnetic moment.
- $\mu_\nu \leq 2.4 \cdot 10^{-10}\mu_B$  from  $\bar{\nu}_e e^-$  scattering, by the Kurtchatov Institute in Moscow [8] [9]. The 103 kg detector was an assembly of seven cells filled with a liquid scintillator ( $\text{C}_2\text{F}_6$ ), surrounded by shielding layers to veto and suppress background. Only the electron energy spectrum above 3.15 MeV was measured due to the high background level of natural and induced radioactivity.
- $\mu_\nu \leq 1.9 \cdot 10^{-10}\mu_B$  (95% CL) at the Rovno reactor [10]. The experiment used 600 silicon modules (in total 75 kg), surrounded by a plastic scintillator acting as an active shielding and by various passive shielding layers. Only 29.6 days with reactor ON and 16.7 days background are available, and the signal to background ratio of order 1:100 is very low. The recoil electron spectrum was measured above 600 keV.
- $\mu_\nu \leq 1.3 \cdot 10^{-10}\mu_B$  at the Kuo-Sheng reactor [11]. The experiment uses a high purity germanium detector of 1.06 kg mass, surrounded by anti-Compton detectors with NaI(Tl) and CsI(Tl) crystal scintillators. The detection threshold of the counting rate experiment is very low (12 keV). No significant difference between reactor ON and reactor OFF was observed, however.

The most stringent limits on the neutrino magnetic moment come from astrophysical observations and are in the order of  $10^{-10} - 10^{-12}\mu_B$ . These

limits are model dependent, however. The limits are obtained in the Dirac case from the fact that the scattering of neutrinos with a large magnetic moment by charged particles would lead to an intense production of right-handed neutrinos, which are sterile for the weak interaction. Alternatively for both Dirac and Majorana neutrinos, virtual plasmons can decay in  $\nu\bar{\nu}$ -pairs, which can escape from the core of a star. This leads to a cooling of the star.

- $\mu_\nu \leq 1.5 \cdot 10^{-10} \mu_B$  from the measurement of the solar neutrino spectrum ( $^8\text{B}$ ) with the Super-Kamiokande experiment [12] [13]. Only a reduction of the neutrino flux due to oscillation was observed. However, the shape of the spectra is in good agreement with the prediction of the weak interaction alone. From this, an 90% upper limit on the neutrino magnetic moment was obtained, assuming that the  $\nu$  do not oscillate.
- $\mu_\nu \leq 2 \cdot 10^{-11} \mu_B$  from the observation of the Helium abundance, see ref. [14]. The escaping sterile neutrinos would lead to a faster cooling after the Big Bang. This would enhance the nucleosynthesis of  $^4\text{He}$  of the order of 15%.
- $\mu_\nu \leq (1 - 4) \cdot 10^{-12} \mu_B$  from the neutrino burst of the supernovae SN1987A, see ref. [15]. Right-handed Dirac neutrinos could escape from the core of a collapsing star. This cools the supernovae and modifies the duration of the collapse. The limit was obtained from the duration of the neutrino pulse. The supernovae arguments only apply for Dirac neutrinos.
- $\mu_\nu \leq 2 \cdot 10^{-12} \mu_B$  from red giant luminosity, see ref. [16]. A large neutrino magnetic moment would delay helium ignition due to cooling, affecting the luminosity function of the star. The argument holds for both Dirac and Majorana neutrinos.

In the MUNU experiment, we measure the energy of the recoil electrons and the scattering angle simultaneously with a time projection chamber. This improves the sensitivity on the neutrino magnetic moment compared to experiments measuring only the energy spectrum. The upper limit obtained in this work is  $1.7 \cdot 10^{-10} \mu_B$  at a 90% confidence level, see chapter 6.

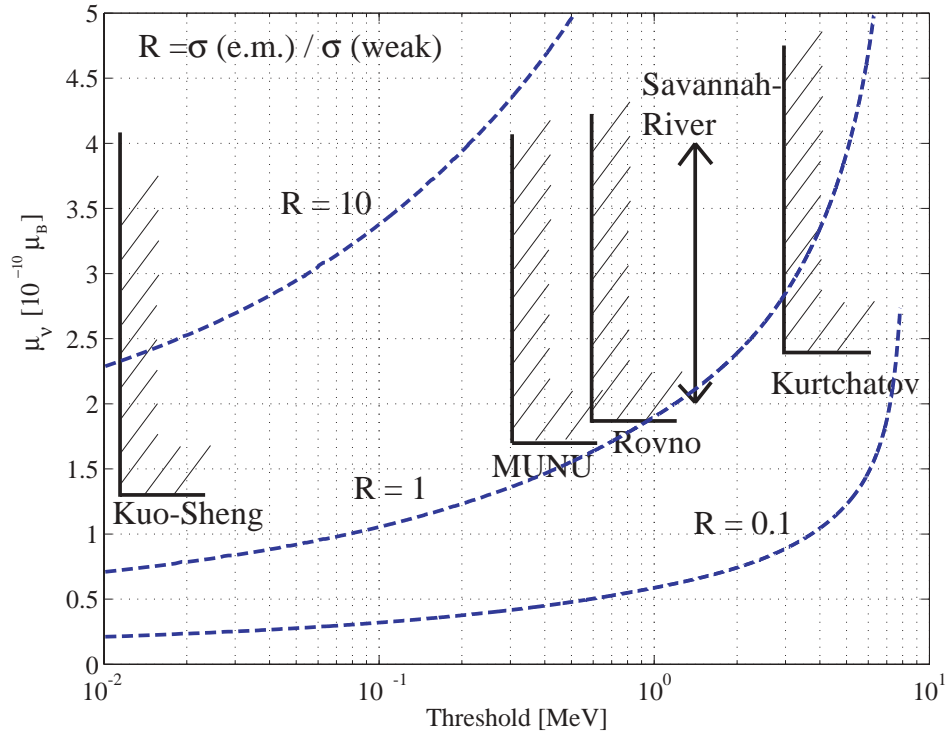
Table 1.1 summarises the present upper limits on the neutrino magnetic moment. Note, that the confidence level for reactor experiments and SKAM is 90%.

Figure 1.7 summarises the results in the  $\mu_\nu$  search with reactor neutrinos versus the electron detection threshold. The dotted lines are the  $\sigma_{\text{e.m.}}/\sigma_{\text{weak}}$  ratio  $R$  at a particular electron energy threshold  $T$  and magnetic moment  $\mu_\nu$ . The sensitivity on the magnetic moment increases with decreasing electron threshold, where the ratio  $R$  increases. The upper limit on the neutrino

**Table 1.1:** Present upper limits (see text).

$\mu_\nu [10^{-10} \mu_B]$	Comment	Reference
<i>Astrophysics and cosmology</i>		
1.5	SKAM $\nu$ spectrum shape	[12],[13]
0.2	$^4\text{He}$ abundance	[14]
0.01 – 0.04	Supernovae SN1987	[15]
0.02	Red Giant luminosity	[16]
<i>Reactor experiments (90% CL) (<math>\bar{\nu}_e e^-</math> scattering)</i>		
2-4	Savannah River	[7], [6]
2.4	Kurtchatov	[8],[9]
1.9	Rovno (95% CL)	[10]
1.3	Kuo-Sheng	[11]
1.7	MUNU experiment, this work	[17]

magnetic moment of  $1.7 \cdot 10^{-10} \mu_B$  is obtained in this work at a 300 keV detection threshold.



**Figure 1.7:** Actual results for neutrino magnetic moments with reactor neutrinos. The blue dashed lines show the ratio of electromagnetic to weak cross section as a function of the recoil energy threshold. The excluded regions are dashed.

### *The MUNU experiment*

The MUNU detector is installed at 18 m distance from the core of the nuclear power reactor number 4 in Bugey (EDF, France). The Pressurised Water Reactor has a 2750 MW thermal power and is built in a solid basement, see figure 2.1. The laboratory R070 is shielded against neutrons and  $\gamma$ -rays from the core by the basement with an attenuation of 20 m water equivalent.

A nuclear power reactor is an intense source of antineutrinos. Per fission, on the average 6.71 antineutrinos are emitted, and a total energy of 205 MeV is released. For a reactor power of 2750 MWth, the number of emitted antineutrinos per second into a solid angle of  $4\pi$  sr corresponds to

$$\langle N_\nu \rangle = 6.71 \times N_{fiss} \simeq \frac{6.71 \times 2.75 \times 10^9 \text{ J/s}}{205 \text{ MeV} \times 1.602 \times 10^{-13} \text{ J/MeV}} \simeq 5.6 \times 10^{20} / \text{s} \quad . \quad (2.1)$$

The distance between the core and the detector is 18 m, reducing the antineutrino flux to  $10^{13} \text{ cm}^{-2} \cdot \text{s}^{-1}$ .

#### *2.1 The MUNU detector*

The MUNU detector is composed from inside to outside, as shown in figure 2.2, of the following parts: a gaseous time projection chamber for the electron tracking; an active shielding based on a mineral oil liquid scintillator and 48 photomultipliers to veto  $\gamma$ -rays and cosmic muons; a lead and borated polyethylene passive shielding against external  $\gamma$ -rays and neutrons.

A photography of the detector, see figure 2.3, shows the time projection chamber and the surrounding anti-Compton steel vessel. Some photomultipliers are visible in the background.

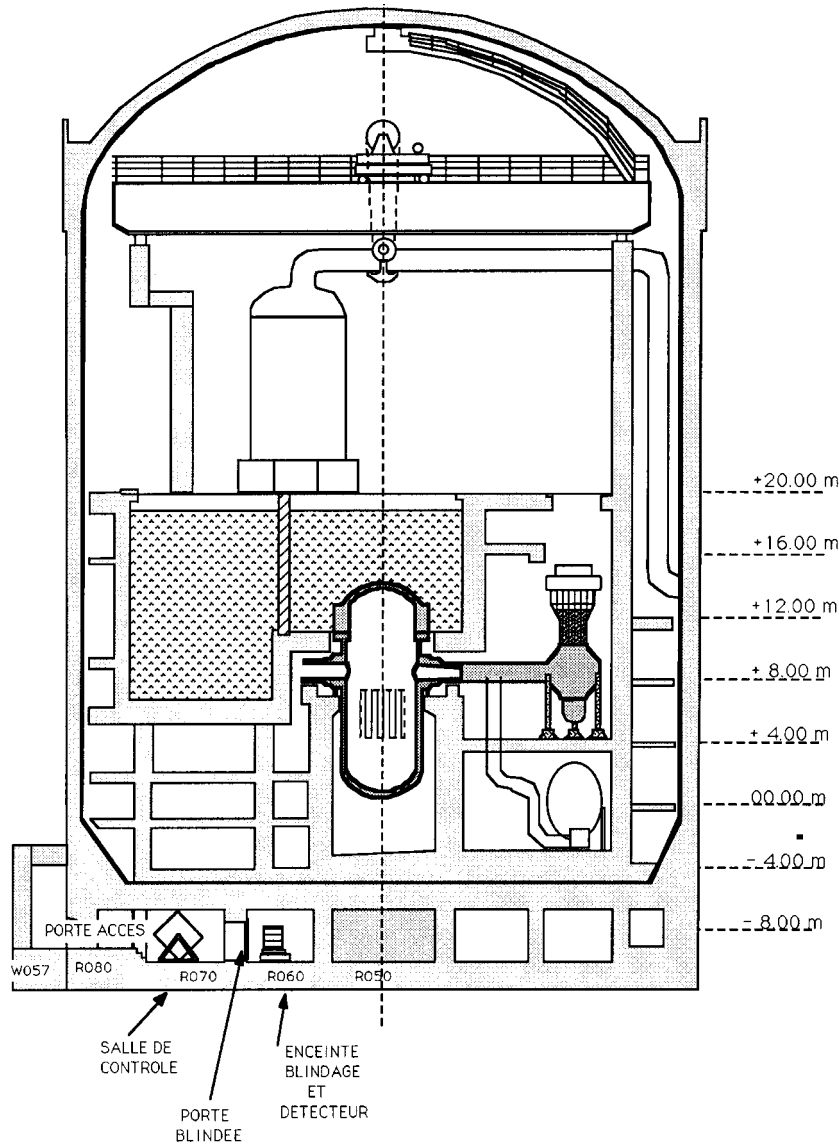


**Figure 2.1:** The building of reactor number 4 of Bugey. The MUNU experiment is located in the lab R070, at 18m distance from the reactor core.

In the following sections, the properties of the MUNU detector will be presented. Further details can be found in ref. [5],[18] and [19].

### 2.1.1 Time Projection Chamber

The  $1 \text{ m}^3$  vessel of the TPC is an acrylic cylinder, with 90 cm inner diameter and 162 cm length. The thickness of the radial wall is 0.5 cm, and the thickness of the end caps is 1.3 cm. The concentration of radioactive elements in

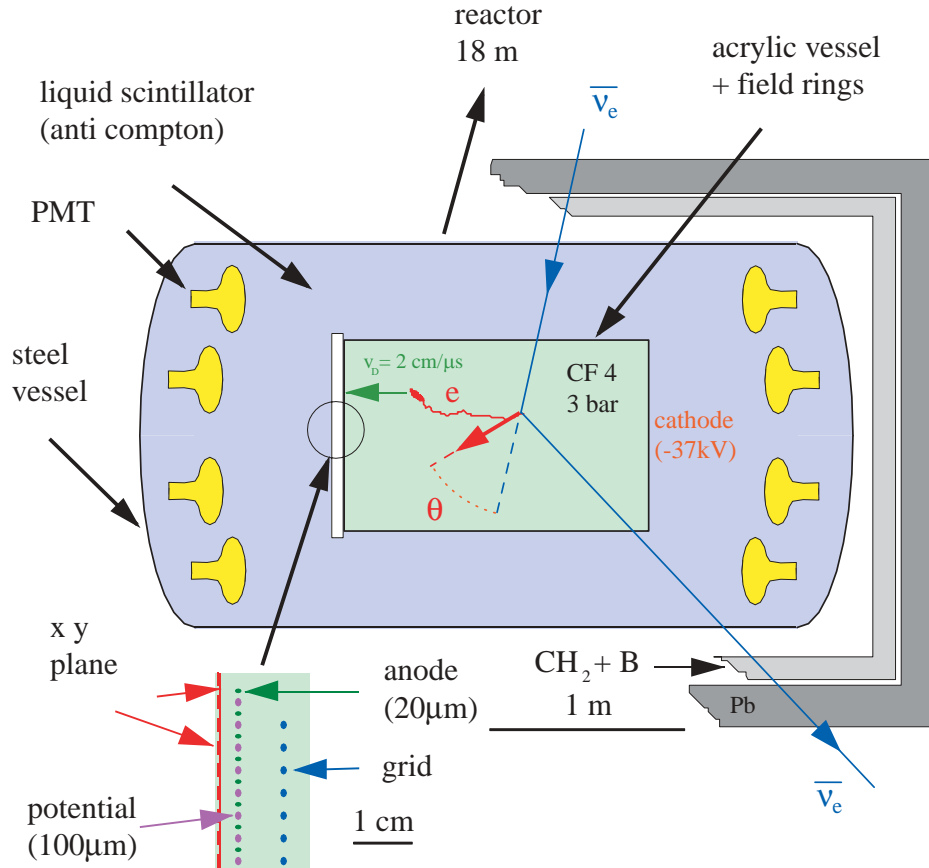


**Figure 2.2:** The MUNU detector.

acryl is low:  $2 \cdot 10^{-7} \text{g/g}$  for Potassium, and less then  $4 \cdot 10^{-12} \text{g/g}$  for Uranium and Thorium.

The high purity electrolytic copper foil cathode is mounted on one lid, see figure 2.2. The cathode is on a negative high potential of  $-37 \text{ kV}$ . The read-out plane on the other side, see figure 2.4, consists of the following parts, from inside to outside: a drift volume limiting grid, an anode plane and a  $xy$  induction plane. The grid wires have a diameter of  $100 \mu\text{m}$  with a  $4.6 \text{ mm}$  pitch and a  $45^\circ$  rotation against the vertical direction. The potential is  $-2 \text{ kV}$ , corresponding to an electrical field of  $220 \text{ V/cm}$  in the drift region. Field shaping rings made from copper strips are wrapped with  $1.5 \text{ cm}$  spacing around the acrylic vessel. The first ring is connected to the high voltage cathode and the last one to grid. The rings are arranged to define a homogeneous drift field inside the drift volume. Behind the grid in  $8.5 \text{ mm}$  distance, a multi-wire proportional chamber MWPC (see ref. [20] [21]) collects and amplifies the drift electrons. Anode and grid wires are mounted orthogo-

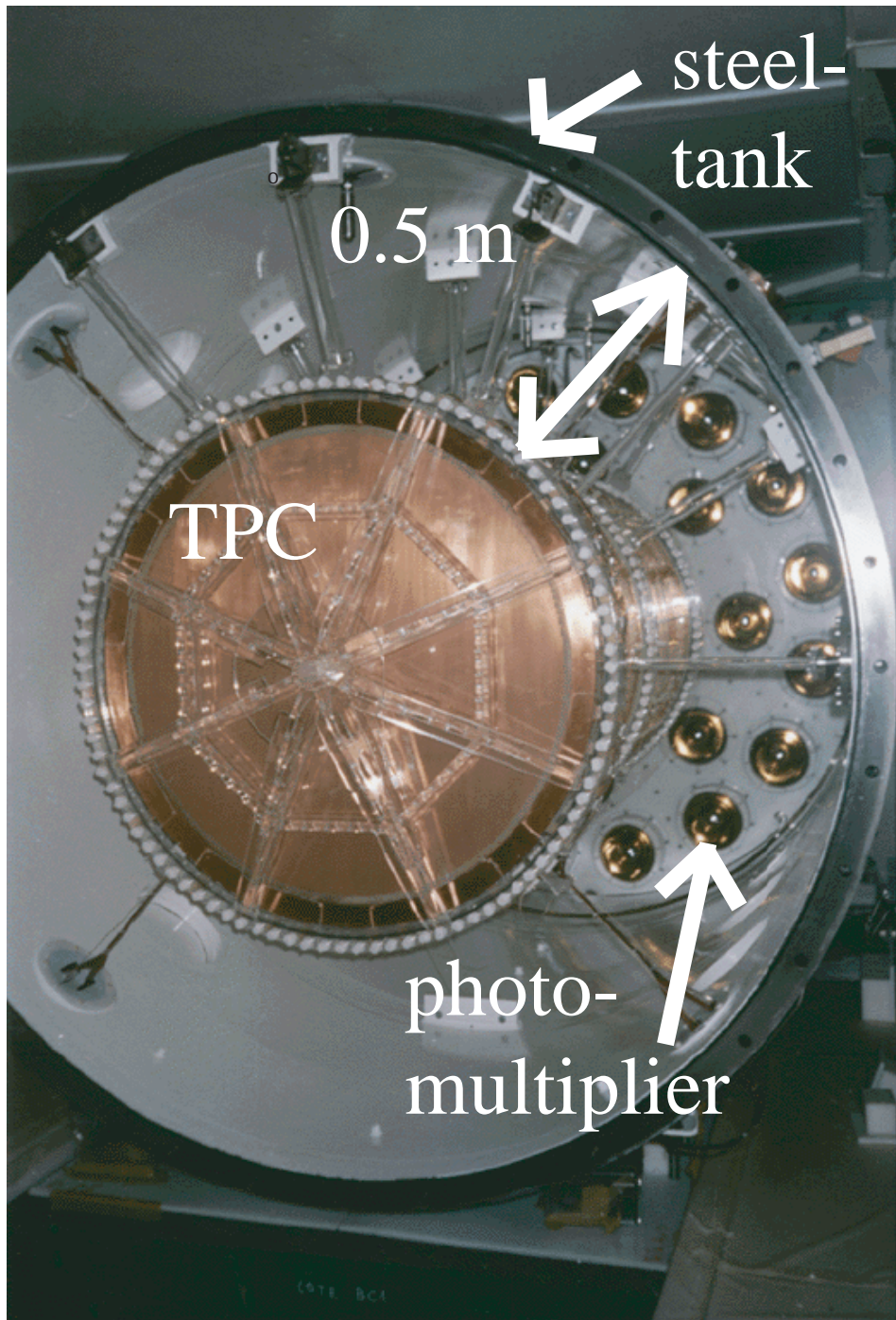


**Figure 2.3:** A photograph of the open MUNU detector. The time projection chamber is surrounded by the anti-Compton active shielding and the steel vessel. The photomultipliers are visible in the background.

nally. The anode wires have a diameter of  $20\ \mu\text{m}$  and a pitch of  $4.95\ \text{mm}$ . Potential wires with  $100\ \mu\text{m}$  diameter are placed between the anode wires. The anode potential is  $3540\ \text{V}$ . The potential wires are on  $400\ \text{V}$  potential and provide an electrical separation of the anode.

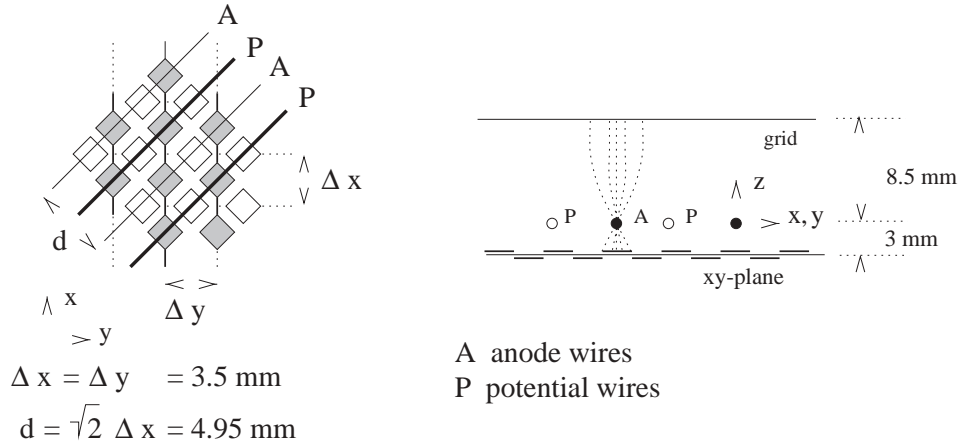


**Figure 2.4:** Schematics of the MUNU detection plane, with grid, anode and  $xy$ -plane.

The induction system, as illustrated in figure 2.4, is mounted  $3\ \text{mm}$  behind the anode and potential wires to sense the position of the induced signal. It consists of a  $125\ \mu\text{m}$  thick PET foil with  $90\ \text{cm}$  diameter, covered by two  $35\ \mu\text{m}$  copper films. On both sides,  $256$  isolated perpendicular strips are etched in the copper film with  $3.5\ \text{mm}$  pitches. The strips near to the drift field side are vertically orientated and provide the  $y$  information. The strips on the opposite side are horizontally orientated and provide the  $x$  information. The third coordinate ( $z$ ), along the drift field, is obtained from the time evolution of the signals. Therefore, we are measuring the  $xz$  and  $yz$  projections of the track. With the TPC, we can visualize and reconstruct the track in three dimensions. From the first few cm of the track, the scattering angle  $\theta$  can be obtained.

#### 2.1.1.1 Drift gas $\text{CF}_4$

The electrons of the  $\text{CF}_4$  gas, which is filled in the  $1\ \text{m}^3$  acrylic vessel at a pressure of  $3\ \text{bar}$ , are the targets for the  $\bar{\nu}_e e^-$  elastic scattering. The pressure of  $3\ \text{bar}$  is a compromise: on one side, the electron density increases with the pressure. On the other side, the multiple scattering increases as well. The  $\text{CF}_4$  is a well known drift gas (see ref. [22]), which was chosen for the following reasons:

- High electron density, and hence more electron targets for the  $\bar{\nu}_e e^-$  scattering. The density at STP is  $1.06 \times 10^{21}$  electrons per  $\text{cm}^3$ .

- Low atomic number  $Z$ , and therefore reduced multiple scattering for the electrons. Less multiple scattering improves the track reconstruction and the angular resolution.
- The gas is almost transparent to low energetic  $\gamma$ -rays, increasing the detection efficiency for the anti-Compton.
- Good drift properties.
- No free hydrogen, and consequently no inverse  $\beta$ -decay reaction  $\bar{\nu}_e + p \rightarrow e^+ + n$ . The cross section of this background reaction is  $10^{-43} \text{ cm}^2$ .

Moreover, the gas is not toxic, inflammable and cheap. Gas purity is important, since oxygen traps the drift electrons. Radon and other radioactive isotopes are an important contribution to background, and have to be removed. Purity is realised by circulating the gas at a flux of 500 liter per hour through a filter from SAES [23]. Behind the filter, a cold trap operating at  $-95^\circ\text{C}$  removes all radon contaminations by liquefaction. Unfortunately, liquefaction of  $^{85}\text{Kr}$  ( $-152^\circ\text{C}$ ) is below the liquefaction of  $\text{CF}_4$  ( $-129^\circ\text{C}$ ), and thus  $^{85}\text{Kr}$  cannot be removed with the cold trap, see ref. [24].

### 2.1.1.2 Drift region

Charged particles are depositing their energy by ionising the gas. In  $\text{CF}_4$ , the mean energy of creating an electron-ion pair is 34.3 eV, which was measured with  $\alpha$ -particles of 5.1 MeV, see ref. [25]. The secondary electrons move towards the anode due to the electric field (220 V/cm) in the TPC. The drift speed of the electrons is limited by collisions with the gas molecules. Typically, the drift time for 162 cm is 70-80  $\mu\text{s}$ . Longitudinal and transversal diffusion during the drift corresponds to a few millimetres. The distance between the anode and potential wires, and similarly the width of the  $xy$  pickup strips is optimised to the diffusion. The mean attenuation length of drifting electrons at 3 bar was measured to be  $22_{-6}^{+14} \text{ m}$ , see ref. [18].

### 2.1.1.3 Signal amplification

The grid is the start of the so-called avalanche region of the wire chamber. In this region, the charge is collected and amplified in the high electric field of the anode wires. Two effects have to be taken into account to describe the avalanche. The first effect is the attachment, which corresponds to a capture of drift electrons in the avalanche region due to  $\text{CF}_4$ . At 3 bar and  $25^\circ\text{C}$ , only 2.7% of the drift electrons survive the attachment. The second effect is the multiplication of electrons. An accelerated electron in the electric field ionises the  $\text{CF}_4$  and creates new electron-ion pairs. The multiplication at 3 bar and  $25^\circ\text{C}$  is  $1.5 \cdot 10^4$ . The electrons are accelerated towards the anode wires, whereas the positive ions are accelerated towards the potential

wires. The integral of the collected charge is proportional to the number of secondary electrons and consequently to the kinetic energy of the recoil electron having ionised the gas.

The ions  $\text{CF}_4^+$  and  $\text{CF}_3^+$  are created in the electron avalanche. Recombination or deexcitation of these ions is followed by emission of the so-called scintillation light, see ref. [26], with wavelengths between 200 and 500 nm. The photons with wavelength above 400 nm can be detected by the photomultipliers consequently. The scintillation light of the avalanche is an alternative measurement of the kinetic energy of the electron.

More details can be found in ref. [27]-[30].

### 2.1.2 Active shielding: Anti-Compton

The TPC is surrounded by a cylindrical steel vessel, filled with a liquid scintillator to veto  $\gamma$ -rays which scatter in the gas and generate low energy recoil electrons. The scintillation light is detected by 48 photomultipliers, 24 on each lid. The length of the cylindrical steel vessel is 3.80 m and its diameter is 1.90 m. The steel is painted with reflective  $\text{TiO}_2$  to optimize the scintillation light collection. The radioactive contamination of the steel vessel is low: the concentration is  $3 \cdot 10^{-11}$  g/g for Uranium,  $1.8 \cdot 10^{-9}$  g/g for Thorium and  $14 \cdot 10^{-7}$  g/g for Potassium.

The space between the steel vessel and the TPC is filled with  $9 \text{ m}^3$  of the mineral oil based scintillator NE235. The emission spectrum is between 400 and 500 nm, with an attenuation length of 8 m at 430 nm. The concentration of radioactive elements is low:  $3 \cdot 10^{-9}$  g/g of Potassium and less than  $3 \cdot 10^{-12}$  g/g of Uranium and Thorium.

The 48 low activity photomultipliers (type EMI 9354KB from the enterprise *Thorn EMI Electron Tubes* [31]) are mounted on a vertical polyethylene plane in a distance of 1.4 m from the centre. The hemispherical geometry and 20 cm diameter allows covering a surface of  $540 \text{ cm}^2$ . The quantum efficiency is 25% between 300 and 500 nm. The high amplification of  $10^7$  permits to register at a single photoelectron level. The activity was measured at the Laboratoire Souterrain de Modane to be very low: the concentration of Potassium is  $85 \cdot 10^{-6}$  g/g and the concentration of Uranium and Thorium is  $40 \cdot 10^{-9}$  g/g.

The background rejection of the anti-Compton is high, since the liquid scintillator is surrounding the TPC with 50 cm thickness in the radial direction, and with 60 cm at the end caps. The probability, that a  $\gamma$ -ray of 1 MeV from outside the steel vessel is simulating a Neutrino signal is  $10^{-6}$ . For  $\gamma$ -rays emitted inside the steel vessel, e.g. from the TPC walls or the gas, the rejection is only  $10^{-4}$ . From background of internal origin we expect not more than 2 events per day. Moreover, the active shielding provides veto against cosmic muons. Muons have a high-energy deposition in the scintillator of

a few hundreds of MeV, and are thus easy to reject. Muons can activate the scintillator by neutron capture, with a subsequent  $\gamma$ -decay with a mean lifetime of  $180 \mu\text{s}$ . Therefore, the muon veto has to be applied during  $200 \mu\text{s}$ .

### 2.1.3 Passive shielding: Lead and borated polyethylene

The passive shielding due to the liquid scintillator and steel vessel is not sufficient to protect against external  $\gamma$ -rays. Therefore, the detector is surrounded with 15 cm of low activity lead to reduce the local activities by a factor  $10^3$ . The passive shielding is shown in figure 2.5.

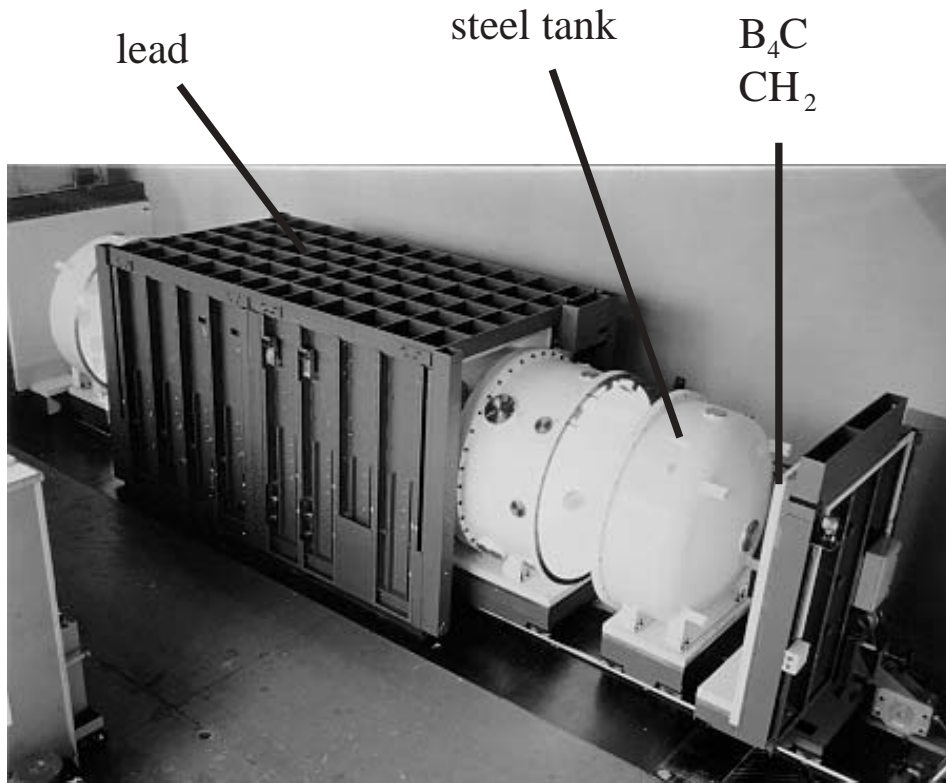


**Figure 2.5:** The passive shielding of the MUNU detector consisting of lead and borated polyethylene surrounds the steel tank.

Concerning cosmic muons, the Bugey laboratory is protected by a large overburden of steel, concrete and water, corresponding to about 20 m water equivalent. This attenuates the muons by a factor 4. The measured muon flux in the laboratory is  $32 \text{ m}^{-2} \text{ s}^{-1}$ . Muons can interact in lead and pro-

duce about  $5 \cdot 10^6$  neutrons per day. Thermal neutrons can interact with hydrogen ( $\sigma(H) = 330$  mb), present in the scintillator and the steel vessel. The subsequent emission of a  $\gamma$ -ray (2.2 MeV) would be an important contribution to background. Neutrons are attenuated in 8 cm polyethylene CH<sub>2</sub> plates after the lead shielding. The polyethylene plates are covered on both sides with B<sub>4</sub>C sheets to absorb the neutrons. Boron has a high cross section ( $\sigma(B) = 767$  b) for thermal neutrons.

#### 2.1.4 Background and radiochemical purity

The expected background per day is 2 events from external  $\gamma$ -rays and 2 events induced by cosmic muons. The background reaction  $\bar{\nu}_e + p \rightarrow e^+ + n$  in the acryl, gas and scintillator is negligible. The background with internal origin is related to the concentration of Uranium, Thorium and Potassium in the detector material. All detector parts have been selected to be radiochemically clean, as shown in table 2.1. From this we expect 2 background events per day. The total background simulating neutrino events for a 500 keV threshold is 6 per day. In the chapter 3 we will see, that the mea-

**Table 2.1:** Uranium, Thorium and Potassium concentration in the detector parts.

material	U [g/g]	Th [g/g]	K [g/g]
liquid scintillator	$< 3 \cdot 10^{-12}$	$< 3 \cdot 10^{-12}$	$0.3 \cdot 10^{-8}$
photomultiplier	$< 0.41 \cdot 10^{-7}$	$< 0.49 \cdot 10^{-7}$	$0.85 \cdot 10^{-4}$
steel vessel	$< 0.3 \cdot 10^{-10}$	$< 0.18 \cdot 10^{-8}$	$0.14 \cdot 10^{-5}$
acrylic vessel	$< 3 \cdot 10^{-12}$	$< 4 \cdot 10^{-12}$	$2 \cdot 10^{-7}$

sured background is much higher than the expected 6 events per day: The measured rate of electrons ( $T > 300$  keV) with a  $\gamma$ -ray of more than 90 keV is 0.15 Hz, and is probably due to Krypton and Cobalt. This type of events is rejected by the offline filter. The remaining 15 mHz electrons without a  $\gamma$ -ray in the scintillator cannot be rejected. This background is probably due to a Krypton and Radon contamination in the gas.

## 2.2 The trigger of the MUNU experiment

The main hardware trigger for a neutrino run is the anode signal. This signal is vetoed against Compton events and cosmic muons. Electrical discharges are rejected by the online filter due to the asymmetry in the light yield between the anode and cathode side. The active shielding and online filter reduce the 90 Hz anode counting rate to 0.23 Hz, which can be read out by the data acquisition with a 40% dead time. The data is then written to disc with 0.14 Hz, and afterward transferred to tape. In the following section, the hardware trigger and online filter are presented in detail.

### 2.2.1 Neutrino hardware trigger

The anode signal is used as the main trigger for the data acquisition. The trigger threshold is at 250 keV with a  $1 \mu\text{s}$  integration time. Muons are the main contribution to the 90 Hz counting rate, because the detector is not underground. A cosmic muon crossing the detector has a path length of more than 100 cm in the scintillator. With a mean energy loss of about 1.8 MeV per cm, the muons deposit a large signal in the scintillator, which is seen by the photomultipliers. Hence, cosmic muons can be rejected easily by a 22 MeV energy threshold. The trigger schematic is shown in figure 2.6. The muon veto is applied on the anode signal during  $200 \mu\text{s}$  and reduces the anode counting rate to 0.86 Hz. The remaining events are electrons from Compton scattering and electrical discharges. Electrical discharges have a high charge deposit on the anode and on the  $xy$  readout plane, and will be rejected later by the online filter. The veto AC against low energy  $\gamma$ -rays is defined by an energy threshold of 100 keV corresponding to a total collection of 15 photoelectrons. Because the contribution from dark noise (300 Hz) from individual phototubes is not negligible, a multiplicity of at least 8 photomultipliers is required for the veto. The veto is applied during

#### TPC anode

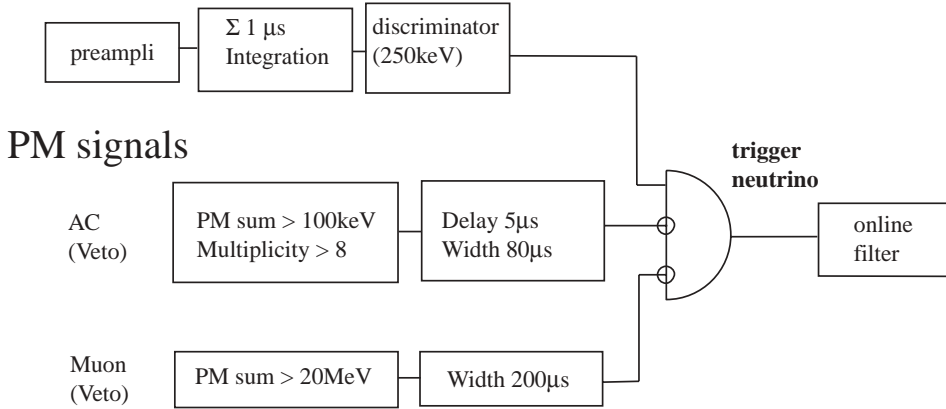


**Figure 2.6:** The neutrino trigger.

$80 \mu\text{s}$ , corresponding to the total drift time in the TPC. A delay of  $5 \mu\text{s}$  is necessary to not to reject electrons due to their own avalanche. The efficiency of the anti-Compton veto is  $10^{-4}$  for  $\gamma$ -rays from inside the TPC, and  $10^{-6}$  for  $\gamma$ -rays coming from outside the detector.

The anti-Compton counting rates are measured online: The muon veto rate is 260 Hz, and the AC veto against Compton electrons is 710 Hz respectively. All counting rates were stable during the data-taking period. Application of the anti-Compton and cosmic muon veto reduces the neutrino hardware trigger to 0.51 Hz. This trigger rate is still too high for our data acquisition

system, since the readout time of one event is 2.5 seconds. A more selective trigger was therefore needed to reduce the dead time. An online filter was developed to reduce the electrical discharges.

### 2.2.2 Online filter against electrical discharges

The online filter is directly built into the VME readout system, see section 2.3. The online filter is used to reject electrical discharges. Without the online filtering, the electrical discharges saturate the data acquisition: The neutrino hardware trigger collects 60% of, whereas the rest (40%) are discharges. To identify the electrical discharges, the asymmetry  $a$  of the collected light (PM) between the anode and the cathode side is calculated:

$$a = \frac{\sum \text{PM}_{\text{Anode}} - \sum \text{PM}_{\text{Cathode}}}{\sum \text{PM}_{\text{Anode}} + \sum \text{PM}_{\text{Cathode}}} . \quad (2.2)$$

The anode plane is located 80 cm from the TPC centre, and an avalanche is expected to have an asymmetry  $a$  near 0.6 for every event. However, due to saturation of the photomultipliers the asymmetry is smaller for muons (0.18), electrons (0.16) and  $\alpha$ -particles (0.06). Electrical discharges are emitting only a faint light, and consequently the photomultipliers are not saturating: the asymmetry of electrical discharges remains close to 0.6. The asymmetry can therefore be used to distinguish between electrical discharges and electrons. The asymmetry distribution without the online filter is shown in figure 2.7. A further characteristic of electrical discharges is their short

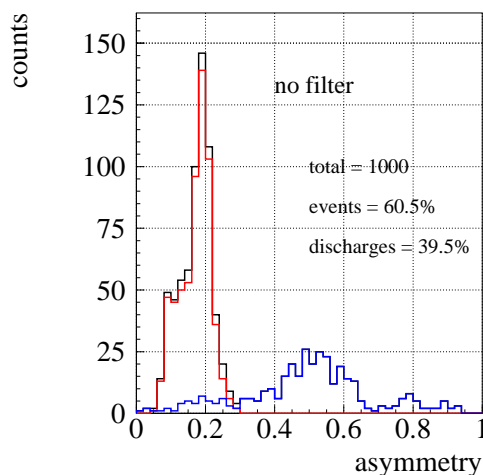


**Figure 2.7:** Asymmetry of the light collection by the PM. The normal events have asymmetries below 0.25, whereas discharges are characterised with asymmetries above 0.25. With a typical neutrino trigger without filtering, there are 60% events and 40% discharges.

signal length (less than 600 ns) in the photomultipliers, thus allowing an even better rejection. Based on the asymmetry and signal length, a fast online trigger is developed. The online trigger reveals the electrons by reducing the

discharges efficiently. After the online filter, there are only 14% of discharges left, which can be identified and rejected later by a more detailed analysis. The acceptance and efficiency of the online filter is determined with a spe-

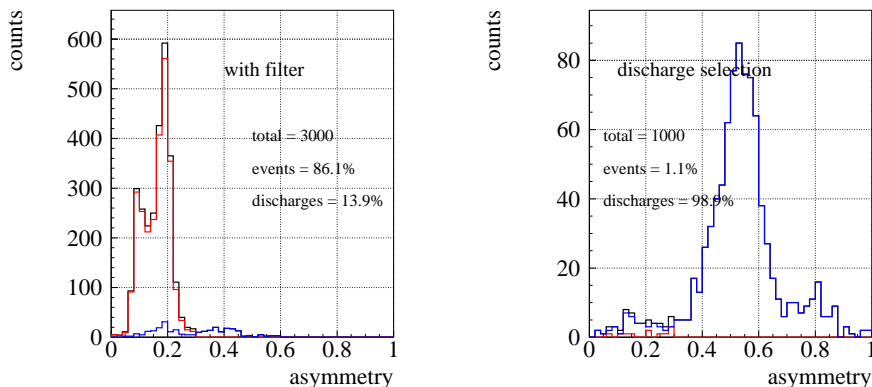


**Figure 2.8:** Asymmetry distribution, taken with the filter against discharges. The right plot shows the asymmetry distribution, taken with the negative discharge filter.

cial run, by applying a negative discharge filter on the hardware trigger. This filter is triggering only on discharges, but accidentally also on 1.1% electrons. These electrons would have been rejected by the discharge filter, hence reducing the acceptance. The table 2.2 summarizes the percentage of electrons and discharges for the three different run types. The efficiency  $\epsilon$

**Table 2.2:** Online filter against discharges.

Event type	No filter	filter	anti filter
Discharge	40%	14%	98.9%
Electrons	60%	86%	1.1%

gives the percentage of rejected discharges, and the acceptance  $\alpha$  is defined as the percentage of electrons left after the online filtering. With the online filter we have

- $\alpha \cdot 60$  accepted electrons,
- $(\epsilon - 1) \cdot 40$  accepted discharges.

The ratio of accepted electrons to accepted discharges after the filter is then given by

$$\frac{\alpha \cdot 60}{(1 - \epsilon) \cdot 40} = \frac{86}{14} . \quad (2.3)$$

This equation contains two unknowns  $\alpha$  and  $\epsilon$ . Therefore, we need another equation to obtain the acceptance and the efficiency. For that purpose, we are applying the anti filter and have now:

- $(\alpha - 1) \cdot 60$  accepted electrons,
- $\epsilon \cdot 40$  accepted discharges.

The ratio of accepted electrons to accepted discharges after the anti filter is now given by

$$\frac{(1 - \alpha) \cdot 60}{\epsilon \cdot 40} = \frac{1}{99} \quad . \quad (2.4)$$

The acceptance and the efficiency can be solved by calculating  $\alpha$  from the first equation 2.3 and replacing it in the second equation 2.4. The efficiency is then given by

$$\epsilon = \frac{60/40 - 86/14}{1/99 - 86/14} \simeq 75.7\% \quad ,$$

and the acceptance is

$$\alpha = \frac{86}{14} \frac{40}{60} (1 - \epsilon) \simeq 99.5\% \quad .$$

The high efficiency of the online filter is very important, because the dead time without filter is around 70%. A dead time in this order means that data taking during 100 days corresponds to only 30 days effective measuring time. With the new filter the dead time decreased to 40%, hence increasing the live time of our experiment by almost a factor two. The counting rate of the accepted events after the online filter is 0.23 Hz, and the data acquisition has written the events with 0.14 Hz to disc.

### 2.2.3 Summary

The main trigger for a  $\bar{\nu}_e e^-$  scattering is the anode signal, with a threshold at 250 keV. The anti-Compton active shielding is providing a veto against cosmic muons and Compton electrons. Electrical discharges are reduced by the asymmetry between the anode and cathode side. The measured counting rates are summarized in the table 2.3. In appendix A.1 and app:neutrinohard, the counting rates are shown as a function of time. The stability of the counting rate is important for the interpretation of the electron counting rate.

## 2.3 The data acquisition

The readout system, see figure 2.9, consists of the following parts: a VME crate for the main control, 3 crates housing the 72 flash ADC modules, a

**Table 2.3:** *The hardware trigger.*

Anti-Compton (100 keV, M8, 80 $\mu$ s veto)	710 Hz
Anti-Compton Muon Veto (22 MeV, 200 $\mu$ s veto)	260 Hz
TPC trigger (250 keV)	90 Hz
+ TPC veto muon veto	0.86 Hz
+ Anti-Compton veto	0.51 Hz
+ Online trigger (discharge filter, $\alpha = 99.5\%$ )	0.238 Hz
Recorded events	0.144 Hz

CAMAC crate with the trigger selection and dead time system, and a NIM crate for the hardware trigger. The FADC crates and CAMAC crate are connected to the VME crate with interface modules, while the NIM crate is a standalone system. The VME crate is connected by Ethernet to a server. The server is used to start and stop the data acquisition and for the data storage. More detail can be found in 2.3.5.

### 2.3.1 VME crate and main control

The VME crate houses the VME master module (FIC8234, a CPU running under OS9), interfaces to the FADC crates, an interface to the CAMAC crate, a CORBO trigger module and a slow control (pressure and temperature) unit. The data acquisition program, based on CASCADE [32], is running on the master module. Readout is started when a START signal arrives on the input of the CORBO [33] module. The program reads out the detector signals from the FADC crates, performs the event building and writes the data to discs on the server machines. The program is used for the online filter, the readout of the slow control data and the dead time measurement as well. Furthermore, the trigger program for the ULM module, see below, is transferred to the Xilinx chip via the CAMAC interface.

### 2.3.2 Flash-ADC crates to digitize signals at high speed

The anode, strip and photomultiplier signals are sampled by a 12.5 MHz - flash ADC system from STRUCK [34]. Every FADC crate is equipped with 24 flash ADC modules, a sampler module (SAM DL352) and an interface module (SIM DL357). The flash ADC modules are operating in circular mode: the analogue signals are sampled and recorded continuously in a 1024 word memory. Each word (z-bin) corresponds to a depth of 8 bits. The analogue signal is therefore recorded with integer values between 0 and 256. The flash ADC modules are operating in non-linear mode, which provides a uniform resolution even for small pulses. Figure 2.10 shows a example of a photomultiplier pulse.



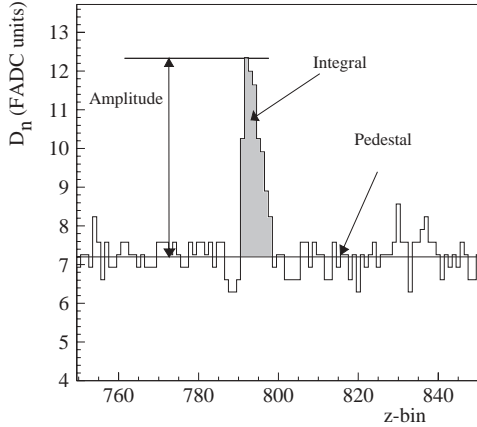


**Figure 2.10:** Digitalisation of a photomultiplier pulse. One  $z$ -bin corresponds to 80 ns. The non-linear pulse height  $D_n$  can be transformed with a simple expression to a voltage.

### 2.3.4 CAMAC crate for the trigger system and dead time measurement

The CAMAC crate houses a ULM2366 [35] trigger module and a scaler module for counting. The scaler counts the triggers from the anode, anti-Compton veto and the selected trigger from the ULM module. Moreover, the scaler is measuring the dead time of the data acquisition with a 120 Hz clock. The ULM module is equipped with a Xilinx chip [37] [38] which is programmed to select remotely the hardware trigger, e.g. from CERN. The delay time can be adjusted, and coincidences or vetos between the signals are feasible. The delay time for the neutrino trigger is set to  $40 \mu\text{s}$ , because the position of the track is then in the centre of the recorded time window. Detail can be found in diploma thesis [29].

### 2.3.5 Run control

The main parts of the run control consist of a scheduler, a watchdog and a backup system. The run control is reducing the dead time of the experiment. Moreover, the system allows working remotely, e.g. from CERN.

The total capacity of the discs is about 10 GB, enough for storing data of one day of data acquisition. A typical neutrino run corresponds to 3000 events, and uses 1.8 GB of disc space.

During the start process of a run, a free disc is selected by the scheduler. After the stop of a run, a logfile is completed with the required information, e.g. the start and stop time, the number of recorded events, the disc space used and the runtype and trigger. The scheduler starts afterwards a new run, according to a runlist. In this list, the exact runtypes and number of

required events are specified. The scheduler is controlled by a watchdog. This is important, because the data-acquisition is interrupted frequently by hardware failures. The scheduler itself is not disturbed by the hardware failures, and is able to handle the interrupts. All this reduced the dead time significantly.

After a run is finished and transferred to the acquisition servers, the data is written to tape. To prevent full discs, a successful backup system was developed. On a DLT tape, with 40 GB compression, is space for 6 to 7 days of data taking, corresponding to 20-30 neutrino runs typically.

## 2.4 Typical events in the MUNU experiment

Typical events of the MUNU experiment are shown in figures 2.11-2.15. The signals are recorded with the  $x$  and  $y$  strips, and the  $z$  information is obtained from the time evolution. The event is therefore seen in the two projections  $xz$  and  $yz$ . A  $xy$  view of the signal can be obtained by combining the two projections  $xz$  and  $yz$ . The amplitude of the signal is represented by the color: higher amplitudes are dark (red and black), whereas low amplitudes are yellow.

Electrons (figure 2.11) are recognised by the curved track, which is due to multiple scattering in the gas. At the start of the track (the vertex), the energy deposition is low. The end of the track is characterised by an increased energy loss, leading to the typical end blob.  $\alpha$ -particles (figure 2.12, right) of a few MeV have short tracks of only a few cm due to the high energy loss. Muons (figures 2.13, 2.14) of a few GeV produce straight tracks, and are thus easy to distinguish from electrons. Electrical discharges on the anode plane (figure 2.15) are visible in one of the two projections, while the other projection is often empty.

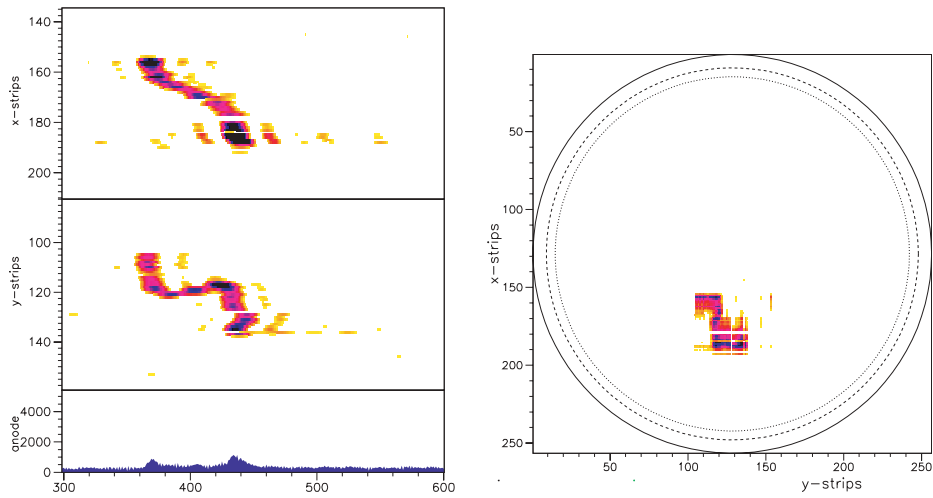


**Figure 2.11:** Electron track in the TPC. Left: the two projections  $xz$  and  $yz$ . Right: Reconstruction of the event in the  $xy$ -plane.

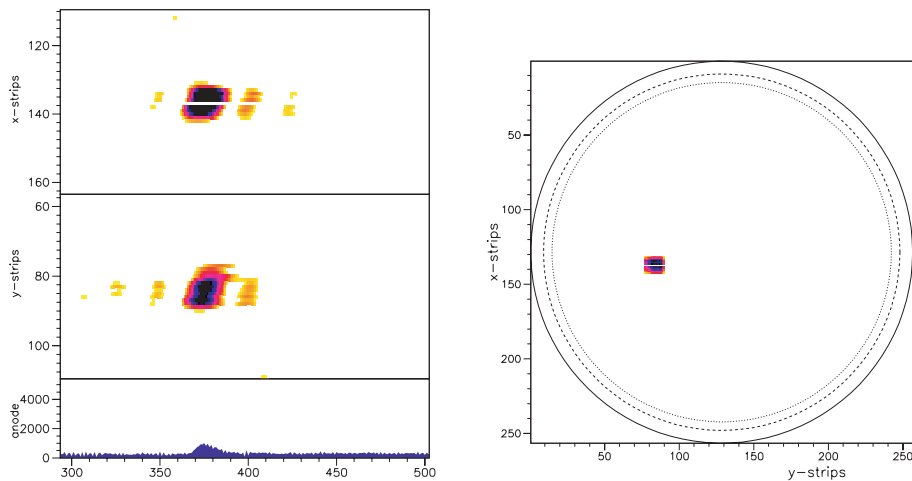


**Figure 2.12:**  $\alpha$ -particle in the TPC. Left: the two projections  $xz$  and  $yz$ . Right: Reconstruction of the event in the  $xy$ -plane.

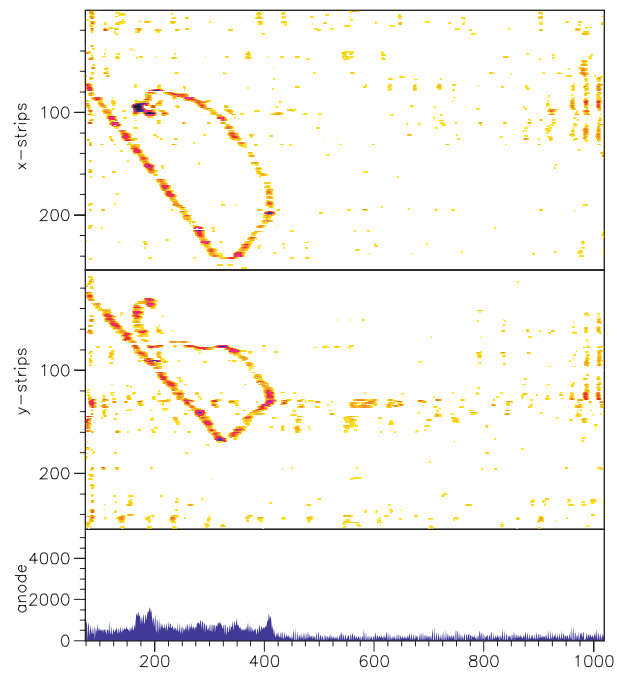


**Figure 2.13:** Muon with  $\delta$ -electron.

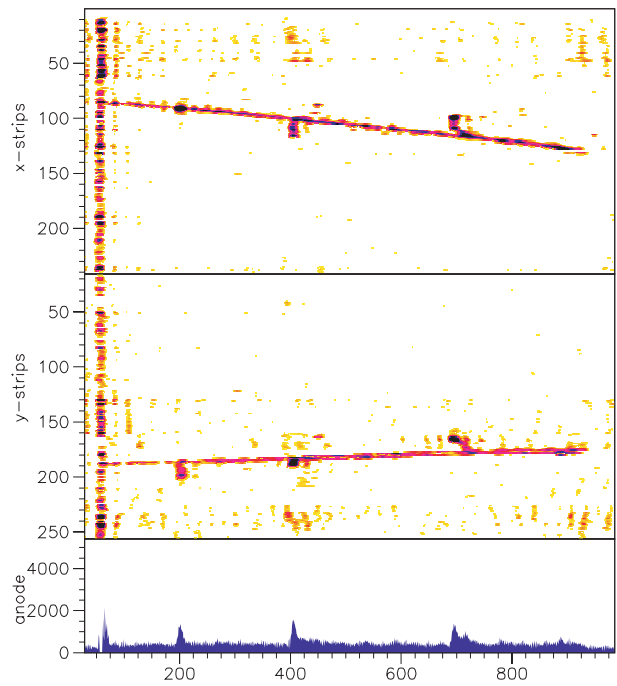


**Figure 2.14:** Horizontal muon, used for calibration.

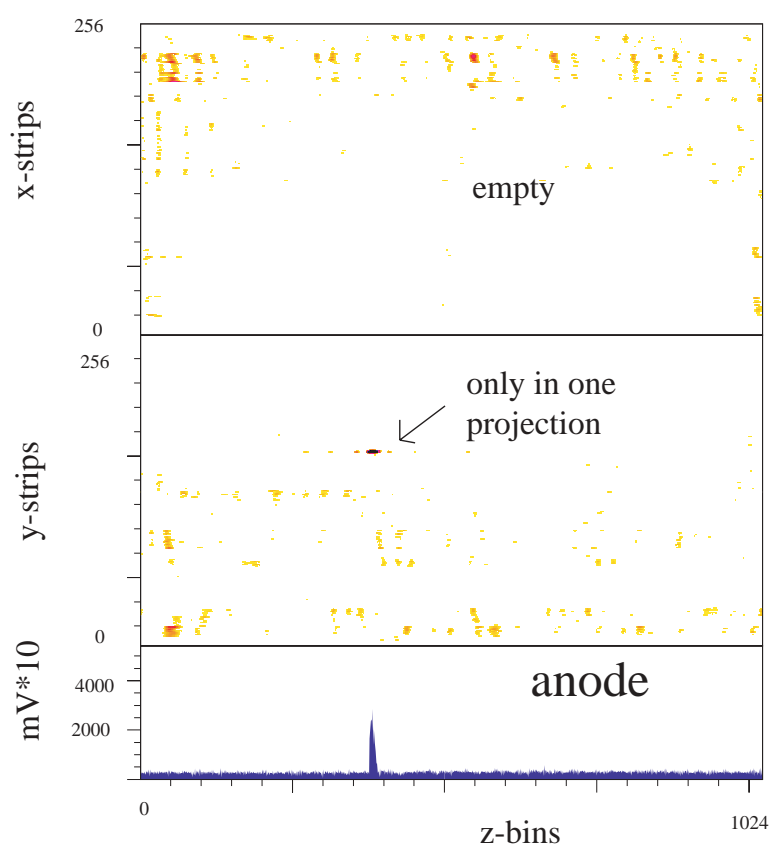


**Figure 2.15:** Electrical discharge on the anode with induced signal on the  $y$ -strips, which are nearer to the anode than the  $x$ -strips.

### *Offline filtering and calibration*

The raw data is processed in four steps, as shown in figure 3.1. First, the data is filtered against background events. This step reduces the number of events by a factor of five. In the second step, the vertex and scattering angle are reconstructed by the automatic tracking software for all remaining events. However, for the visual scanning only events above 700 keV are reconstructed. Additionally, the second step provides a reduction due to a classification of the event as electron inside the containment. In the third step, all runs of reactor ON are merged to one file, including information about the calibration, dead time, drift time and reactor power. The reactor OFF data is processed the same way. The merging utility is used for the automatic tracking and visual scanning. The last step compares the measured forward and backward counting rates with the Monte Carlo prediction, giving an upper limit on the neutrino magnetic moment, as discussed in chapter 6. In this chapter, the offline filtering will be described. All acceptances are used in the present analysis.

#### *3.1 Offline Filtering*

The offline filtering is performed with a program called FILL. This filter is used to reject obviously bad events, namely electrical discharges on the anode and read-out plane, Compton electrons, electrons outside the containment and electrons crossing the anode plane. Furthermore, a few events with saturation of the anode signal and some events with a wrong trigger time are rejected during this filtering stage.

The Monte Carlo simulation is far from being complete, and does not allow to study the global acceptance of the offline filter. Therefore, several independent studies are necessary to determine the acceptance of each filter separately. They are described in the following sections.

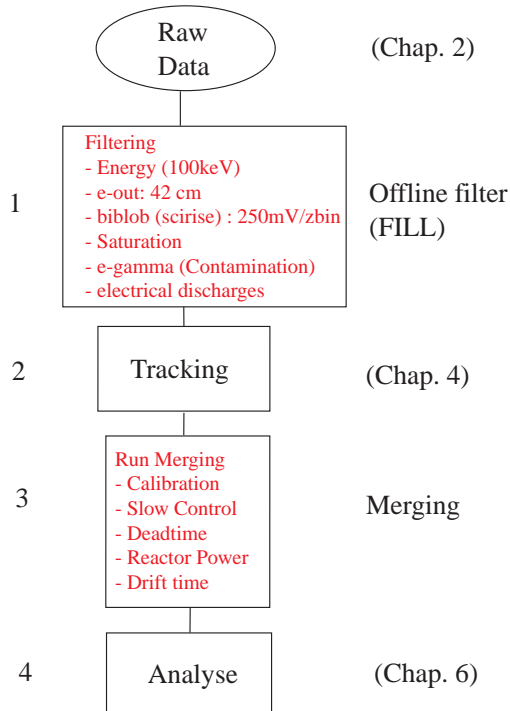


**Figure 3.1:** The four steps of data processing, see text.

Table 3.1 summarises the number of recorded and accepted events to give an overview for the coming discussion. In the table, the counts per day are given after successively applying the filter against electrical discharges, then against anode crossing, Compton electrons, and events where the track or a part of the track is outside the containment. For instance, we have 15200 events per day above 300 keV, and after removal of the electrical discharges, there are still 12300 events per day left. The anode-crossing filter reduces this amount of events to 5100 per day, and at the end of the offline filtering, there are 3100 events per day left. The reduction by the offline filtering is in the order of 20% with the 300 keV threshold, and decreases to 9% at 700 keV. The reason for the stronger rejection at low energy is the presence of higher background at low energy, consisting mainly of events crossing the anode and Compton events. It is important to remark, that some events are rejected by more than one filter. For instance, an electrical discharge on the anode plane is rejected by the anode-crossing filter as well. Electrons outside the containment can have a  $\gamma$ -ray, and they are therefore rejected by both the Compton filter and the containment filter. The disentanglement of the events is not simple, and therefore the table 3.1 gives the counting rates in a successive application of the filters. However, the selected order is important in the following meaning: after the removal of electrical discharges, there are only electrons left. The 12300 counts per day can be interpreted as 0.14 Hz of electrons in the TPC. After the application of the remaining filter, especially against Compton electrons and containment, the counting rate decreases to 36 mHz at 300 keV, and 5 mHz at 700 keV respectively. Compared to one

**Table 3.1:** Counting rates in counts per day (cpd) after the successive application of the offline filter at a 300 keV and 700 keV threshold.

<b>Successive filtering</b>	300 keV cpd	700 keV cpd
Recorded events	15200	4700
- Electrical discharges	12300	3850
- Anode-crossing	5100	950
- e- $\gamma$	4600	740
- e-out	3200	490
- other	3100	440

$\bar{\nu}_e e^-$  scattering expected per day, this counting rate is still too high and has to be reduced by the track reconstruction software later. The main advantage of the MUNU experiment is the combination of the active shielding and the track reconstruction.

### 3.1.1 Asymmetry filter against electrical discharges

Electrical discharges, as already discussed in section 2.2.2, are rejected by the asymmetry between the left and right photomultiplier light collection and the short signal length. After the online filter, there are still 14% of electrical discharges. Therefore, the offline filter recalculates the asymmetry with the software sum of each photomultiplier. In the online filter, the hardware sum of the photomultipliers is used instead. The more detailed analysis based on the software sum of the photomultipliers allows to reject most of the remaining electrical discharges. Figure 3.2 shows the signal length seen by the photomultipliers versus the asymmetry. The electrical discharges are identified and thus rejected without problem by this two dimensional topology. The acceptance of the online discharge filter is found to be close to 100% by eye scanning.

### 3.1.2 Filter against electrons crossing the anode plane

Electrons crossing the anode plane produce a high charge deposition similar to the end-blob of a normal electron track. Therefore, these electrons have two end-blobs, and it is not possible to disentangle the true end blob and the anode blob from the  $xz$  and  $yz$  projection alone. However, during the charge induction on the anode plane, the light emission is seen by the photomultipliers (PM) as well. Because the induction time is short (a few 10 ns only), the rise time in the PM is short and the pulse height change per  $z$ -bin (=derivative) of the PM sum is therefore high. Events with a derivative higher than 250 mV/ $z$ -bin are crossing the anode, see figure 3.3. A typical

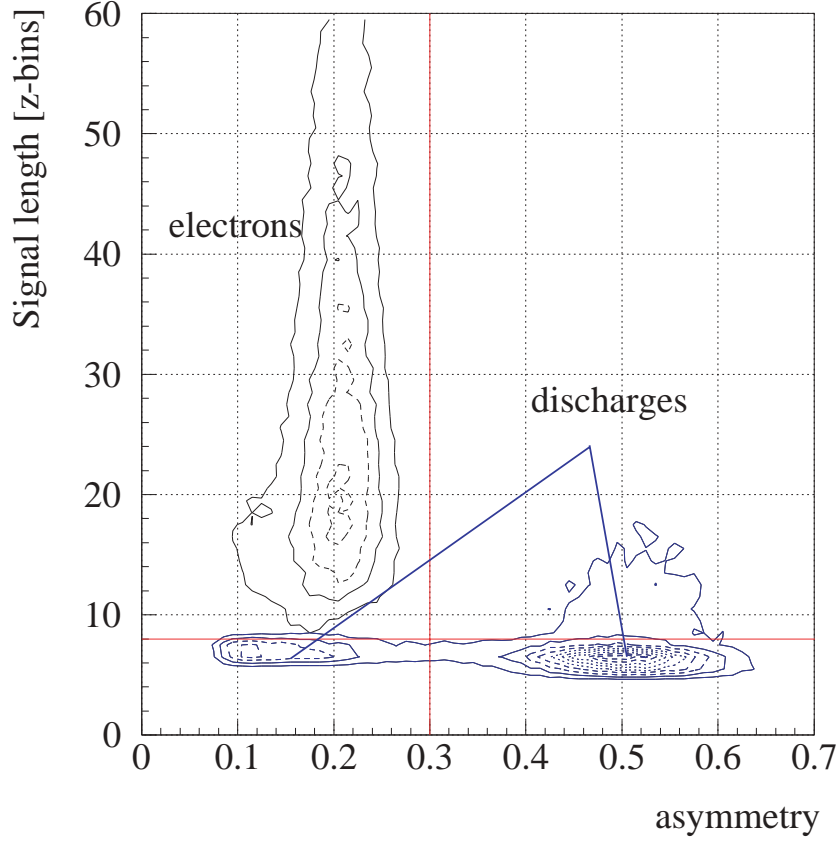


**Figure 3.2:** Signal length versus anode-cathode photomultiplier asymmetry. The offline cut is rejecting all events (blue colour) with an asymmetry larger than 0.3 or with a signal length smaller than 8 z-bins, corresponding to 640 ns.

biblob electron is shown in figure 3.4.

The biblob cut and acceptance are determined with a special run using a radioactive source (Mn). The biblob electrons are hence suppressed and almost not present in the data set. The file is scanned by eye afterwards, with vertex determination and direction fit. With this study, the acceptance of the biblob filter is determined to be 94%. A further possibility to study the acceptance of the biblob filter is to use runs taken with a muon veto trigger. Events taken with this trigger are mostly electrons with a  $\gamma$ -ray. If the  $\gamma$ -ray is preceding the avalanche of the electrons, then the event can be interpreted as a Compton scattering electron. If the electron would cross the anode plane from outside the TPC, the  $\gamma$ -ray would be hidden completely by the avalanche. Therefore, electrons with a  $\gamma$ -ray are not crossing the anode plane. Runs with the muon veto trigger are hence taken to study the filter against biblobs.

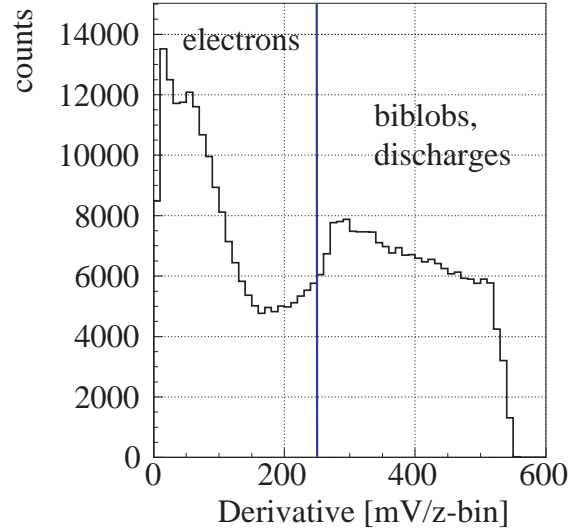


**Figure 3.3:** Derivative distribution for the reactor ON data 2001. The biblob events have a derivative above 250 mV/z-bin and are thus easily rejected.

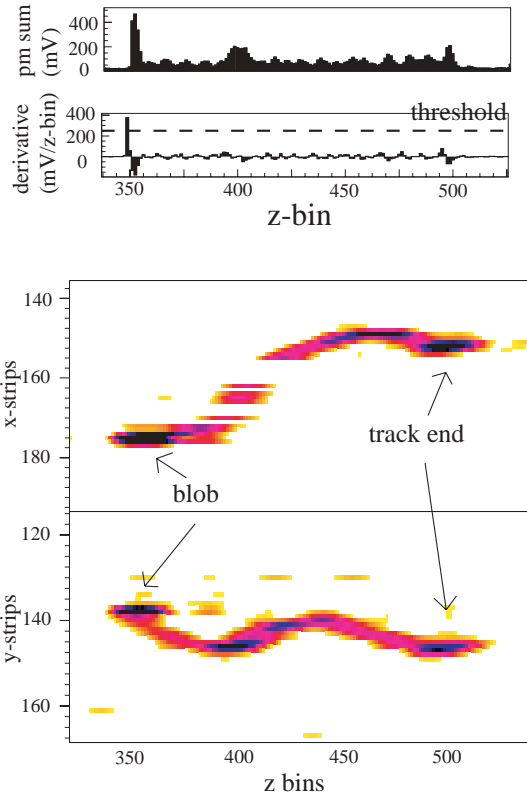


**Figure 3.4:** Electron crossing the anode plane with two end blobs. The derivative of the PM sum is shown in the top graph, and the two projections in  $xz$  and  $yz$  on the bottom.

Electrons from the anode plane probably come from  $\beta$ -decay of the isotope  $^{210}\text{Bi}$ , which is originating from  $^{210}\text{Pb}$ . The latter isotope is deposited on the grid and readout plane due to a Radon contamination of the  $\text{CF}_4$  gas.

### 3.1.3 Veto against electrons from Compton scattering

During the first  $5\ \mu\text{s}$  preceding the TPC trigger, no anti-Compton veto is applied. To reject the Compton electrons, the filter looks for a signal in the scintillator above 90 keV. The counting rate of this type of event is 770 per day and is stable in time, see appendix A.3. With a special muon veto trigger (delay  $75\ \mu\text{s}$ ), the total TPC can be monitored. The total drift time is roughly 15 times higher than the  $5\ \mu\text{s}$  of no anti-Compton veto. The expected 12000 electrons per day are in good agreement with the 13000 measured events. This counting rate corresponds to 0.15 Hz background, which can be attributed to 0.045 Hz  $^{40}\text{K}$ , 0.031 Hz  $^{60}\text{Co}$  and other contributions (0.074 Hz), as proposed in ref. [39]. The most probable location is the acrylic structure of the TPC and the scintillator. The angular distribution of Compton electrons is isotropic, and no 'hot spot' on the TPC wall can be identified. This excludes a contamination on the anode or cathode plane as well.

Figure 3.5 shows a typical electron  $\gamma$ -ray event. The time between the  $\gamma$ -ray (at z-bin 325) and the avalanche position (at z-bin 360) can be used to calculate the absolute position of the electron: 35 z-bins difference corresponds to  $2.8\ \mu\text{s}$ . For a typical drift time ( $80\ \mu\text{s}$ ), the absolute position is at 5.7 cm from the anode plane.

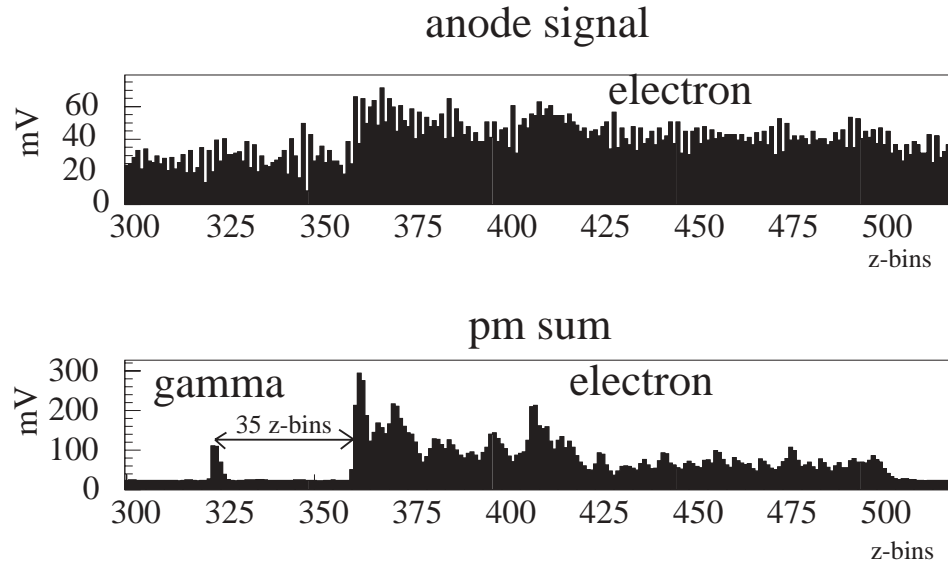


**Figure 3.5:** Electron and  $\gamma$ -ray, signals seen by the anode (top), and the photo-multiplier sum (bottom).

After electrical discharges, anode crossing events and Compton scattering electrons are removed, we have still 4600 electrons per day above 300 keV, and 740 above 700 keV respectively. However, the 99.4% acceptance of the  $e-\gamma$  filter is high. The remaining electrons can be further reduced by analysing

the radial position of the track. If the track of an electron is outside the 42 cm fiducial volume, it will be rejected in the next filter step.

### 3.1.4 Containment filter

The radial containment is calculated by combining the  $xz$  and  $yz$  projections to a  $xy$  view of the track, see figure 3.6. An algorithm is then able to recognise the electrons that are not fully contained in the 42 cm radius of the fiducial volume. This part can be simulated with the Monte Carlo program. For the determination of the acceptance, a  $\bar{\nu}_e e^-$  run is generated and filtered with the containment algorithm. The acceptance of the e-out filter is 86%. The remaining events after e-out filtering is decreasing to 3200 electrons per day at 300 keV, and the number of remaining events above 700 keV is 490 per day respectively. See appendix A.5 for the time evolution of the counting rates of electrons entering or leaving the TPC trough the wall.

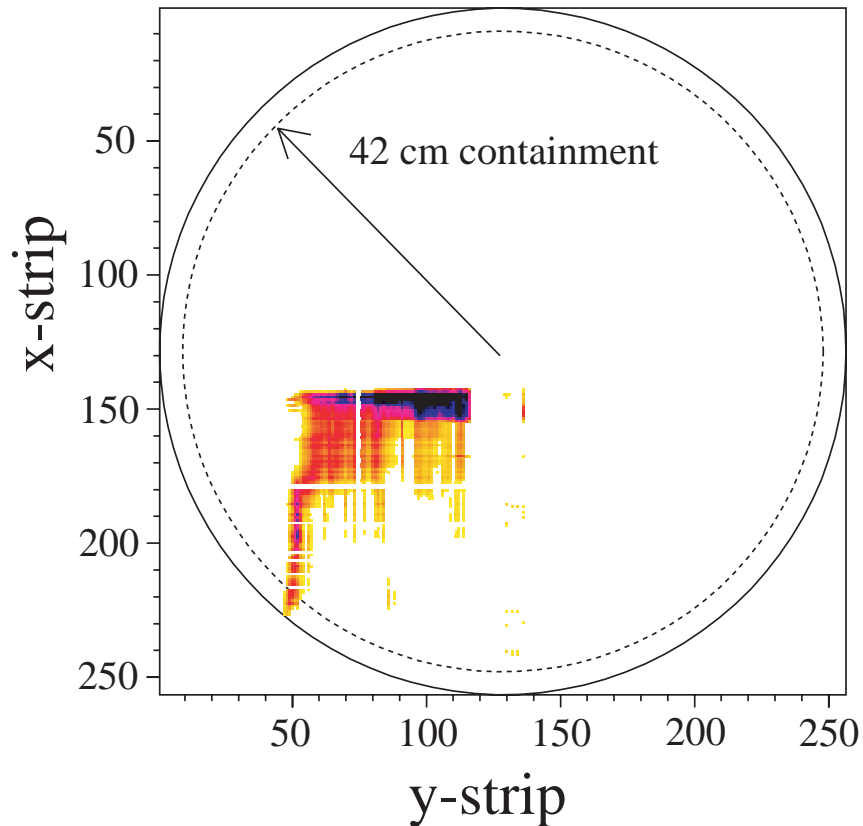


**Figure 3.6:** Electron entering the TPC trough the wall. The containment is defined by a 42 cm radius from the centre of the TPC. The radius of the TPC is 45 cm.

A further reduction of electrons with a track outside the containment is done

during the track reconstruction. The algorithm reconstructs the vertex and the electron will be rejected if its position is outside the 42 cm radius. This reduction (5%) is not very strong, however.

The longitudinal containment ( $z$ -axis) of the TPC is much more difficult to determine. If an electron is due to Compton scattering, then the time between the  $\gamma$ -ray in the scintillator and the avalanche time can be used to calculate the absolute  $z$ -position. Without the  $\gamma$ -ray, there is no way to determine the  $z$ -position. If an electron is entering the TPC by the cathode side, the track is not to distinguish from a track of a full-contained electron. However, if the electron is leaving or entering the TPC through the anode, it will be recognised by the biblob topology and rejected by its fast rise time of the scintillator light.

### 3.1.5 Accepted events

The counting rate of the accepted electrons within the containment is 3100 per day (36 mHz) above 300 keV, and 440 per day (5.1 mHz) above 700 keV respectively. However, this counting rate is not stable in time. The evolution is shown for both energy thresholds in figure 3.7. At 300 keV a continuous increase over the full data taking period is observable, with a sharp step of more than 2000 counts per day around day 700 when the gas was exchanged. At 700 keV and above, the continuous increase in the counting rate is still present. However, the gas exchange at day 700 has no effect. In ref. [39], the

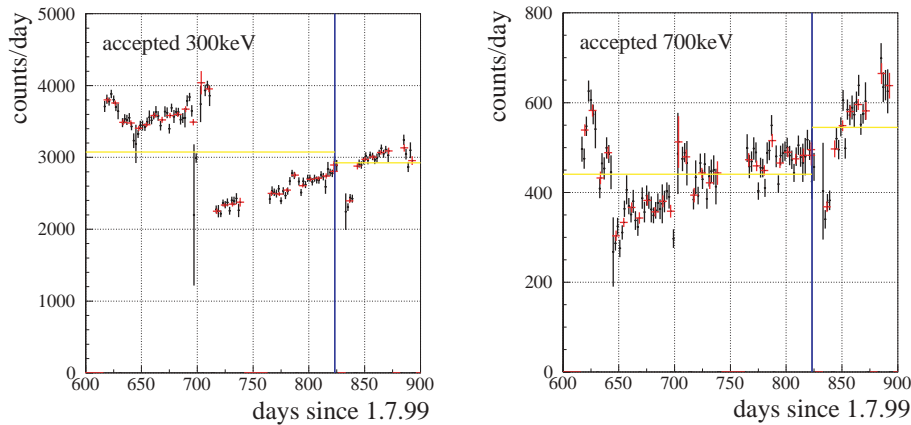


**Figure 3.7:** Counting rate of accepted electrons inside the fiducial volume. Runs taken before day 823 (vertical line) are with reactor ON, after which day the reactor is OFF.

preferred explanation is the presence of Krypton in the gas. Krypton  $^{85}\text{Kr}$  emits an electron with a  $Q_\beta$  of 687 keV. This explains why the counting rate above 700 keV is not affected after the gas exchange. Krypton mixes well with  $\text{CF}_4$ , and is present in the atmosphere with an activity of  $1\text{Bq}/\text{m}^3$ .

It is possible, that Krypton was entering our detector during an opening period. The cold trap, which operates at  $-80^{\circ}\text{C}$ , is not able to liquefy and remove the Krypton, which becomes liquid at  $-152^{\circ}\text{C}$ . This explains the accumulation of Krypton in the gas.

### 3.1.6 Summary and conclusion

The acceptances of the offline filter are given in table 3.1.6. The most important reduction (86%) is due to the radial containment, and is determined with a Monte Carlo simulation. The second strong reduction in the acceptance is due to the biblob cut against events crossing the anode. The filter against discharges and Compton electrons are hardly reducing the signal of  $\bar{\nu}_e e^-$  scattering. The total acceptance of the online and offline filter of 80% is taken into account in the analysis, see chapter 6.

**Table 3.2:** Online and offline filter acceptances

Filter	Acceptance
Discharge online	99.5%
Discharge offline	100%
Biblob	94%
Compton	99.4%
Containment	86%
<b>Total filter acceptance</b>	<b>80%</b>

We have taken data during 66.3 days with reactor ON and 19.3 days of background without reactor. During data taking, some counting rates have changed, which is explained by a Krypton contamination. The complete filtered data set is then processed by the automatic tracking reconstruction, which was developed for this thesis.

## 3.2 Detector calibration and slow-control

The calibration of the detector consists in the energy calibration and in the time to length conversion of the z-binning. Another important task is the slow-control of the pressure, temperature and the electron density in the TPC. The dead time measurement of the hardware trigger, online filter and readout gives us the effective live time of the experiment. In addition, for the prediction of the expected number of  $\bar{\nu}_e e^-$  scattering we need the reactor power. This is the topic of the present section.

### 3.2.1 Energy calibration

For the calibration we used a  $^{54}\text{Mn}$  source, which was placed close to the TPC wall, with a 26.4 cm distance from the anode plane. The isotropic emitted  $\gamma$ -rays have an energy of 835 keV and undergo Compton scattering in the TPC with a Compton edge at 640 keV. During the calibration run, we recorded both, the anode signal and the energy deposit in the scintillator. The Compton edge is not visible with our energy resolution of 10% at 1 MeV, therefore the complete spectrum is used to determine the calibration. Several details are included, such as the geometry of the source holder and the absolute vertex position of the Compton scattering. The simulation of the Compton spectrum included the decay scheme of all possible daughter elements as well. In addition to the  $^{54}\text{Mn}$   $\gamma$ -source, we used  $^{137}\text{Cs}$  (662 keV) and  $^{22}\text{Na}$  (1274 keV) for the calibration.

Figure 3.8 shows the evolution of the calibration coefficients for the anode signal and the photomultipliers. The energy in keV is then obtained by

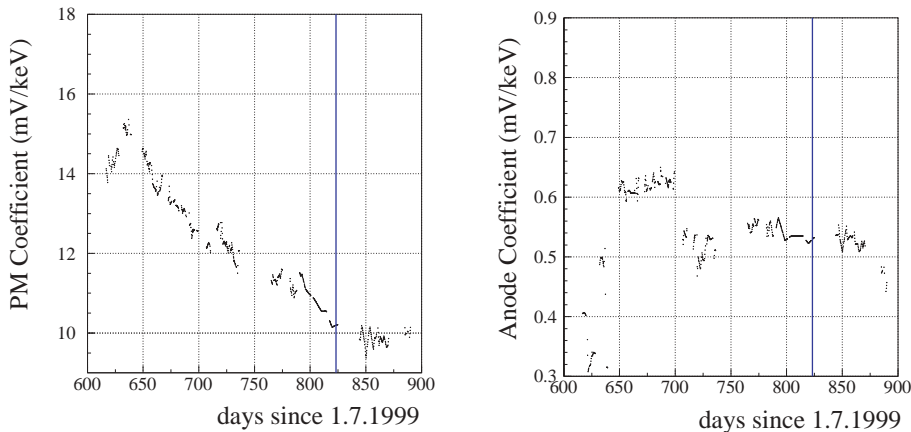


**Figure 3.8:** Calibration coefficients for the photomultipliers (left) and the anode (right). Runs taken before day 823 (vertical line) are with reactor ON, after this day the reactor is OFF.

dividing the recorded signal in mV units by the calibration coefficient:

$$T[\text{keV}] = \frac{\text{FADC integrated signal} [\text{mV}]}{\text{calibration coefficient}} . \quad (3.1)$$

The main problem is to explain the steps in the calibration of the anode and the degradation in the calibration of the avalanche light seen by the photomultipliers. This is not yet fully understood. More detail about the energy calibration can be found in ref. [39].

### 3.2.2 Drift time in the TPC and z-bin conversion

The drift time is an important parameter of the detector, and has to be measured. There are three different methods to determine the drift time: the first and preferred one uses the known position of a radioactive source; the second one uses the maximal drift time for electrons with a  $\gamma$ -ray; the last one uses horizontal muons which are traversing the full TPC from the anode to the cathode side. The three methods are used and documented in ref. [39]. For the last method, a special horizontal muon trigger has been implemented with the online filter of the data acquisition. By calculating the length of the anode signal, only muons with a length over 600 channels ( $z$ -bins) are accepted by the trigger, revealing horizontal muons. Figure 3.9 shows the time evolution of the drift time. Before day 700, the drift time

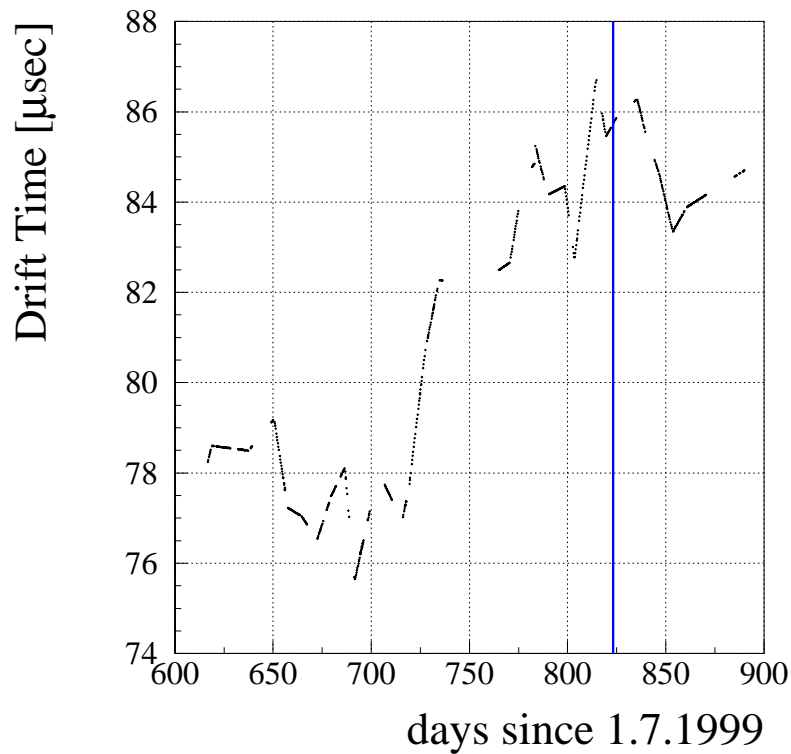


**Figure 3.9:** Drift time during data taking of 2001. The drift time is adapted to the  $80\mu\text{s}$  memory of the readout system. Runs taken before day 823 (vertical line) are with reactor ON, after this day the reactor is OFF.

is  $78\mu\text{s}$ , and increased to  $84\mu\text{s}$  afterwards. The drift time is used for the conversion of the  $z$ -binning (time) to a length: one  $z$ -bin corresponds to

80 ns (12.5 MHz clock), and the full drift region from the cathode to the anode side is 162 cm. The drift velocity  $v_D$  and the drift time  $T_D$  are then related by

$$v_D[\text{cm}/\mu\text{s}] = z\text{bin}[\text{cm}] \cdot 12.5 \text{ MHz} \quad , \quad T_D[\mu\text{s}] = \frac{162 \text{ cm}}{v_D[\text{cm}/\mu\text{s}]} \quad . \quad (3.2)$$

Replacing the drift velocity  $v_D$  in the equation of the drift time gives the length in cm for one  $z$ -bin:

$$z\text{bin}[\text{cm}] = \frac{162 \text{ cm}}{12.5 \text{ MHz} \cdot T_D[\mu\text{s}]} \quad . \quad (3.3)$$

For instance, with a  $78 \mu\text{s}$  drift time, one  $z$ -bin corresponds to 0.167 cm and 1024  $z$ -bins cover over 170 cm. At a higher drift time, e.g.  $84 \mu\text{s}$ , only 158 cm are covered. This is not problematic, as our electron tracks are shorter than 50 cm, and the trigger position is close to the centre of the TPC.

The drift time is used in the track reconstruction software to transform the  $xz$  and  $yz$  projections of an event in the correct scaled 3D space. This is important for the calculation of the scattering angle.

### 3.2.3 Determination of dead time

In this section, the dead time due to the hardware trigger and readout will be estimated and compared to the measured dead time.

First, the dead time due to the hardware trigger is estimated. The cosmic muon veto, see table 2.3, has a frequency of 260 Hz, with a veto time of  $200 \mu\text{s}$ . Hence, the dead time due to cosmic muons is the multiplication of the two values, and gives 5.2%. Similarly, the anti-Compton (AC) veto counter has a frequency of 710 Hz, and the width of the veto is  $80 \mu\text{s}$ . The corresponding dead time is 5.6%. The muon veto is often in coincidence with the anti-Compton veto, and therefore they contribute 6-10% in total. The dead time of the data acquisition can be estimated with the readout time per event, which is 2.5 seconds. The DAQ is writing with a 0.144 Hz rate on disc, and the dead time related to the readout is therefore 36%. The most important contribution to the total dead time is obviously the readout of the event, and only a small contribution is due to the anti-Compton. The estimated total dead time of the hardware trigger and data acquisition is 42-46%. This calculation does not take into account the coincidence between the readout of an event and the veto signal of the anti-Compton. Due to the coincidence (10% of 46%), the real dead time is around 40%. To determine the dead time, a direct measurement was developed.

A 120 Hz clock is used for the measurement of the dead time. The dead time is obtained from the number of tick counts during the readout busy time and anti-Compton veto signals, and from the number of total tick counts during the measurement time. With this method, we obtain a 40%

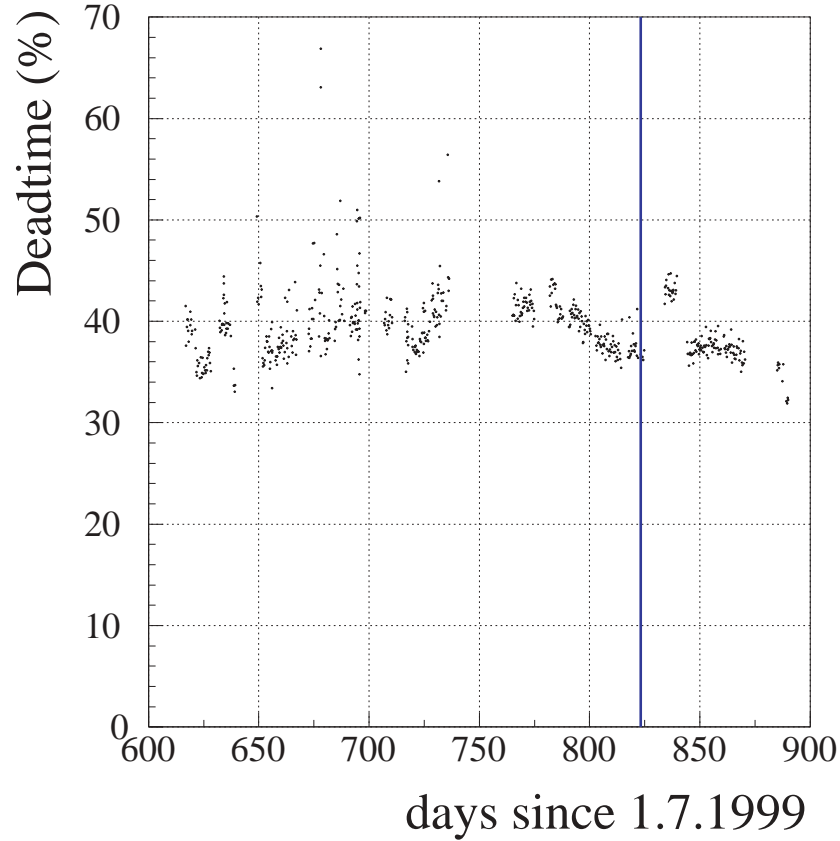


**Figure 3.10:** Dead time evolution since 1.7.1999. Each point represents a run. Runs taken before day 823 (vertical line) are with reactor ON, after this day the reactor is OFF.

dead time, which is compatible with the prediction given above. The time evolution of the relative dead time is shown in figure 3.10.

With the dead time, the effective live time can be obtained. During the period with reactor ON, we measured 109 days, corresponding to 66.3 days effective time. The background without reactor is measured during 31 days, corresponding to 19.3 effective time. Table 3.2.3 summarizes the results of the dead time calculation for the data taking period of 2001.

### 3.2.4 Measurement of the electron density

The slow-control of the MUNU experiment is done twice: First, a standalone version is measuring continuously the temperature and the pressure. The temperature inside the TPC is 28°C in summer and 24°C in winter. Moreover, the pressure (around 3 bar) is monitored, because the difference  $\Delta p$  between the anti-Compton and the TPC must not be larger than 80 mbar,

**Table 3.3:** Comparison between measured time and effective time of the data taking period 2001.

Period	Runs	Measured days	Effective days
ON	570	108.8	66.3
OFF	128	31.04	19.3

otherwise the acrylic structure would be stressed and probably damaged. Second, the slow-control is written for every event in the data file. This method allowed determining the pressure and temperature of the  $\text{CF}_4$  gas directly for each run. From the pressure  $p$  and temperature  $T$ , one obtains the electron density:

$$\rho_e = \frac{Zp}{kT} \frac{1}{c} . \quad (3.4)$$

In this formula,  $Z$  denotes the number of electrons for  $\text{CF}_4$  ( $Z = 42$ ),  $k$  the Boltzmann constant, and  $c$  the compressibility for a real gas. The compressibility for  $\text{CF}_4$  at  $25^\circ\text{C}$  and 3 bar is 0.9954, as given by ref. [40]. The volume of the TPC is  $1.0306\text{m}^3$ . From formula 3.4 we obtain the weighted number of electrons  $N_e$  in the TPC during reactor ON:

$$N_e = 3.25 \times 10^{27} .$$

The error is below 1%. Figure 3.11 shows the time evolution of the number of electrons during 2001, where each run is represented by a point.

### 3.2.5 Thermal reactor power

Another important information is the thermal reactor power. The data is provided by EDF in paper format, since no connection to the internal network of the power plant is allowed. Therefore, the reactor power is not directly build into the slow-control and a by hand assignment to each run is necessary afterwards. For the ON period 2001 the mean thermal reactor power is calculated for the 570 analysed runs and is found to be 2750 MW.

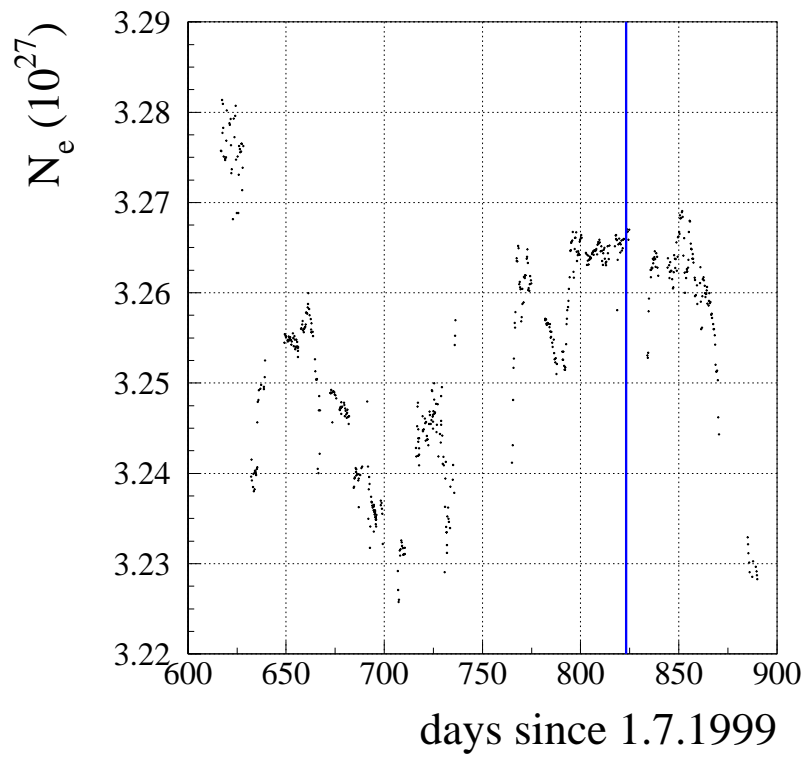


**Figure 3.11:** Number of electrons in the TPC. Each point represents one run. Runs taken before day 823 (vertical line) are with reactor ON, after this day the reactor is OFF.



*Track reconstruction*

The visual scanning was the first method to classify an event, to find the vertex and to fit the direction by eye. Because the visual scanning is time consuming, an energy threshold at 700 keV was applied to reduce the number of events. Based on the knowledge coming from the visual scanning an automatic tracking method was developed, which is described in this chapter.

The advantage of the visual scanning is a better event classification and background rejection. Electrons with two blobs on each track end, the so-called biblobs, are recognised in the eye scanning without problem. The automatic tracking cannot distinguish between start and end of a biblob electron, leading to a wrong vertex position in 50% of the cases. Due to the wrong vertex position, the direction fitted at this position is wrong as well. A kinematic event selection hence is not possible afterwards.

The advantage of the automatic tracking is the possibility to study systematically and with high accuracy its acceptance and efficiency with Monte Carlo simulations. In this chapter, the electrons were generated with an isotropic angular distribution and with a continuous energy spectrum. The vertex positions were distributed randomly in the TPC. The Monte Carlo simulation was used to determine the energy dependence of the angular resolution and to optimise the tracking parameters.

The final version of the tracking program was used to reconstruct the real data, corresponding to 66.3 days reactor ON and 19.3 days reactor OFF effective measuring time. With the automatic track reconstruction, we have access to the complete data at low energies, where more neutrino-electron scattering events due to the electromagnetic interaction are expected.

## 4.1 Automatic tracking

The automatic tracking, hereafter referred as track reconstruction, performs the following steps: finding of the event region in  $x$ ,  $y$  and  $z$ ; two passes of an iterative reconstruction of the trajectory in both projections  $xz$  and  $yz$ ; reconstruction of the vertex with a weight function; reconstruction of the event in three dimensions at the vertex position and angular fit.

### 4.1.1 Event region finding

First, the region of the event has to be found in  $x$ ,  $y$  and  $z$ . From the anode, the  $z$  position is obtained by the following procedure: A first iteration finds the region of  $z$ -bins above a threshold (50 mV), whereas isolated  $z$ -bins are ignored. The pedestal is obtained from the  $z$ -bins outside this region. In a second iteration, the anode region is refined with a threshold (6 mV) above the pedestal, see figure 4.1. To accept a  $z$ -bin as the start time of the signal, from the following  $z$ -bins 10 have to be above the threshold as well. A similar algorithm determines the region of the event in  $x$  and  $y$ . At the end, a margin is added to ensure that the event is fully contained in the region.

### 4.1.2 Iterative reconstruction of the trajectory

The trajectory is reconstructed in each projection plane with a set of points by the following iterative algorithm:

- The total contents in the event region is summed up, and the event is rejected if this sum (STRSUM) is below a given threshold. The sum is an important parameter at the end of the reconstruction.
- A box is moved over the projection in  $xz$ . The position for which the content is maximum corresponds to the start point of the reconstruction in the  $xz$  projection. For the second projection  $yz$ , the distance in  $z$  to the start point in  $xz$  has to be smaller than 20  $z$ -bins, corresponding to 3 cm. This pair is the high ionisation end of the electron and is marked with a blue star in figure 4.2. Then the amplitude within a box around the start region is set to zero to avoid backtracking. In addition, the total contents (STRSUM) in the event region is reduced by the contents of the deletion box.
- A box of 6 strips length (parameter RLENGTH) and 4 strips width is turned around the actual position. By this, the angle  $\phi$  of the box with the largest contents is obtained, see figure 4.3. The next point, marked by a black cross, is evaluated by going from the actual position in the direction of the angle  $\phi$  with a step size of 2 strips (parameter RSTEP). The content at the actual position is deleted because the

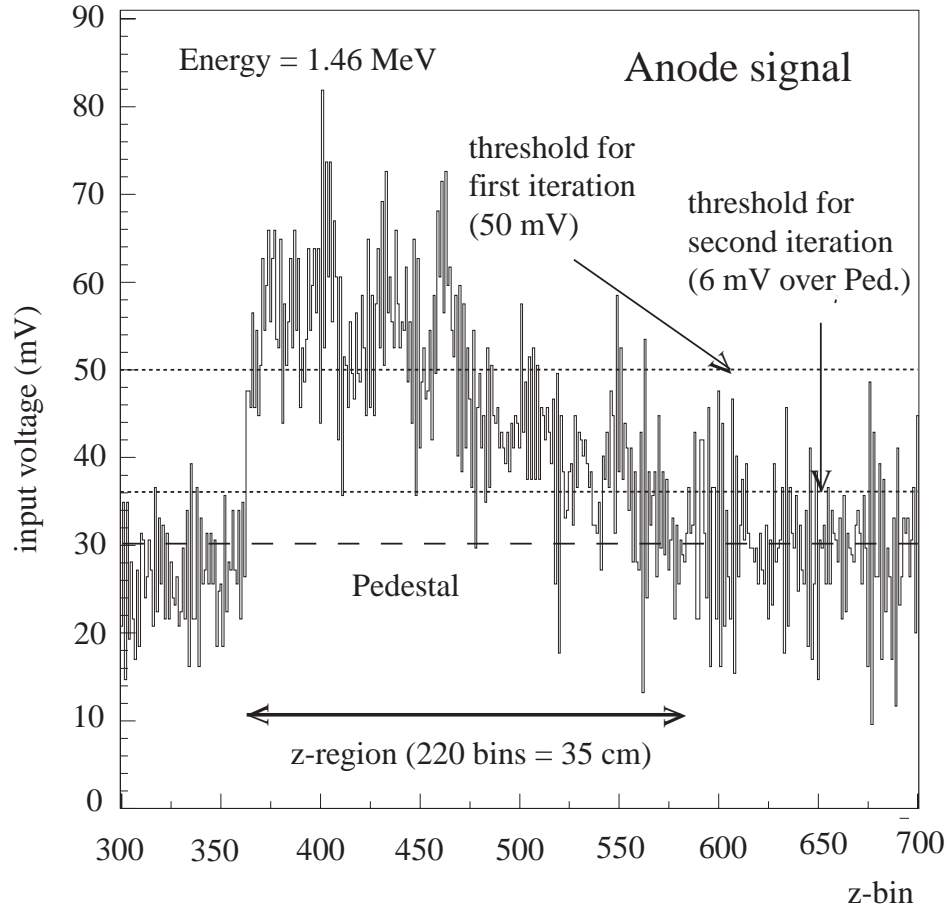


**Figure 4.1:** Anode signal of a 1.46 MeV electron. The pedestal is obtained in a first iteration (threshold 50 mV). The threshold for the second iteration is 6 mV above the pedestal. From the second iteration, the  $z$ -region is obtained (35 cm from  $z$ -bin 350 to 570).

information has been used already, and is subtracted from the total charge sum STRSUM. This step is repeated until the content of the rotation box gets below a threshold. For most events, the vertex is where the tracking ends. Vertex candidates are marked with green stars, see figure 4.3.

- For events with a gap in the track or with  $\delta$ -electrons, the end of the main track is generally not the vertex. Another track iteration is started if the remaining sum of the strip amplitude is more than 5% of the initial sum STRSUM. This explains that there are more than one vertex candidates (green stars).
- Higher track iterations, with at least 2 steps, are only accepted if the shortest distance to the main track is smaller than 35  $z$ -bins. All

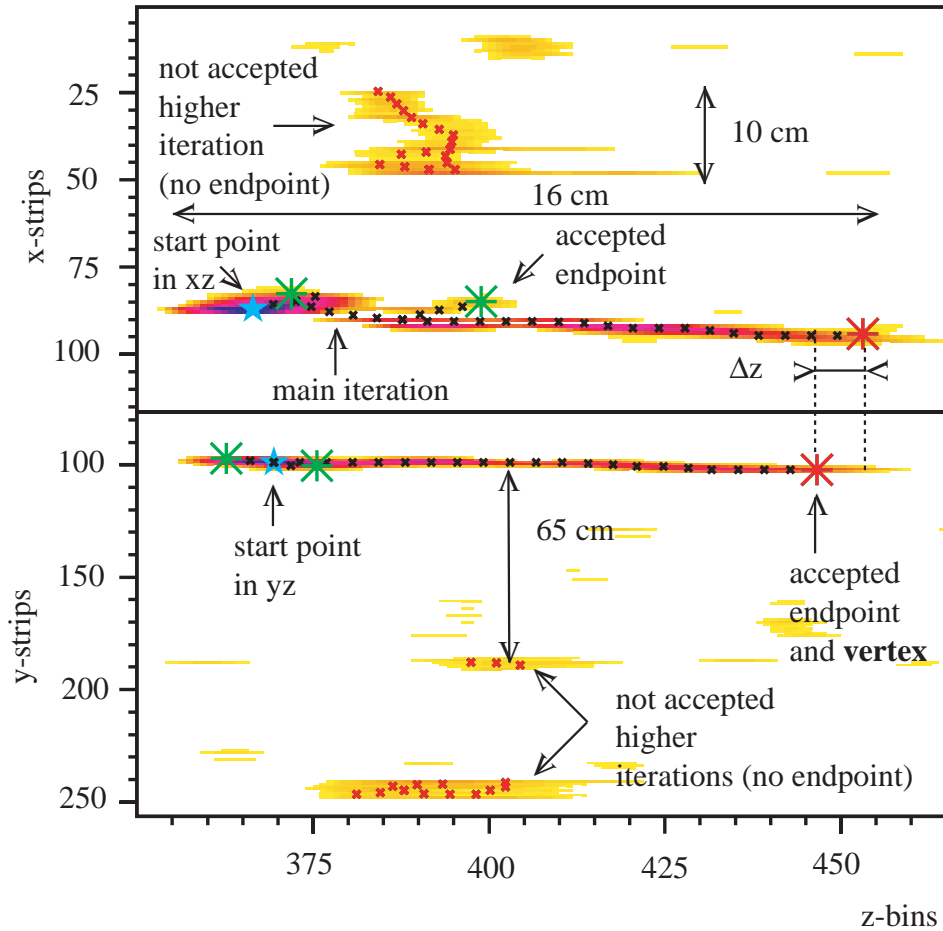


**Figure 4.2:** Real electron after the first reconstruction pass. Starting from the blue star, the small black points follow the trajectory towards the endpoints (green stars). The vertex, marked by a red star, is chosen amongst a pair of consistent endpoints, one in  $xz$  and one in  $yz$ .

higher iterations that not fulfil the condition are marked as not valid and the endpoints are not used as vertex candidates (see figure 4.2).

With this algorithm, the main trajectory and its higher iterations are reconstructed with a set of points. The invalid parts of the track are usually electronic noise, and can be rejected. Therefore, a better event region can be obtained from the accepted iterations. A second pass of the tracking algorithm is performed in the new region, as shown in figure 4.4. The improvement in the angular resolution is in the order of a few degrees, see section 4.2.

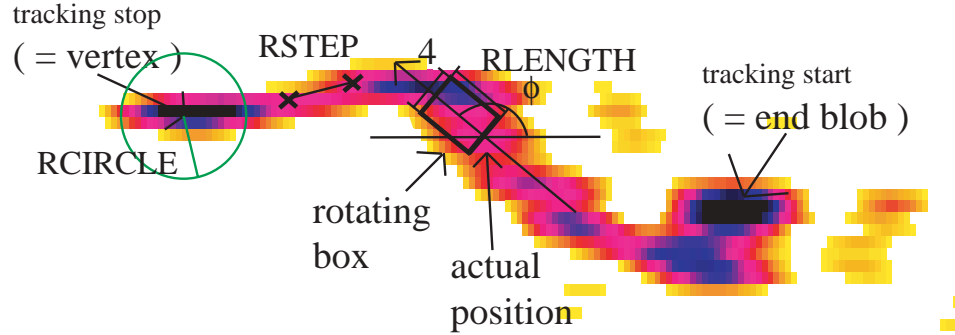


**Figure 4.3:** illustration of the track reconstruction. The parameters  $RSTEP$  and  $RLENGTH$  control the behaviour of the tracking, whereas the parameter  $RCIRCLE$  is important for the angular fit. In this example, the fit-radius is shown in a projection, but in the program it corresponds to the radius of the sphere in 3D at the vertex position.

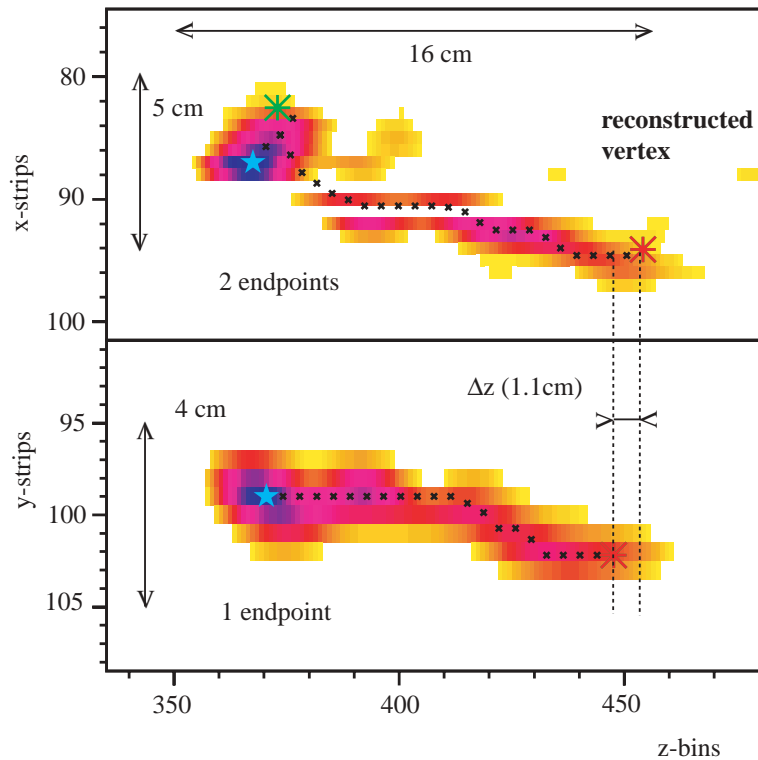


**Figure 4.4:** Real electron after the second pass of the trajectory reconstruction. The track ends are again marked with green stars, whereas the vertex-candidate is in red.

### 4.1.3 Vertex reconstruction

The vertex candidate is determined after the second pass of the trajectory reconstruction by the following method. All valid endpoints in the  $xz$  projection are tested against all endpoints in the  $yz$  projection by calculating the weight function

$$p = e^{-|\Delta z/\delta|} \times e^{-\rho_{xz}\rho_{yz}/\rho_n^2} \quad , \quad (4.1)$$

where  $\Delta z$  is the difference in  $z$ -bins along the  $z$  direction and  $\rho_{xz}$  is the ionisation within a circle of 8 strips radius around the candidate in the  $xz$  projection. The normalisation constant  $\delta$  for the  $z$  direction is set to 2.5  $z$ -bins, corresponding the resolution in  $z$ . To determine the normalisation  $\rho_n$  for the ionisation, a special tracking run without vertex reconstruction was used. The ionisation around the generated vertex was then calculated, and the normalisation was set to the mean value of the distribution, see figure 4.5. The pair with the highest weight  $p$  is selected as the vertex, because the

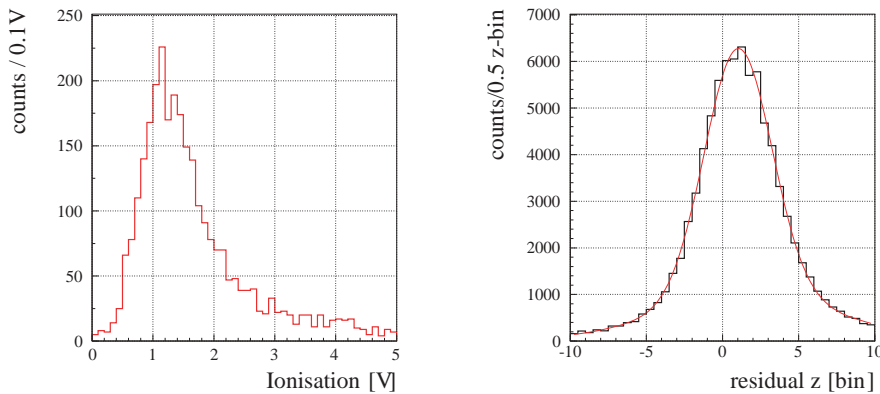


**Figure 4.5:** Determination of the normalisation constants. Left: Ionisation within a circle of 8 strips radius around the true vertex. Right: Vertex resolution and Gaussian fit in  $z$ . One  $z$ -bin corresponds to 0.2 cm. (Monte Carlo simulation).

vertex is characterised by a low energy deposition and a small  $\Delta z$ . The  $\Delta z$  term in the weight function permits to reject combinations between endpoints due to uncorrelated electronic noise in  $xz$  and  $yz$ . In addition, the selection of the track end as vertex is suppressed by the ionisation density term in the weight function. The weight function distribution of the selected vertex for 3000 electrons is shown in figure 4.6. Only 4% of all reconstructed events have a weight smaller than  $10^{-10}$ . This events have mostly a large  $\Delta z$  and can be rejected with a cut on the weight, e.g. at  $10^{-7}$ .

The vertex weight can be used to study the angular resolution, see section 4.2. Figure 4.7 shows the dependency of the angular resolution  $\sigma_\theta$  as a

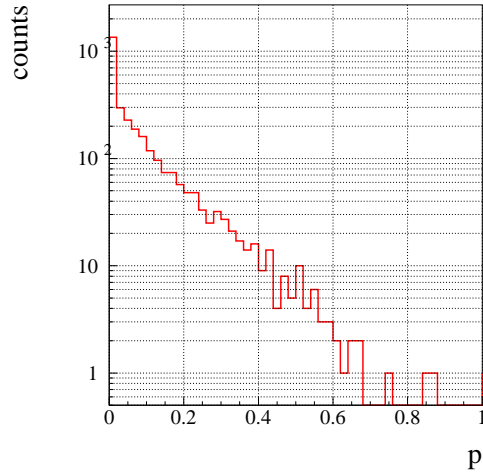


**Figure 4.6:** Distribution of weights  $p$  for 3000 events. (Monte Carlo simulation).

function of the cut on the vertex weight  $p$ . The angular resolution was found to vary from  $25^\circ$  without cut,  $24^\circ$  for  $p > 10^{-7}$ ,  $21.5^\circ$  for  $p > 10^{-4}$ , to  $18^\circ$  for  $p > 10^{-2}$ . The angular resolution of events with a high vertex weight is close to the resolution obtained with the true vertex ( $15^\circ$ ).

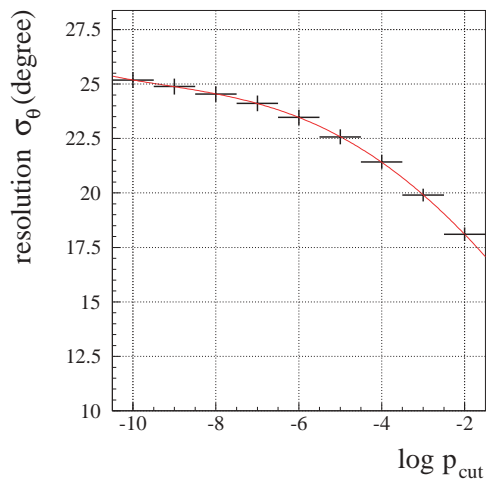


**Figure 4.7:** Angular resolution in  $\theta$  as a function of the cut on the vertex-weight  $p$ . The angular resolution obtained with the true - generated - vertex position is  $15^\circ$ . (Monte Carlo simulation).

For a good efficiency of the vertex determination, it is important to not have too many endpoints. By comparing figures 4.2 with 4.4, we count three endpoints in each projection after the first pass, and only one in  $xz$  and two in  $yz$  after the second pass of the trajectory reconstruction. This fact explains why the second pass is important for the vertex determination, and

thus why the angular resolution is improved.

#### 4.1.4 Spatial resolution of the vertex

The spatial vertex resolution was determined with a Monte Carlo study by combining the spatial information from the strips with the  $z$  position. The averaged distance for energies between 0.3 MeV and 1.3 MeV is 0.75 cm, as shown in figure 4.8. The distributions in the  $x$ ,  $y$  and  $z$  directions are however as expected Gaussian.

With the spatial resolution, figure 4.8, we can determine the efficiency of the vertex reconstruction. For one half of all events, the distance between the true - generated - vertex and the reconstructed vertex is less than 1 cm. Therefore, the vertex reconstruction is the limiting factor in the automatic scanning method. If the vertex is not recognised within 1-2 cm, then the angular direction fit produces no meaningful result, because the radius used by the fit is 3.9 cm. An improvement of the trajectory reconstruction would lead to a better vertex reconstruction and thus to a better angular resolution and finally to a better kinematical selection.

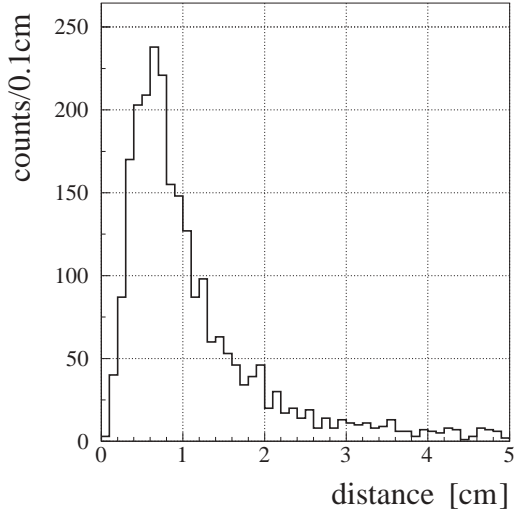


**Figure 4.8:** Distribution of the distance between true and reconstructed vertex for 3000 Monte Carlo events, generated with GEANT.

The spatial resolution of the vertex position depends slightly on the energy of the event. Low energy means short tracks and more multiple scattering. Above 700 keV the resolution in space is 0.7 cm, and increases up to 0.8 cm with decreasing energy. The distance of 0.7 cm corresponds to 2 strips only. The energy dependency of the resolution will play a crucial role in the determination of the acceptance of the neutrino electron scattering. More about this in the chapter 5. Moreover, the resolution depends on the electronic noise. The electronic noise is reduced twice, first by a Fourier transformation

and secondly by the tracking program due to the two passes of trajectory reconstruction. Further degrading in the resolution comes from dead strips, because a gap in the track leads to more iterations in the reconstruction, and therefore more combinations of endpoints have to be calculated. In this case the weight function calculation helps to reject bad endpoint combinations with the distance  $\Delta z$ , since a gap in the trajectory exists only in one projection and not in both.

## 4.2 Angular fit in 3D

The angular fit algorithm combines for each  $z$  position the strips from both projections if their amplitude is above a threshold (parameter IXYCUT = 60 mV). This threshold is used to suppress electronic noise near the vertex position. The 3D-region around the vertex position is then used to obtain the angles  $\phi_{\text{det}}$  and  $\theta_{\text{det}}$  directly with a least squares fit (MINIUT [41]). The angle  $\phi_{\text{det}}$  is defined from the y-axis, and the angle  $\theta_{\text{det}}$  is with respect to the negative  $z$ -axis. Be aware, that the  $z$ -axis goes from the anode to the cathode, see figure 4.9.

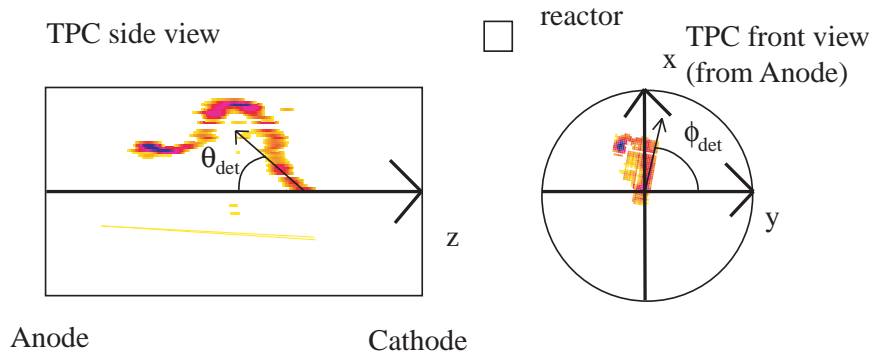


**Figure 4.9:** Definition of the angles  $\phi_{\text{det}}$  and  $\theta_{\text{det}}$  in the detector reference frame.

All points in a circle with radius 3.9 cm (RCIRCLE = 11 strips) around the vertex are used with their amplitude as weight. The fit parameters  $\phi_{\text{det}}$  and  $\theta_{\text{det}}$  are bound from  $-180^\circ$  to  $180^\circ$ , and from  $0^\circ$  to  $180^\circ$  respectively. This is important, because otherwise the angles lie largely outside the physical region and a renormalization of the angles into the restricted range is not precise enough.

The fit method gives only the angles  $\phi_{\text{det}}$  and  $\theta_{\text{det}}$ , but not the absolute direction  $\vec{v}$  of the event: a straight line fit cannot distinguish between the direction  $\vec{v}$  and  $-\vec{v}$ . The absolute direction has to be determined afterwards by comparing the content of two boxes, starting from the vertex position

and going in the direction  $\vec{v}$  and  $-\vec{v}$ , and then taking the direction for which the content is maximum. This process is called direction flip.

#### 4.2.1 Boundaries and convergence of the fit

The angular distribution in  $\phi_{\text{det}}$  is peaked near the boundaries after the fit, see figure 4.10 (left). The peak at  $\phi_{\text{det}} = 0^\circ$  corresponds to events flipped from  $\phi_{\text{det}} = 180^\circ$ . Similarly, the distribution in  $\cos\theta_{\text{det}}$  is peaked at  $\pm 1$ , corresponding to the direction along the z-axis. Moreover, events close to the boundaries have generally a bad fit (convergence) status, which is provided by MINUIT. The angular resolution in  $\phi_{\text{det}}$  for events with converged fit is  $24^\circ$ , and for events with bad fit status  $32^\circ$ , respectively.

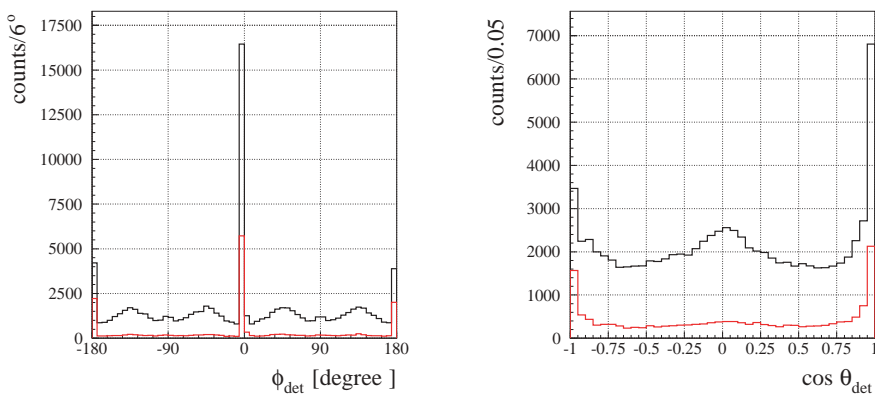


**Figure 4.10:** Angular distributions after the first iteration. Angular distribution in  $\phi_{\text{det}}$  (left) and  $\cos\theta_{\text{det}}$  (right) for all events (black histograms) and for the events with wrong fit status (red histograms). Monte Carlo simulation.

Thus, a second fit is done with new start parameters to reduce the peaks at the limits. The new start parameters are selected carefully by taking the directions from the first fit into account. If one of the angles, e.g. the angle  $\phi_{\text{det}}$ , is close to a boundary, but the second angle  $\theta_{\text{det}}$  is away from a boundary, then only the angle  $\phi_{\text{det}}$  is changed for the second fit. Both angles are changed simultaneously if both are close a boundary.

In figure 4.10, 20% of the events are close to a boundary. After the second iteration, still 20% of the first 20% events are close to a boundary, hence the number of wrong fitted events dropped down to 4%. This is after a third iteration reduced to a negligible small amount of events. The resulting angular distribution in  $\phi_{\text{det}}$  is shown in figure 4.11, and the peaks at  $\phi_{\text{det}}$  close to  $0^\circ$  and  $180^\circ$  are disappeared. The angular resolution in  $\phi_{\text{det}}$  was improved after the third iteration by 3-4 $^\circ$ .

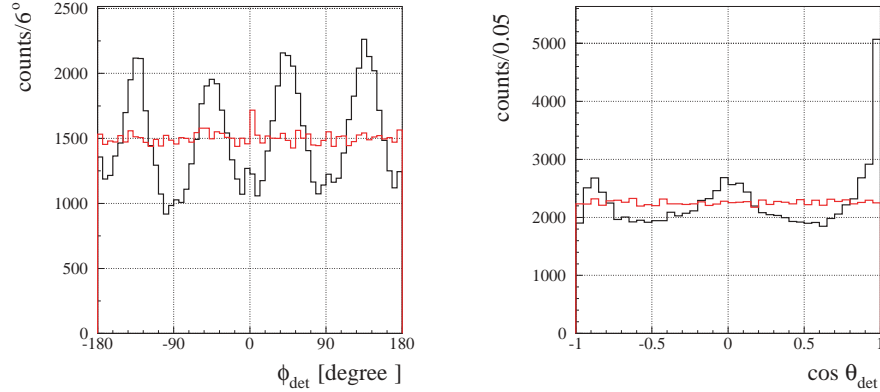


**Figure 4.11:** Angular distributions after the third iteration (black histogram), together with the generated distributions (red histogram).

#### 4.2.2 Peaks in the $\phi_{\text{det}}$ distribution

Unfortunately, new peaks in the  $\phi_{\text{det}}$  distribution appeared at angles  $\pm 45^\circ$  and  $\pm 135^\circ$ , as shown in 4.11 (left). These peaks were already present after the first angular fit, see figure 4.10 (left).

The following explanation was found for the structure in the  $\phi_{\text{det}}$  distribution: events parallel to the  $xy$ -plane are difficult to fit, because the correlation between  $x$  and  $y$  is not provided by the  $z$ -direction. Figure 4.12 (left) shows the projections in  $xz$  and  $yz$  for a typical event parallel to  $xy$ -plane. For this kind of event, each strip in  $x$  (e.g. from 120 to 150) has to be combined with each strip in  $y$  (e.g. from 130 to 150), because the correlation between the strips is missing. After calculating all possible combinations, a 2 and 3 dimensional picture of the event can be reconstructed. The result of the 2 dimensional reconstruction is given in figure 4.12 (right), with the Monte Carlo direction marked in blue. The combination of all  $x$  and  $y$  strips leads to a rectangular box in the  $xy$ -projection, and the 3D fit - in red - was performed at the reconstructed vertex in the left top corner of the box. All pixels in the  $xy$  plane, which are taken into account for the fit, are marked in addition with a black border. The fit radius is set to 11 strips and is also indicated in the display. For this event, the direction with the smallest  $\chi^2$  is close to  $-45^\circ$ , explaining the angular distribution in  $\phi_{\text{det}}$ . The missing correlation between  $x$  and  $y$  for events parallel to the  $xy$ -plane is the reason for the systematic attraction to angles  $\pm 45^\circ$  and  $\pm 135^\circ$ , shown in 4.11 (left).

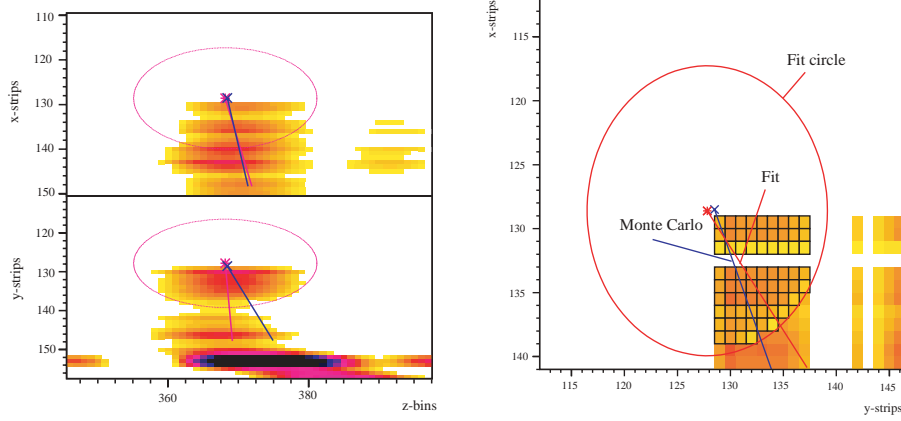


**Figure 4.12:** Typical event parallel to the  $xy$ -plane. The Monte Carlo direction is shown in blue, the 3D angular fit in red.

### 4.2.3 Angular resolution in space

The angular resolution in  $\phi_{\text{det}}$  and  $\theta_{\text{det}}$  is obtained from the difference between the generated and reconstructed angle. The angular resolution of the two angles is Gaussian centred at zero, as expected. They are limited by the following reasons:

- Physical reasons: multiple scattering and diffusion.
- Detector related: such as binning, induction on strips, electronic rise time and noise.
- Program related: mainly due to un-precise vertex determination.
- Angular fit related: peaks in  $\phi_{\text{det}}$  distribution.

The angular resolution in space  $\sigma_{3D}$  can be calculated by comparing the direction in space

$$\vec{v} = \begin{pmatrix} \sin \theta_{\text{det}} \sin \phi_{\text{det}} \\ \sin \theta_{\text{det}} \cos \phi_{\text{det}} \\ \cos \theta_{\text{det}} \end{pmatrix} \quad (4.2)$$

to the generated direction  $p_{\text{MC}}$  ( $\cos \alpha = \vec{v} \cdot p_{\text{MC}}$ ). The distribution of the angle  $\alpha$  between the true and reconstructed direction is shown in figure 4.13. For normal distributed angles  $\phi_{\text{det}}$  and  $\theta_{\text{det}}$  the  $\alpha$  distribution is Gaussian multiplied with a sine:

$$c \cdot \sin \alpha \times e^{-\frac{1}{2} \left( \frac{\alpha}{\sigma_{3D}} \right)^2} \quad . \quad (4.3)$$

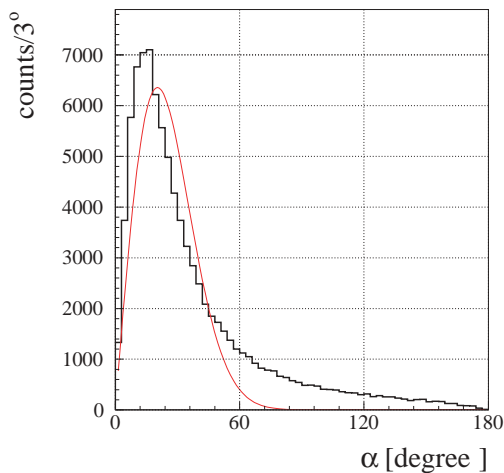


**Figure 4.13:** Distribution of the difference between simulated and reconstructed recoil angle. The theoretical distribution is shown by a red line.

#### 4.2.4 Energy dependence of the angular resolution

The angular resolution in space was determined as a function of the kinetic energy of the recoil electron, from 0.3 MeV to 1.3 MeV with a 100 keV binning. Figure 4.14 shows the angular resolution in space versus the electron energy. The angular resolution at high energy is better than at low energy, mainly due to multiple scattering, which is dominant at low energies. A further contribution comes from the worse vertex resolution at low energies. To study the effect of the angular fit alone, the vertex was taken directly from the Monte Carlo and the direction was fitted at this position. Therefore, there are no effects due to the trajectory and vertex reconstruction. The angular resolution in this situation (of only fit) is  $5^\circ$  better for all energies compared to the full track reconstruction. The energy dependency is still present in the case of the angular fit with the true vertex. The energy dependency can be described by

$$\sigma_{3D} = A/T + B \quad , \quad (4.4)$$

where T is the kinetic energy of the electron.

The quoted resolutions in table 4.1 are averaged over all directions, since the MC events were generated isotropically.

#### 4.2.5 Anisotropy of the angular resolution

The angular resolution is not homogeneous in our detector, events in  $z$ -direction have a better resolution than events parallel to the  $xy$ -plane. The dependency of the angular resolution as a function of the angles  $\phi_{\text{det}}$  and  $\cos\theta_{\text{det}}$  is illustrated in figure 4.15.

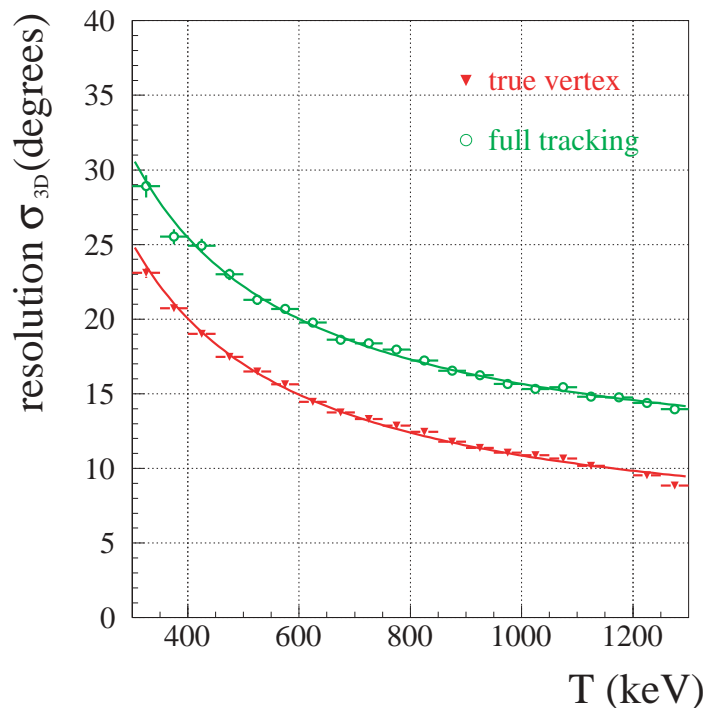


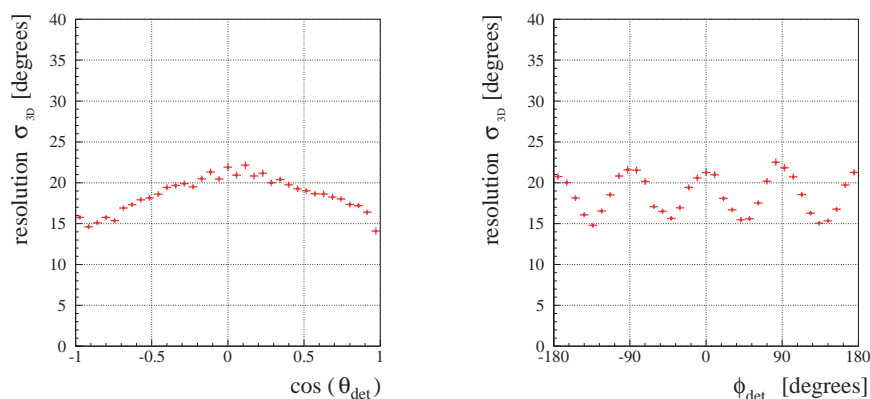
**Figure 4.14:** Angular resolution in space as a function of electron recoil energy. Red curve: 3D angular fit with true vertex; green curve: reconstruction and 3D angular fit. The green curve is relevant for the comparison with real data.

The dependency of the angular resolution on  $\phi_{\text{det}}$  (figure 4.15 right) can be understood with the explanation of the peaks in the  $\phi_{\text{det}}$  distribution. An event parallel to the  $xy$ -plane ( $\cos \theta_{\text{det}} = 0$ ) with an angle  $\phi_{\text{det}} = 45^\circ$  will be attracted to its own direction, leading to a small difference between the reconstructed and the generated direction. Hence, the angular resolution in space is small at  $\phi_{\text{det}} = 45^\circ$ . An event with an angle  $\phi_{\text{det}} = 0^\circ$  or  $90^\circ$  (parallel to the cardinal direction  $x$  or  $y$ ) will be pushed systematically to  $45^\circ$ , leading to a large difference between the reconstructed and the generated direction.

For events with a non vanishing  $z$  component ( $\cos \theta_{\text{det}} = \pm 1$ ), the  $x$  and  $y$  strips are correlated, and therefore the direction in  $\phi_{\text{det}}$  can be fitted with a higher precision, see figure 4.15 (left). For MUNU this had to be taken into account because neutrinos enter the TPC in the direction parallel to the  $xy$ -plane with  $\theta_{\text{det}}$  close to  $90^\circ$ , where the resolution is poor.

**Table 4.1:** Energy dependence of the angular fit.

Energy	fit only	reconstruction and fit
300 keV	25.1°	30.9°
500 keV	17.0°	22.2°
700 keV	13.5°	18.4°
1000 keV	10.9°	15.2°

**Figure 4.15:** Angular resolution as a function of  $\cos \theta_{\text{det}}$  and  $\phi_{\text{det}}$ . Monte Carlo simulation.

#### 4.2.6 Reconstruction of the scattering angle $\theta$

From the two angles  $\phi_{\text{det}}$  and  $\theta_{\text{det}}$  a vector  $\vec{v}$  from the vertex in the event direction can be calculated, as explained already before. Similarly the angles  $\theta_r = 90^\circ$  and  $\phi_r = -47.25^\circ$  can be used to calculate the  $\vec{r}$  vector, which is the direction from the reactor core to the centre of the TPC:

$$\vec{r} = \begin{pmatrix} \sin \theta_r \sin \phi_r \\ \sin \theta_r \cos \phi_r \\ \cos \theta_r \end{pmatrix} \quad (4.5)$$

The scalar product of the two vectors  $\vec{v}$  and  $\vec{r}$  gives the scattering angle  $\theta$  of the event,

$$\cos \theta = \vec{v} \cdot \vec{r} \quad (4.6)$$

The scattering angle  $\theta$  is the angle between the two vectors  $\vec{r}$  and  $\vec{v}$ , which constructs the forward and backward cones. The scattering angle is important for the event selection, as electrons from a neutrino scattering are always contained in the forward cone, see figure 4.16. The opening angle of the cone depends on the incident neutrino energy, but is typically 40-60°.

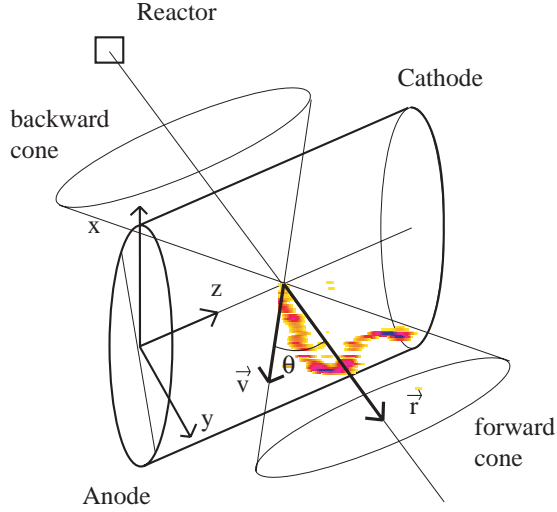


**Figure 4.16:** Scattering angle  $\theta$ . The scattering angle is defined as the angle between the reactor direction  $\vec{r}$  and the electron direction  $\vec{v}$ .

Figure 4.17 (left) shows the obtained angular distribution for isotropically generated electrons. The energy was generated uniformly distributed between 0.3 MeV and 1.3 MeV. The distribution is not flat because the angular distributions in  $\phi_{\text{det}}$  and  $\cos\theta_{\text{det}}$  are not isotropic as well. In the forward cone ( $\cos\theta \simeq 1$ ), signal and background events will be observed. In the backward cone ( $\cos\theta \simeq -1$ ) there are only background events. The angular resolution is  $24^\circ$ , as shown in figure 4.17 (right).

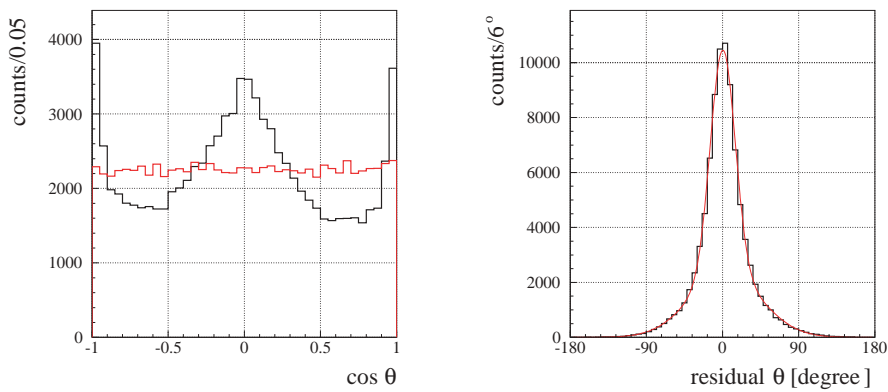


**Figure 4.17:** Left: angular distribution of the reconstructed (black) and generated (red) scattering angle. Right: angular resolution of the scattering angle (black) with gaussian fit (red). Monte Carlo simulation.

### 4.3 Real data angular distributions

The track reconstruction was applied to the real data, corresponding to 66.3 days reactor ON and 19.3 days reactor OFF. We expect an isotropic angular distribution since background electrons from internal radioactivity (35 mHz at 300 keV, see section 3.1) dominate the real data. Figure 4.18 shows the obtained distribution for the reactor ON period, normalised to 1 day of data taking.

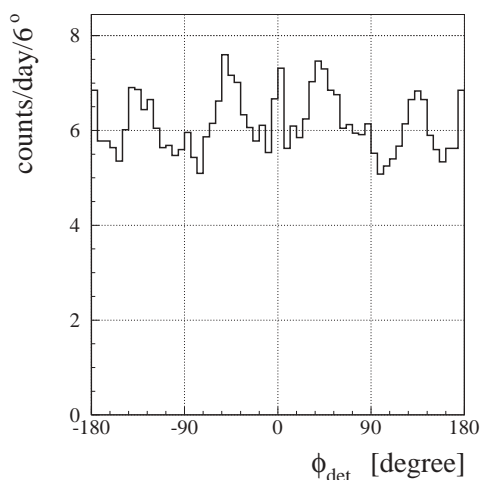


**Figure 4.18:** Measured angular distribution in  $\phi_{\text{det}}$  for 66.3 days reactor ON.

The structure in  $\phi_{\text{det}}$  is due to the missing correlation between  $x$  and  $y$  for events parallel to the  $xy$ -plane, as explained in section 4.2.2. The same structure was observed in the angular distribution of isotropically generated MC events (see figure 4.11). The reactor forward direction is centred at an angle  $\phi_{\text{det}} = -45^\circ$ , whereas the opposite (backward) direction is centred at  $\phi_{\text{det}} = 135^\circ$  (see figure 4.19). The direction  $\phi_{\text{det}} = -135^\circ$  is used for calibration runs, since this direction corresponds to electrons coming from the source holder (located at  $45^\circ$ ). In neutrino runs, no contamination is recorded coming from this position.

During 1999 and early 2000, we collected data with a Radon contaminated Oxisorb filter [42], leading to a strong event isotropy, peaking at the cathode side. Activity measurements confirmed that the zeolites in the Oxisorbs contained much higher quantities of uranium than foreseen. Therefore, we have replaced the filters by low background ones in winter 1999. The counting rate for  $\alpha$ 's in the gas dropped by a factor  $10^5$ , from 35 to a negligible  $5 \cdot 10^{-3}$  Hz, while the counting rate for  $\alpha$ 's emerging from the cathode remained constant at about 0.05 Hz. The position of a  $\alpha$  particle can be measured from the time difference between the light pulse generated by the scintillation of  $\text{CF}_4$  and the light pulse from the avalanche at the anode. A typical event is shown in

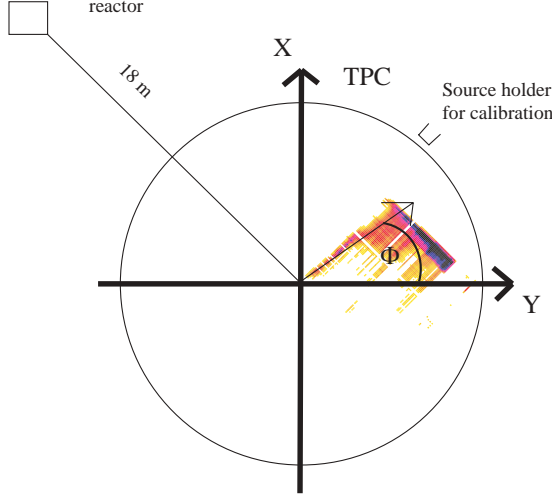
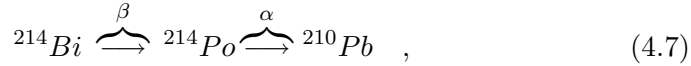
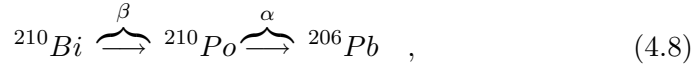


**Figure 4.19:** The angle  $\phi_{\text{det}}$  in the TPC is defined with respect to the y-axis. Events caused by a neutrino-electron scattering are expected at angles  $\phi_{\text{det}}$  close to  $-45^\circ$ . Events from the source holder are expected at angles  $\phi_{\text{det}} = -135^\circ$ .

the figure 4.20, which was traced to the presence of  $^{214}\text{Bi}$  implanted on the high voltage cathode surface. This nuclide decays as



where the  $\alpha$ -decay has a very short mean lifetime of 0.2 ms. The nuclide  $^{210}\text{Pb}$  decays to  $^{210}\text{Bi}$  and successively to  $^{206}\text{Pb}$  via the chain



where the second decay has a mean lifetime of 200d. This time, the electron is not observed in coincidence in the TPC with the  $\alpha$  particle and therefore fakes a neutrino event. Therefore, in March 2000 the cathode was exchanged additionally. Almost all electrons from the Radon contamination disappeared, and the counting rate for  $\alpha$ 's from the cathode side dropped by a factor  $10^2$  to an acceptable  $5 \cdot 10^{-4}$  Hz.

The anode side of our detector is more complicated and therefore more background is expected from this side. Therefore, the angular distribution in  $\cos\theta_{\text{det}}$  is not isotropic, see figure 4.21. On one hand, the distribution is attributable to the non-isotropic response of the angular fit, especially at the boundaries. On the other hand, part of the enhancement at  $\cos\theta_{\text{det}}$  close to  $-1$  ( $\theta_{\text{det}} = 180^\circ$ ), is due to the electrons from the anode side, as explained before. This enhancement was not so strong for an isotropic Monte Carlo simulation with GEANT. For that reason all events from the anode side with  $\theta_{\text{det}} > 100^\circ$  were eliminated.

The angular distribution of the scattering angle  $\cos\theta$  is shown in figure 4.22 for both periods, reactor ON and OFF. The kinematic forward direction is at values of  $\cos\theta$  between 0.7 and 1. In this region, we observe a peak.

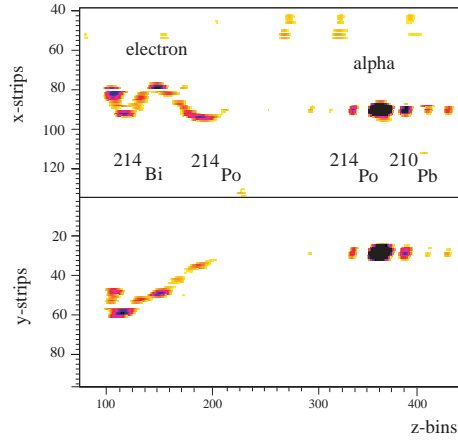


**Figure 4.20:** Background  $\beta-\alpha$  event showing the  $^{214}\text{Bi}$  contamination implanted on the cathode surface. This type of event disappeared after the cathode exchange in March 2000.

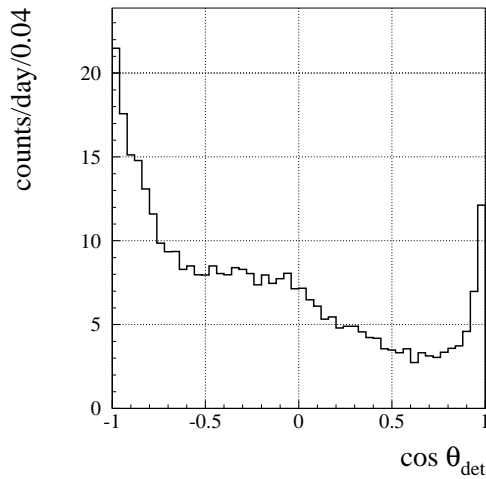


**Figure 4.21:** Real data angular distribution in  $\cos \theta_{\text{det}}$  for 66.3 days reactor ON.

This peak is also visible in the reactor OFF data and in the Monte Carlo simulation of isotropic generated events.

#### 4.4 Discussion

The automatic track reconstruction program from Tadsen [43] was improved significantly, especially in the event finding, the vertex reconstruction and the angular fit in 3D. In particular:

- The Monte Carlo program was extended with true electronic noise. With the aid of the realistic Monte Carlo simulation, a new event

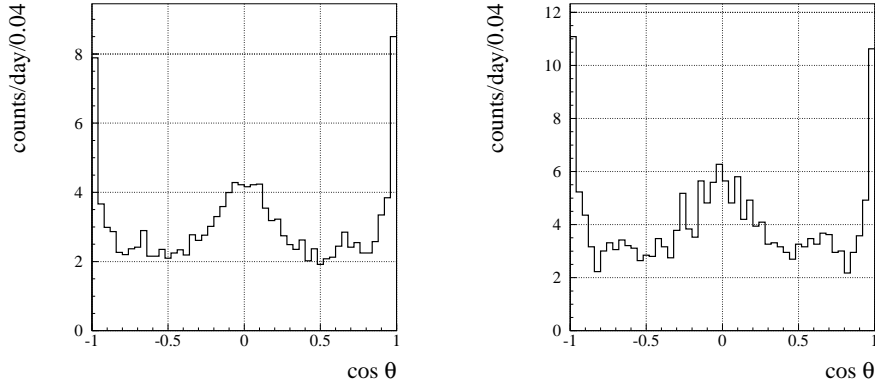


**Figure 4.22:** Scattering angle for reactor ON (left) and reactor OFF (right).

localisation was developed, able to recognise and reject electronic noise. This improved significantly the resolution by 3-4°.

- The angular distribution in  $\phi_{\text{det}}$  was understood and became comparable to the distribution obtained by the visual scanning.
- The distribution in  $\cos \theta_{\text{det}}$  was almost flat for isotropic generated events. The angle  $\theta_{\text{det}}$  could be used to eliminate background from the anode side, see appendix C.12.
- The distribution of the scattering angle  $\cos \theta$  was comparable to the distribution obtained by visual scanning.
- Higher acceptance and better angular resolution were obtained due to the iterative angular fit in 3D.

The tracking parameters were tuned with Monte Carlo simulated electrons. The angular resolution in space and the vertex resolution were then plotted versus the parameter. The optimal value of the tracking parameter was obtained from the position, where the resolution was minimal. Details about the optimisation can be found in appendix A.5. The optimal parameters are summarised in table 4.2. They were then used for tracking the real data.

The visual scanning was compared to the automatic tracking, which is an important part for understanding the event classification. Moreover, the main problem of the automatic tracking was the so-called biblob electrons. This type of event has to end blobs; hence, no low ionisation vertex is visible. The automatic tracking is not able to reject these electrons, thus increasing the background significantly. A possible solution is the use of the eye classification.

**Table 4.2:** Tracking parameters

Parameter	value	Description
RSTEP	2 strips	Step size between two track points
RLENGTH	6 strips	Length of rotation box
RWDEL	8 strips	Length of static deletion box
BXFRAC	0.05	Fraction of the initial charge deposition
RSTART	8 strips	Ionisation density radius
IXYCUT	60 mV	Reconstruction threshold for 3D fit
RCIRCLE	11 strips	Fit length around vertex
ZBIN	0.15-0.19	binning in z, depends on the drift speed.

With the automatic tracking all real data were reconstructed. For the visual scanning, only events with energies above 700 keV are analysed. However, the information from the automatic tracking could be used to reduce the enormous amount of data at lower energies in the order of 60%. The acceptance of the neutrino signal would be still 90%, as shown in appendix C.12.



## *Monte Carlo Simulation*

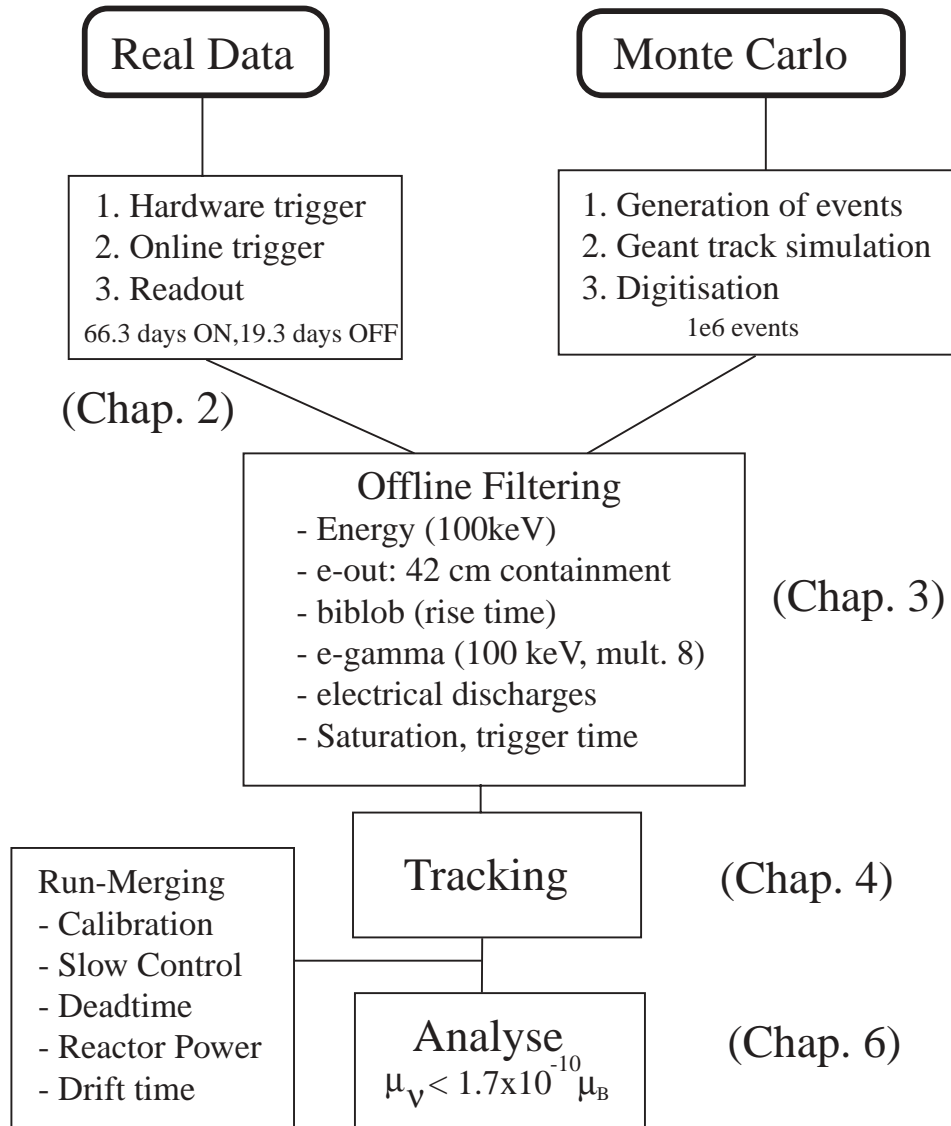
The Monte Carlo simulation was used to predict the electron energy spectrum and thus the counting rate for  $\bar{\nu}_e e^-$  scattering. The expected energy spectrum of the recoil electron can then be compared directly with the measured spectrum, see chapter 6.

Figure 5.1 illustrates the processing for real data and Monte Carlo events. In the first step of the Monte Carlo program, the counting rate and electron energy spectrum was obtained from the differential cross section and from the known reactor antineutrino flux. In the second step, the detector geometry and the energy and angular resolution were taken into account by simulating the tracks of recoil electrons with GEANT3 [44]. In the last step, the generated tracks were digitised and written in the data format of the real data. True electronic noise was included as well.

Both, real data and Monte Carlo generated events were filtered and tracked. By this, the acceptance of the offline filter and track reconstruction was included in the prediction. The acceptance of the tracking software for recoil electrons from  $\bar{\nu}_e e^-$  scattering was presented in section 5.2, whereas the determination of the acceptance of the offline filter was already discussed in chapter 3.

### *5.1 The Monte Carlo simulation*

The Monte Carlo simulation program for the MUNU detector consists of three separate parts. In the first part, antineutrinos from the nuclear reactor were simulated, including the energy and angular distribution. The next part was based on GEANT, in which the track of the recoil electron in the detector was simulated. The physics of the photo effect, the Compton scattering and Pair production were taken into account, and multiple scattering



**Figure 5.1:** Simulation and measurement. The offline filter and the tracking software were used for both real data and Monte Carlo generated events.

determines the trajectory of the electrons. The generated electron track was then digitised in the last (third) part to have the same data format as in the real data, including the electronic noise pattern of the readout system. The resulting Monte Carlo file was then readable by the normal Event-Display and tracking software for further studies, e.g. for the determination of the acceptance. The Monte Carlo simulated events were processed afterwards by the offline filter (see chapter 3) and the track reconstruction program (see chapter 4).

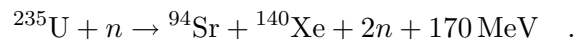
### 5.1.1 Event generation

The first part simulates antineutrinos from the core of a nuclear reactor. Furthermore, it generates the vertex position, the kinetic energy and scattering angle of the recoil electron. The geometry and size of the reactor core and of the TPC were taken into account as well. For every event the differential cross section for the  $\bar{\nu}_e e^-$  scattering was calculated. From this simulation, the expected event rate was obtained, without any acceptances.

#### 5.1.1.1 Antineutrinos from a nuclear reactor

Nuclear power reactors are abundant sources of antineutrinos, distributed up to 8 MeV, and peaking at 0.5 - 1.0 MeV. The antineutrino spectrum has two sources: the emission from fission fragments and the emission from radioactive nuclei formed in the capture of neutrons by various nuclei, including fission fragments. The second contribution was important at energies below 2 MeV.

Let us consider first the antineutrino emission from radioactive nuclei. If a  $^{235}\text{U}$  captures a neutron, the total energy is distributed over amongst the 236 nucleons now present in the compound nucleus. This nucleus is relatively unstable, and is likely to break into one heavy and one light fragment. Creation of the fission fragments is followed instantaneously by emission of typically 2-3 neutrons, which enable the chain reaction to be sustained. The origin of the asymmetric fragment yield, as shown in figure 5.2, can be predicted with the deformed-shell model proposed by Wilkins, Steinberg and Chasman [45]. The fission reaction in  $^{235}\text{U}$  produces hence nuclei such as Ba, Kr, Sr, Cs, I and Xe with atomic masses around 95 and 137. An example of a typical reaction is



Both the  $^{94}\text{Sr}$  and  $^{140}\text{Xe}$  isotopes subsequently decay and form more stable isotopes, with the emission of 6 electrons and antineutrinos.

An additional contribution at low energy (below 2 MeV) comes from nuclei formed in the capture of neutrons by various nuclei, including fission fragments. The resulting nucleus may become more stable by emitting  $\alpha$  or  $\beta$  particles. Since the  $^{238}\text{U}$  is the major proportion of the fuel element material in a thermal reactor (96%), capture of fast neutrons by  $^{238}\text{U}$  is an important process. The breeding of the (fissile)  $^{239}\text{Pu}$  from  $^{238}\text{U}$  is shown in the figure 5.3.

Some of the  $^{239}\text{Pu}$  isotopes may capture a neutron to become  $^{240}\text{Pu}$ , which is less stable. By further neutron capture,  $^{240}\text{Pu}$  nuclei may form  $^{241}\text{Pu}$ , which undergoes  $\beta$ -decay into  $^{241}\text{Am}$ . Moreover,  $^{239}\text{Pu}$  is fissile in the same way as  $^{235}\text{U}$ , i.e. with thermal neutrons. It is the other main source of energy (and antineutrinos) in a nuclear reactor.

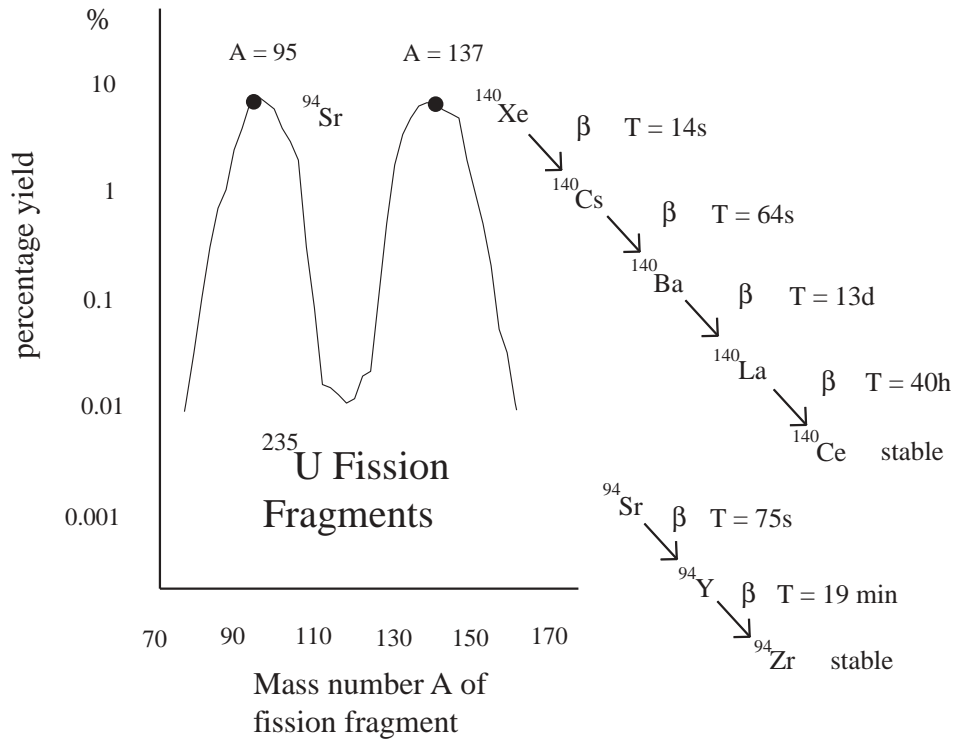


**Figure 5.2:** Distribution of fission products from  $^{235}\text{U}$ . Fission fragments with atomic mass number  $A$  close to 95 and 137 are preferred. The example shows the decay schemas of two fragments, with the emission of 6 electron antineutrinos. The mass distribution for thermal neutron-induced fission of  $^{235}\text{U}$  was taken from ref. [46].

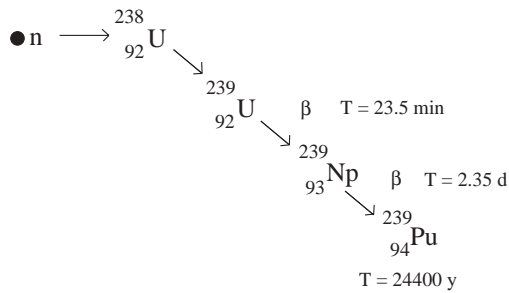


**Figure 5.3:** Neutron capture by  $^{238}\text{U}$  and the  $\beta$ -decays to the actinide  $^{239}\text{Pu}$ . The fissile  $^{239}\text{Pu}$  contributes to one third to the total antineutrino spectrum.

The Bugey (France) EDF nuclear reactor is a Pressurized Water Reactor (PWR) with a thermal power of 2750MW. The core is cylindrically shaped with 1.61 m radius and 3.66 m length. The Bugey reactor operates during almost a year, followed by a scheduled shut down of 1-2 month for the

replacement of a part of the fuel elements. After the refill, the antineutrino yield in per cent is as follows: 69% from  $^{235}\text{U}$ , 21% from  $^{239}\text{Pu}$ , 7% from  $^{238}\text{U}$  and 3% from  $^{241}\text{Pu}$ . Other fission fragments such as  $^{236}\text{U}$ ,  $^{240}\text{Pu}$ ,  $^{242}\text{Pu}$ , etc. contribute less than 0.1% to the antineutrino spectrum and can, therefore, be neglected.

During the operation period of a reactor, the Uranium isotopes are breeding the fissionable Plutonium isotopes as explained before, and consequently, the relative contribution of the fissioning isotopes varies as a function of time. This effect is called the burn-up of the fuel elements. Typically, the initial 69% contribution of the  $^{235}\text{U}$  isotope drops down to 50% after 7 month of reactor operation, whereas during the same period the contribution of the  $^{239}\text{Pu}$  isotope increases up to 36% due to breeding. The average contributions over a year from the fission fragments are 54% from  $^{235}\text{U}$ , 33% from  $^{239}\text{Pu}$ , 7% from  $^{238}\text{U}$  and 6% from  $^{241}\text{Pu}$ . The total effective energy per fission in a thermal reactor, including the contribution from neutron capture, was calculated in ref. [47] from fission product yields and from mass tables. The total effective energies per fission are displayed in table 5.1.

**Table 5.1:** Total effective energy per fission in a thermal reactor, including contributions from capture. The averaged contribution is shown in the last column.

Nuclide	Total energy (MeV/fission)	Averaged contribution
$^{235}\text{U}$	201.7	54%
$^{238}\text{U}$	205.0	6%
$^{239}\text{Pu}$	210.0	33%
$^{241}\text{Pu}$	212.4	7%

In a thermal reactor, the averaged total energy per fission is 205.3 MeV. In a thermal reactor of 2750 MW we expect therefore

$$N_{\text{fiss}} = \frac{2.75 \times 10^9 \text{ J/s}}{205 \text{ MeV} \times 1.602 \times 10^{-13} \text{ J/MeV}} \simeq 8.36 \cdot 10^{19} \quad (5.1)$$

fissions per second. This number gives the absolute normalisation, but not the shape of the antineutrino spectrum.

### 5.1.1.2 Antineutrino energy spectrum

For an interpretation of the data, we must have accurate knowledge of the antineutrino spectrum, including its low-energy part. The antineutrino spectrum emitted by fissioning isotopes was obtained experimentally and by calculation. For the three isotopes  $^{235}\text{U}$ ,  $^{239}\text{Pu}$  and  $^{238}\text{U}$ , the electron spectrum following fission was measured at the ILL reactor in Grenoble (ref. [48]-[51]). The antineutrino spectrum was then reconstructed from the electron spectrum with the fact, that for each  $\beta$ -decay the electron and the antineutrino

share the available endpoint energy. The available energy range for the antineutrino spectrum in these experiments was between 1.5 MeV and 10 MeV, and the 5% accuracy was mainly limited by the uncertainty in the electron spectrum and the reactor power. These measurements were in good agreement with the spectrum obtained at reactors with  $\bar{\nu}_e p \rightarrow e^+ n$  scattering by different collaborations ([52]-[56]). For the isotope  $^{239}\text{U}$  only calculations were available, see ref. [57].

Below 1.5-2.0 MeV the contribution from the  $\beta$ -decay of fission fragments can only be calculated by summing over all individual fragments, e.g. calculated in ref. [6] and [57] with an uncertainty of 10%. The contribution to the spectrum from neutron capture was calculated in ref. [57] for the decays of heavy isotopes formed during the reactor period, such as  $^{239}\text{U}$ ,  $^{239}\text{Pu}$  and  $^{237}\text{U}$ . A small correction due to neutron absorption by these fragments was also taken into account. Figure 5.4 shows the total electron antineutrino energy spectrum below 2 MeV, assuming a mean burn-up of the fuel composition. The plateau at 1 MeV is due to the fission of neutron-activated nuclei. The neutrino spectrum is shown in figure 1.5 up to 10 MeV.

### 5.1.1.3 Counting rate prediction

To obtain the expected event rate  $n(T)$  as a function of the electron energy  $T$ , one has to multiply the averaged differential cross section (see figure 1.6) as follows:

$$n(T) = \left\langle \frac{d\sigma}{dT} \right\rangle \times N_{\text{fiss}} \times \frac{1}{4\pi r^2} N_e \quad . \quad (5.2)$$

Here,  $N_{\text{fiss}}$  is the number of fissions per second (see section 5.1),  $r$  denotes the distance between the reactor and the TPC centre (18 m), and  $N_e$  is the number of electrons in the gas at a pressure of 3 bar, corresponding to  $3.25 \times 10^{27}$  electrons, see section 3.2.4. The expected electron energy spectrum for a pure weak-interaction and for an additional magnetic moment of  $10^{-10} \mu_B$  is shown in figure 5.5, where the counting rates were calculated per day and per 100 keV. Note that the differential cross section was given per MeV and per fission. From the integration of the counting rate in the interval 300 keV to 1.8 MeV one obtains 9.30 events per day for a weak-interaction, and 14.5 events per day for an additional magnetic moment of  $10^{-10} \mu_B$ . The spectrum in figure 5.5 was obtained from a Monte Carlo simulation, which takes the true distance between the position of the neutrino creation in the reactor core and position of the  $\bar{\nu}_e e^-$  vertex in the TPC into account. Moreover, the scattering angle  $\theta$  depends on the true neutrino direction, which was obtained from the positions mentioned above. Therefore, equation 5.2 was interpreted with the correct scattering angle and distance event by event.

These counting rates were the predictions without taking the detector response, the energy resolution and the acceptance of the track reconstruction into account. For that reason, the second and third part of the Monte Carlo simulation were developed.

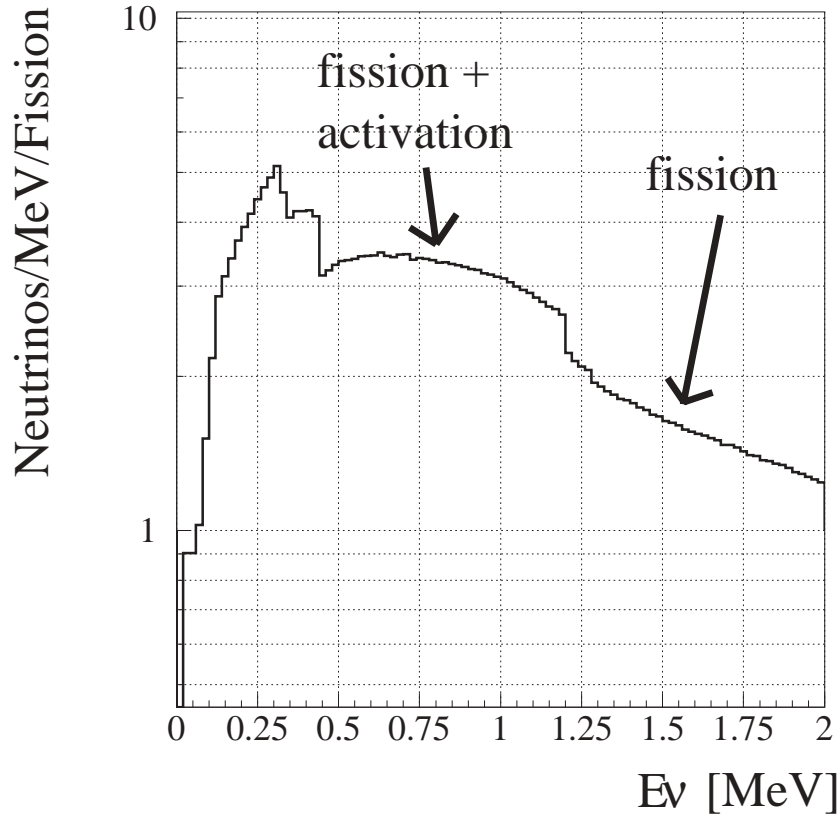


**Figure 5.4:** Simulated neutrino spectrum below 2 MeV.

### 5.1.2 Track simulation with GEANT

The second part of the Monte Carlo was based on GEANT to simulate the electron tracks. This part takes the start position, energy and direction of each event from the first part. In each detector component, the interaction probability was calculated based on the material properties. In case of an interaction, the energy deposition and scattering angle were calculated.

Let us shortly summarize the detector geometry used in the simulation. In the simulation, the detector was surrounded by a cube of air. Then the following cylindrical volumes were placed successively in the air cube: the anti-Compton steel vessel, the anti-Compton liquid scintillator, the TPC acrylic vessel, and the  $\text{CF}_4$  gas. The complete assembly is shown in figure 5.6. The photomultipliers were not important for the simulation, because the tracking was done with the TPC. The description takes the material densities and the gas pressure of the drift gas into account.

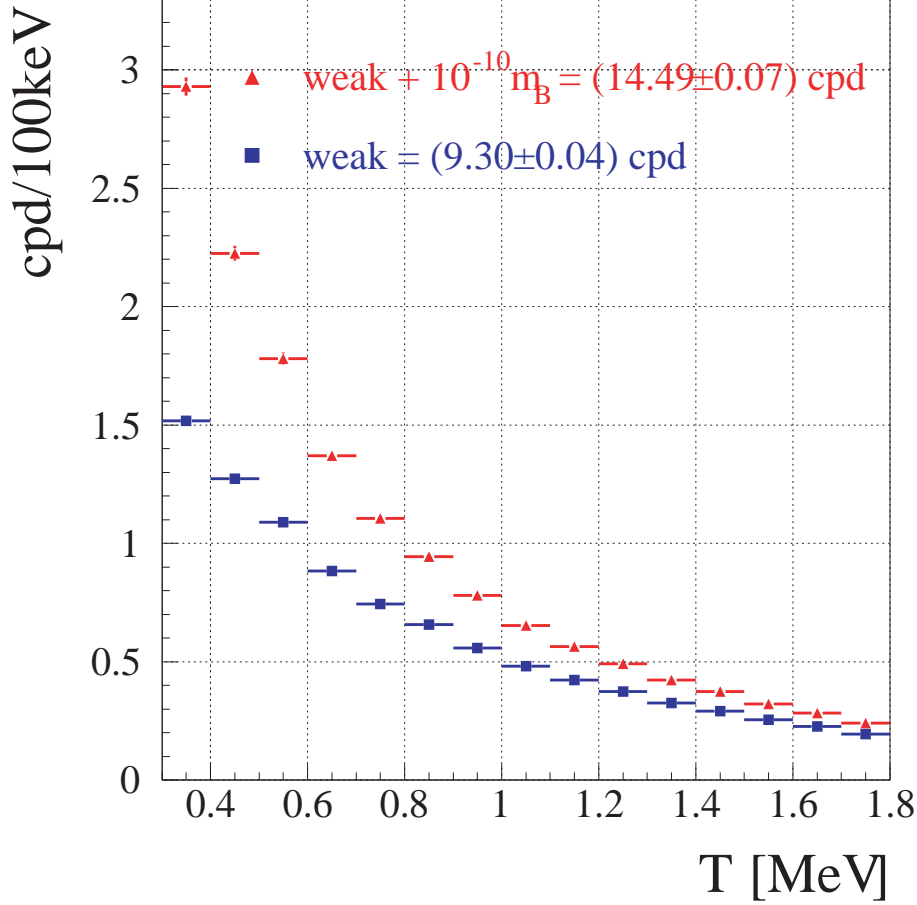


**Figure 5.5:** Expected energy distribution in counts per day (cpd) of the recoil electron in our TPC without acceptance corrections.

The physical interactions in our simulation were the photo effect, Compton scattering and pair production. The energy loss of electrons was by ionisation and bremsstrahlung. The energy resolution due to multiple scattering, statistical fluctuations and the attachment in the multiplication region, see section 2.1.1.3, were simulated at 3 bar with the following rule:

$$\sigma(E) = \sigma_0 \times \left( \frac{E}{E_0} \right)^n . \quad (5.3)$$

The resolution at the energy  $E_0 = 1 \text{ MeV}$  was found to be 8%, and the coefficient was 0.7 for the TPC, see ref. [19]. This empirical law was in better agreement with the low energy part of the Compton spectra. We believe that the resolution was not following a simple square root law, because the rather strong electron attachment in  $\text{CF}_4$  affects the statistics of the avalanche.

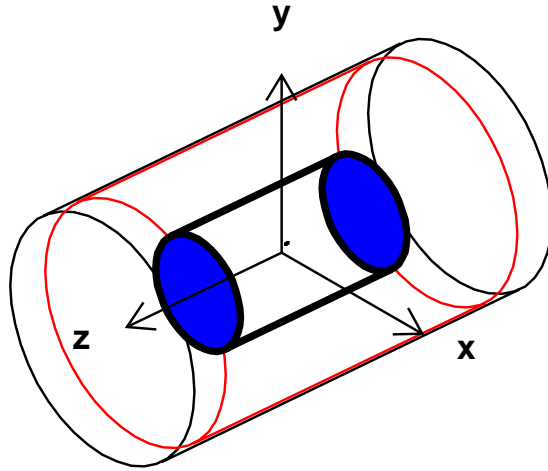


**Figure 5.6:** GEANT display of the simulated detector components: steel vessel (black), liquid scintillator (red), TPC acrylic (blue) and  $\text{CF}_4$  drift gas (innermost volume).

### 5.1.3 Track digitisation

The simulated tracks from the second part have to be written in the format of the real data, so that the offline filter and tracking program can be tested directly. The main problem in the digitisation was the electronic noise which has to be simulated accurately. Simulated events without electronic noise were reconstructed more efficiently compared to real data, leading to a better, but wrong, angular resolution.

The following successful solution was found: A pedestal run containing only electronic noise was recorded. The run was then scanned by eye to remove accidental electrons in the data. The remaining background data was then saved in a special noise file. The noise pattern was added to the electron trajectory from GEANT during the digitisation process. Verification of the resulting digitisation was done by eye scanning of these events: No significant difference between real data and generated events was visible anymore. An alternative approach would have been to superimpose the amplifier response function. But the typical electronic noise pattern was difficult to simulate, especially the clustering of noise within 3-5 strips. This small electronic noise clusters leads to potential fake ends in the tracking.

## 5.2 Acceptance of the automatic tracking

As shown in figure 5.1, the Monte Carlo events have been processed successively by the offline filter and the tracking in order to determine the acceptances. The following data reduction was obtained (see figure 5.7):

The first reduction was due to the offline filter, which was determined in section 3.1.6 to be 80%. The main reduction comes from the containment. The next reduction was due to the track reconstruction. The reconstructed

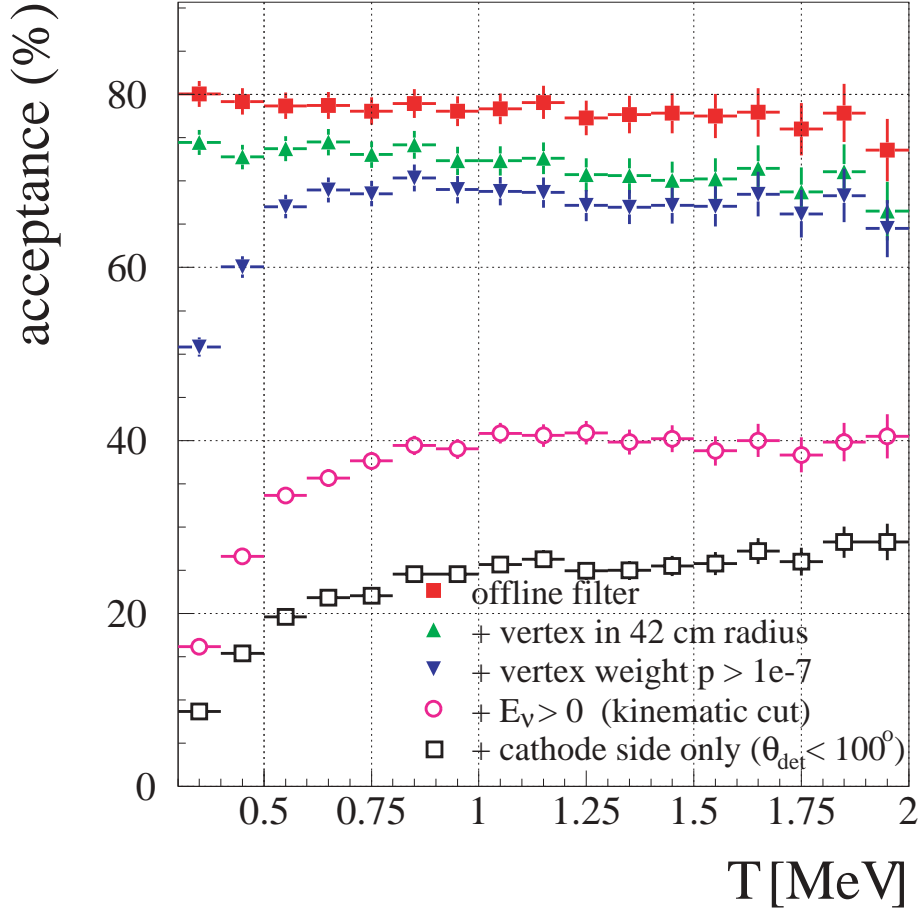


**Figure 5.7:** Acceptance of the different steps in the data processing. Data and Monte Carlo events were passed through the same filter and reconstruction program. See text.

vertex position was used to classify the events as inside or outside the containment. This reduced the data to 75%. The next reduction was due to the vertex weight  $p$ , which was used to select only well reconstructed events. In the present analysis, the cut on the vertex weight was set to a rather low threshold ( $10^{-7}$ ). The remaining percentage of the original data set was then 70%, and independent on the energy above 500 keV. At low energy, the acceptance decreases significantly (50%) due to multiple scattering, see figure 4.14.

The next reduction was due to the kinematic cut. The scattering angle was measured from the first 4 cm of the electron track. The neutrino energy  $E_\nu$  can then be reconstructed from the electron energy  $T$  and from the scattering

angle by

$$E_\nu = \frac{m_e}{\sqrt{\frac{T+2m_e}{T} \cos \theta - 1}} \quad , \quad (5.4)$$

where  $m_e$  denotes the electron mass (0.511 MeV). The neutrino energy has always to be positive, which can only be fulfilled if the scattering angle was not larger than

$$\cos \theta \leq \sqrt{\frac{T}{T + 2m_e}} \quad . \quad (5.5)$$

At low energy  $T$ , e.g. at 300 keV, the opening angle of the forward cone is  $61.6^\circ$ , whereas at higher energies the scattering angle becomes more forward peaked: At 700 keV the opening angle of the forward cone is  $50.4^\circ$ , at 1 MeV  $45.3^\circ$  and at 2 MeV  $35.6^\circ$  respectively. The relation between the scattering angle and the recoil energy  $T$  of the electron was used to select the events within the forward and backward cones. The acceptance after this step was around 40% above 700 keV, 30% at 500 keV and 20% at 300 keV.

In the analysis, different thresholds on the vertex weight were tested to improve the acceptance after the kinematic cut. The acceptance did not change significantly due to the following reason: with a higher threshold on the vertex weight  $p$ , only well-reconstructed events were accepted. This was reducing the acceptance obviously more than with a low threshold cut. On the other hand, the well-reconstructed events have a better angular resolution, and consequently the reduction by the kinematic cut was less. This compensates the reduction due to the vertex cut applied before. Above 700 keV, the vertex reconstruction, angular fit and kinematic cut decreases the acceptance from 80% (filter) to 40%, as shown in figure 5.7. Hence, the acceptance of the automatic tracking was around 50%. This was rather poor compared to the 90% acceptance of the visual scanning, as shown in B.9. The last reduction was due to the cut  $\theta_{\text{det}} < 100^\circ$ , which accepts only events from the cathode side.

The global acceptance of the filter and tracking process was 25% above 700 keV, decreasing to 20% at 500 keV and 10% at 300 keV. The decrease of the acceptance at low energy explains why the upper limit on the magnetic moment cannot be improved by lowering the energy threshold on the energy  $T$ . The resulting energy spectrum is shown in the chapter 6, where the comparison between the measured counting rate and the Monte Carlo prediction was used to determine the upper limit on the neutrino magnetic moment. The Monte Carlo error comes from uncertainties in the antineutrino flux and spectrum (5%), track reconstruction (2%), offline filter (3%) and target electron density (1%).

The expected counting rate in the interval 300 keV- 1.8 MeV for the weak interaction was found to be 1.62 counts per day, and 2.66 counts per day for an additional magnetic moment of  $10^{-10} \mu_B$  respectively, see table 5.2. The (averaged) global acceptance for this interval is therefore 18% for the weak and for the electromagnetic interaction.

**Table 5.2:** Expected counting rates.

Stage	weak [counts/day]	$+10^{-10}\mu_B$ [counts/day]
Generated [300 keV,1.8 MeV ]	9.30	14.50
With global acceptance (18%)	1.62	2.66

The Monte Carlo simulation contains many other important features. For instance, the position of the vertex was taken into account as well: An electron close to the acrylic wall at the reactor opposite side, but with its vertex still inside the containment, will most probable leave the TPC. Electrons close to the reactor side instead have a much larger region in the forward direction to their disposition, see figure 5.8 (right). Therefore, the global acceptance (see figure 5.7) depends on the angle  $\phi$ , which was defined relative to the  $y$ -direction. This effect is illustrated in figure 5.8 (left), which shows the global acceptance versus the angle  $\phi$ .

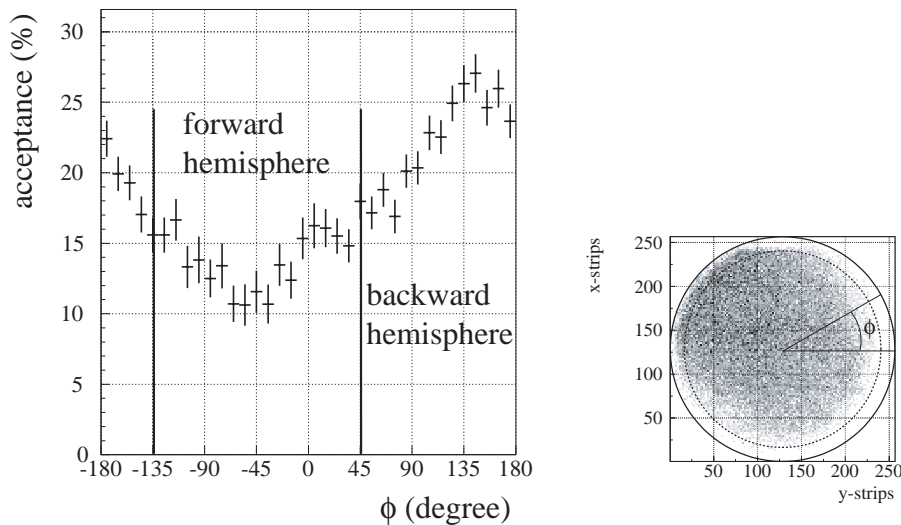


**Figure 5.8:** Global acceptance as a function of  $\phi$  (left), and true vertex distribution of the accepted events (right). The solid circle corresponds to the TPC wall, and the dashed circle illustrates the 42 cm containment. The reactor is located in the top left corner. (Monte Carlo simulation)

Due to the random vertex distribution, the distance between the reactor and the vertex changes with every event. The antineutrino flux is 10% higher at the walls close to the reactor compared to the opposite side. Therefore, the true distance and direction were taken into account in the determination of the normalisation. This simulation includes also the reactor size and geom-

---

etry, leading to a worse angular resolution  $\sigma_\theta$  in order of  $3^\circ$ .

### 5.3 Discussion

For the study of the acceptance, the online and offline filter, the containment, the detector response simulated with GEANT, the vertex reconstruction and the kinematic cut were taken into account. The global acceptance has been determined with high statistic for a weak interaction alone and for different magnetic moments. Unfortunately, the acceptance of the automatic tracking was smaller compared to the visual scanning.

A measurement at low energy would be more sensitive to the upper limit on the neutrino magnetic moment. However, the acceptance of the automatic tracking was around 25% above 700 keV, but decreases rapidly at lower energies. Due to the bad acceptance and the high background at low energy, the upper limit was not improved by lowering the electron energy threshold. Nevertheless, the automatic tracking can be applied on the full data set.



*Data Analysis*

In this chapter, the analysis of the 66.3 days reactor ON data is presented. First, obviously bad events are removed from the raw data by the offline filter, as explained in chapter 3. All remaining electrons are then reconstructed with the automatic tracking, as explained in chapter 4. The obtained energy spectrum is then compared with the Monte Carlo prediction for a weak and electromagnetic interaction. From that an upper limit on the neutrino magnetic moment is derived. Moreover, the cross sections for the  $\bar{\nu}_e e^-$  scattering is determined and compared to the predicted values from weak and electromagnetic interaction. The results obtained with the automatic tracking are in good agreement with the weak interaction.

## *6.1 Event selection*

A short summary of the event selection by the hardware trigger, offline filtering and track reconstruction shall be given here. More details can be found in previous chapters, see 2, 3 and 4.

### *6.1.1 Hardware trigger and online filtering*

The counting rate of the anode signal with an energy deposit above 250 keV is 90 Hz. Most of these events are cosmic muons because the detector is not underground. The 200  $\mu$ s muon veto is used to reject cosmic muons and any successive  $\gamma$ -ray emission due to neutron activation. The counting rate after the muon veto is 1 Hz. After applying the anti-Compton veto against Compton electrons during 80  $\mu$ s, the counting rate decreases to 0.5 Hz. The online filter against electrical discharges reduces the counting rate to 0.23 Hz. The data is finally written to disc with 0.14 Hz. The acceptance of the online

filter is 99.5%, and the 40% dead time is used to calculate the effective live time ( = 66.3 effective days out of 109 days with reactor ON) of the experiment. The various trigger levels and corresponding counting rates are summarised in table 6.1.

**Table 6.1:** Hardware trigger counting rates.

Hardware trigger and DAQ	rate [ Hz ]
Anode ( 250 keV threshold )	90
+ Veto Muon (22 MeV threshold, 200 $\mu$ s veto)	0.86
+ Veto AntiCompton (80 $\mu$ s veto, 100 keV threshold, mult. 8)	0.51
+ online filter (electrical discharges, asymmetry below 0.3)	0.24
+ DAQ readout and writing on disc, dead time 40%	0.144

### 6.1.2 Offline filtering

The real data are filtered afterwards to eliminate obviously bad events, namely:

- Electrons due to Compton scattering, which are identified by a  $\gamma$ -ray above 100 keV in the 80  $\mu$ s preceding their avalanche.
- Electrical discharges. They have an asymmetry in the scintillation light between the anode and cathode side of more than 0.3, and the signal length is shorter than 8 z-bins (1.3 cm).
- Electrons not fully inside the containment of the 42 cm fiducial volume.
- Electrons crossing the anode plane. This type of event can be rejected by the fast rise time of the photomultiplier signal.
- Events saturating the anode signal. This cut ensures that the energy of an event can be determined correctly.
- Events below 100 keV.

After applying the offline filter, the counting rate is 36 mHz for a 300 keV energy threshold and 5.1 mHz for 700 keV respectively. More details can be found in chapter 3. These counting rates are still much higher than the expected signal from the  $\bar{\nu}_e e^-$  scattering. The prediction for the weak interaction is 1.62 events per day, see chapter 5.

### 6.1.3 Track reconstruction and kinematic cut

All remaining events above 300 keV are processed by the tracking program. The program reconstructs the trajectories in both projections and finds the vertex, as explained in chapter 4. The vertex weight  $p > 10^{-7}$  is used to select only well reconstructed tracks. Additionally, the vertex position is used to classify the event as inside or outside the containment, eliminating about 10% of the electrons in total. The most important information coming from the event reconstruction is the scattering angle, which is obtained from the first 4 cm of the track by a fit in 3D. An excess of events from the anode side is observed, which is probably due to the higher complexity of the readout plane. To reduce the background from the anode side, only events coming from the cathode side are accepted ( $\theta_{\text{det}} < 100^\circ$ ).

Moreover, only events within the forward kinematical cone are accepted, using the formula:

$$E_\nu = \frac{m_e}{\cos \theta \sqrt{1 + \frac{2m_e}{T} - 1}} > T \quad . \quad (6.1)$$

For the backward cone, the scattering angle is assumed to be  $\pi - \theta$ . The event selection due to the track-reconstruction is summarised in table 6.2.

**Table 6.2:** *Track reconstruction*

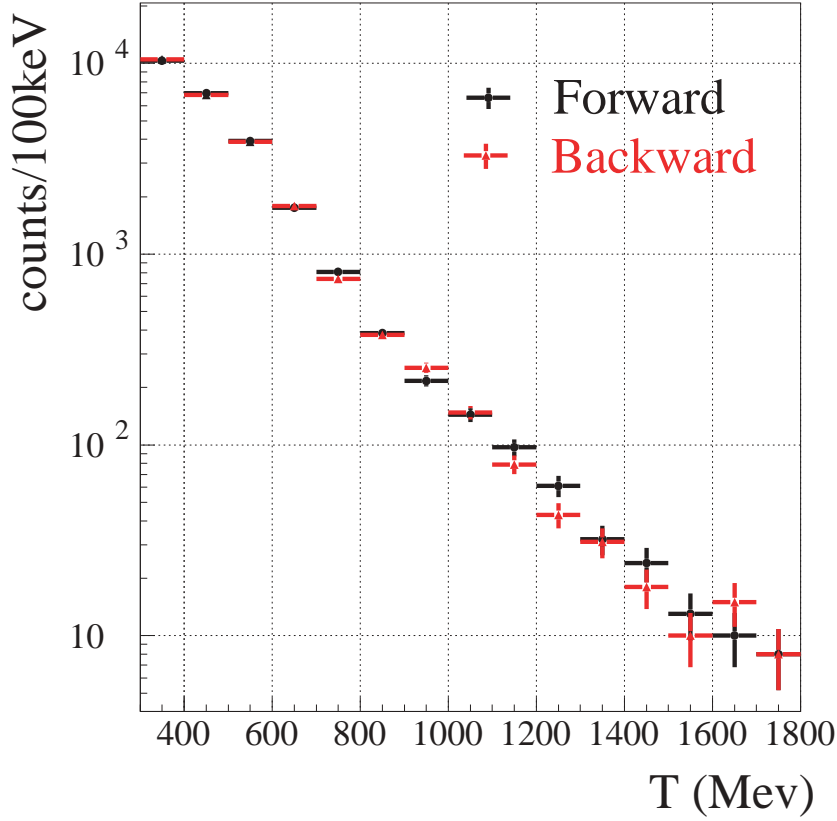
Cut	Threshold 300 keV counts/day	Threshold 700 keV counts/day
Accepted events from offline filter	3100	440
+ Containment + Vertex weight	2760	400
+ Anode side	1600	150
+ Forward cone	374	27

Figure 6.1 shows the measured electron energy spectrum of the forward and backward cone for the 66.3 days reactor ON data. Events originating from the anode side are rejected as well with  $\theta_{\text{det}} < 100^\circ$ . The electron energy spectrum of the backward cone is similar to the forward cone.

The strength of the MUNU-Experiment is the identification of muons, Compton electrons,  $\alpha$ 's, electrical discharges and not contained electrons by their topology and or by the anti-Compton veto. Moreover, the kinematic selection of electrons by the scattering angle reduces the background significantly.

## 6.2 Isotropy of the background: Reactor OFF

Background is measured during 19.3 days reactor OFF. This data is used to verify the isotropy of the background. Figure 6.2 shows the forward minus



**Figure 6.1:** Recoil energy spectrum for the forward (black circles) and backward (red triangles) direction cone for events coming from the cathode side ( $\theta_{\text{det}} < 100^\circ$ ).

backward distribution of the electron energy. The recoil energy spectrum of contained electrons shows no precise structure.

Table 6.3 summarises the forward minus backward subtraction for the reactor OFF period at three particular thresholds. At 550 keV a forward minus backward asymmetry is observed. Above 600 keV, the asymmetry is still negative, but less significant. The statistic of the reactor OFF data is small however, and cannot be used to identify a particular position of a - possible - radioactive contamination. Moreover, the analysis of Compton events did not reveal any hot spots. The following effects for the forward minus backward asymmetry are excluded, namely:

- The inverse  $\beta$ -decay reaction  $\bar{\nu}_e + p \rightarrow e^+ + n$  in the TPC gas. This type of event is not present because the  $\text{CF}_4$  has no free protons. Moreover, the  $\gamma$ -emission due to positron annihilation would be vetoed by the anti-Compton.

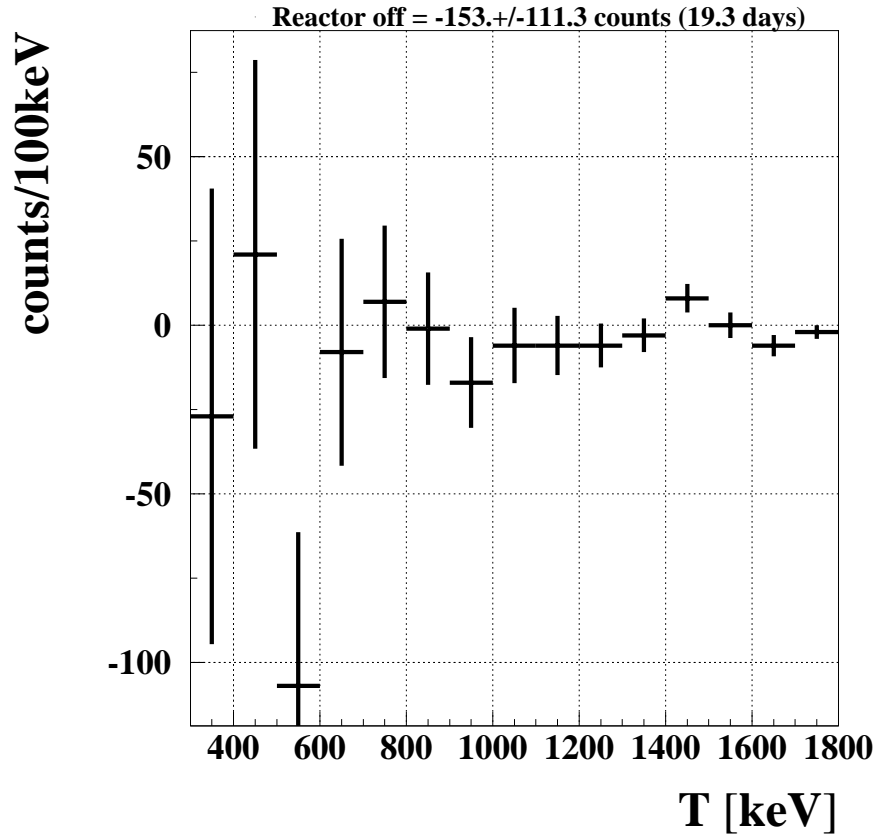


**Figure 6.2:** Forward - backward counts with reactor OFF data as a function of electron recoil energy.

- The inverse  $\beta$ -decay reaction  $\bar{\nu}_e + p \rightarrow e^+ + n$  in the acyclic TPC. This type of event exists, but it is eliminated by the containment filter.
- The energy calibration, z-binning conversion, veto-counting rate, and live time. Every systematic error cancels out in the forward minus backward comparison.
- The offline filter. No forward minus backward asymmetry can be created by construction: The containment filter is defined by the fiducial volume, hence is independent on the direction of the event in case of an isotropic distribution. The filter against electrons crossing the anode plane is the same for events in the forward and backward cone.
- The tracking program. A study with isotropic generated background showed no significant difference between the forward and backward cone.

**Table 6.3:** *Reactor OFF. Total number of events in 19.3 days.*

Threshold $T$ (keV)	forward - backward
300	$-153 \pm 111$
700	$-32 \pm 36$
1000	$-21 \pm 17.8$

The background data of the reactor OFF period is not used as a correction of the reactor ON data in the following analysis, because the observed asymmetry is a statistical fluctuation.

### 6.3 Analysis of reactor ON data

#### 6.3.1 Forward minus backward comparison

The advantage of the MUNU experiment is the simultaneous measurement of the signal and background. In the forward cone ( $\cos\theta \simeq 1$ ), signal and background events are observed. In the backward cone ( $\cos\theta \simeq -1$ ) are only background events. The forward minus backward cone subtraction then defines the signal from the reactor. The number of events above an electron energy threshold for the 66.3 days reactor ON are summarised in table 6.4, together with Monte Carlo predictions.

**Table 6.4:** *Reactor ON. Total number of events in 66.3 days.*

Threshold $T$ (keV)	forward	backward	f-b	weak	weak + e.m.
300	$24792 \pm 158$	$24704 \pm 157$	$88 \pm 223$	106	176
700	$1797 \pm 42$	$1726 \pm 42$	$71 \pm 59$	52	79
1000	$389 \pm 20$	$352 \pm 19$	$37 \pm 27$	24	34

For a 300 keV threshold, we have 24792 events in the forward cone, whereas the forward minus backward subtraction gives  $88 \pm 223$  events. From the weak interaction we expect 106 events, and with an additional magnetic moment ( $10^{-10} \mu_B$ ) 176 events respectively. To calculate the counts per day, one has to divide the number of events by the effective live time of the experiment, which is 66.32 days exactly. From this, we have 374 events per day in the forward cone, and the forward minus backward subtraction gives  $1.33 \pm 3.5$  events per day. Predicted are 1.6 events from the weak interaction and 2.65 events with an additional magnetic moment respectively. The signal to background ratio at 300 keV corresponds to  $176/24704 = 7/1000$ , which is rather bad. For that reason, the high background at low energy is one of the limiting factors for the analysis.

At 700 keV the number of total events drops to 1797 events (27 per day) in the forward cone, whereas the forward minus backward subtraction gives  $71 \pm 59$  events. From the weak interaction we expect 52 events, and with an additional magnetic moment 79 events respectively. The signal to background ratio at 700 keV corresponds to  $79/1726 = 5/100$ , one order better than at 300 keV. Similarly, one obtains a good signal to background ratio of 1:10 at 1000 keV.

The reactor OFF data measurement verified the forward minus backward isotropy of the energy spectrum, and therefore, the observed signal during reactor ON is due to the antineutrino flux from the reactor core.

### 6.3.2 Upper limit on the neutrino magnetic moment

The subsequent analysis works as follows: For all energy-cuts, scanning from 300 keV up to 900 keV, the experimental reactor ON data is compared to the Monte Carlo simulation. In figure 6.3, the forward minus backward energy spectrum for an 300 keV threshold is shown together with the weak prediction and the prediction for an additional magnetic moment of  $1.7 \cdot 10^{-10} \mu_B$ .

For the comparison with the Monte Carlo prediction, the energy spectrum of the recoil electron is taken in the interval from e.g. 300 keV to 1800 keV. The binning width is set to 100 keV. For each energy channel, the difference between the measured number of events per day  $y_i$  and the Monte Carlo prediction  $MC_i$  is squared, and divided by the experimental and Monte Carlo simulation error squared. The  $\chi^2$  is defined as the sum over channels:

$$\chi^2 = \sum \frac{(y_i - MC_i)^2}{\sigma_i^2}, \quad \sigma_i^2 = \sigma_{y_i}^2 + \sigma_{MC_i}^2 \quad . \quad (6.2)$$

In the  $\chi^2$  analysis, the recoil energy spectrum is fitted. The shape contains the information of the differential cross section. The Monte Carlo counting rate  $MC_i$  is given by the sum of the weak prediction  $W_i$  and the electromagnetic contribution  $E_i$  from an additional neutrino magnetic moment:

$$MC_i = W_i + \mu_\nu^2 E_i \quad (6.3)$$

The predicted counting rate varies as a function of the squared magnetic moment  $\mu_\nu^2$ , and the term  $E_i$  corresponds to the contribution from the magnetic moment equal to  $10^{-10} \mu_B$ .

Minimising the  $\chi^2$  for the parameter  $\mu_\nu^2$  is done for every energy threshold from 300 keV to 900 keV. The parabola in figure 6.4 is the  $\chi^2$  as a function of the squared neutrino magnetic moment for a 300 keV threshold. From the  $\chi^2$  parabola, its minimal position and width can be determined. The minimal position in  $10^{-20} \mu_B^2$  units is 0.02, and the width is 1.75.

Table summarises the position of the minimum and  $1\sigma$  width of the  $\chi^2$  parabola for particular energy thresholds. From the position and the width,

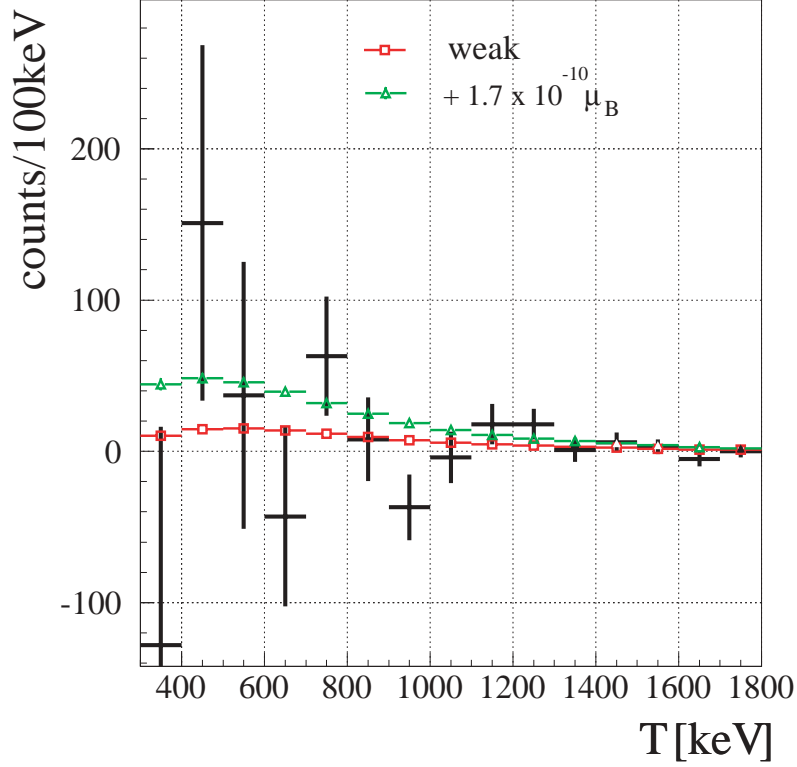


**Figure 6.3:** Reactor ON spectra and Monte Carlo.

one obtains the upper limit at 90% confidence level (last column) in units of  $10^{-10} \mu_B$ .

**Table 6.5:** Result of the  $\chi^2$  minimisation.

Threshold $T$	$\mu_\nu^2$	$1\sigma$	$\mu_\nu$ 90% CL
keV	$10^{-20} \mu_B^2$	$10^{-20} \mu_B^2$	$10^{-10} \mu_B$
300	0.02	1.75	1.71
400	0.27	1.77	1.78
500	-0.09	1.79	1.69
600	-0.20	1.84	1.69
700	0.30	1.90	1.85
800	-0.61	2.02	1.65
900	-0.67	2.19	1.72

In the energy interval 1000-1200 keV, the measured spectrum is higher than the prediction from weak interaction alone. The difference is not significant,

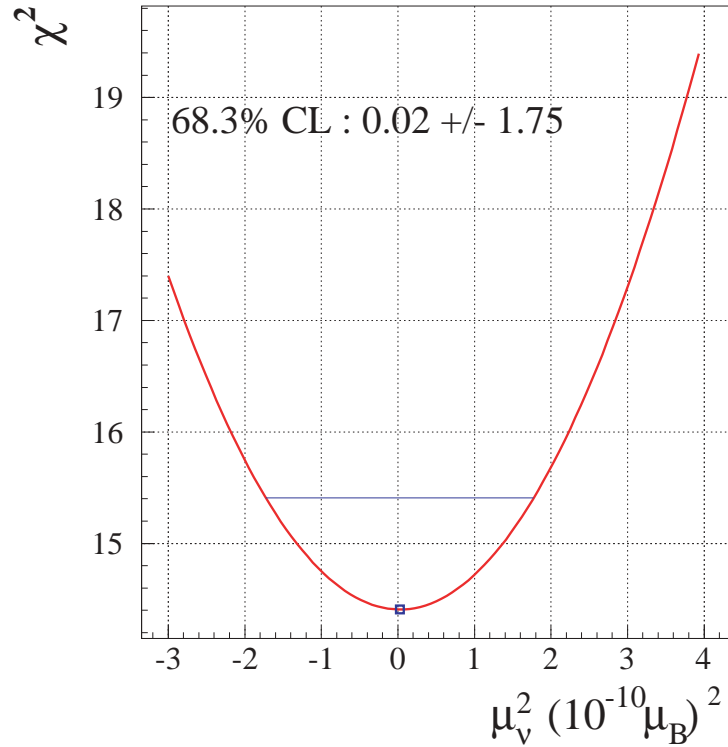


**Figure 6.4:**  $\chi^2$  parabola for the 300 keV recoil energy spectrum.

however. At 950 keV, the measured signal is  $2\sigma$  lower than the weak prediction. This fluctuation is statistically possible, however. Note that the signal is defined as the difference between the forward minus the backward cone, and this difference can be negative. As a consequence, the position of the  $\chi^2$  parabola, associated to the energy spectrum with a threshold at 900 keV, is negative ( $-0.67 \cdot 10^{-20} \mu_B^2$ ). The upper limit for the 900 keV threshold is not better, however. In the 850 keV channel, the forward minus backward signal is positive and compatible with the weak interaction. The peak at 750 keV corrects the negative signal at 900 keV, and hence the position of the  $\chi^2$  parabola is back at positive values ( $0.3 \cdot 10^{-20} \mu_B^2$ ). The 750 keV channel is reproduced by the visual scanning. At lower energies, the error bars become large due to the increasing background.

For the upper limit on the neutrino magnetic moment, not only the position of the parabola is important, but also its width. The width of the parabola changes with the error of the measurement: Increasing the statistic decreases the error bars, and therefore decreases the width of the  $\chi^2$  parabola. Because the error bars are given by the Poisson statistics, the sensitivity of our measurement scales with the square root of time. At lower energies, the error bars increase due to the strong background.

From the position and the width of the  $\chi^2$  parabola, the upper limit on the

neutrino magnetic moment is obtained with the unified approach of Feldman and Cousins [59]. Figure 6.5 summarises the confidence limits for Gaussian measurements  $x$  close to a non-physical boundary, where the true value  $\mu$  cannot be negative.

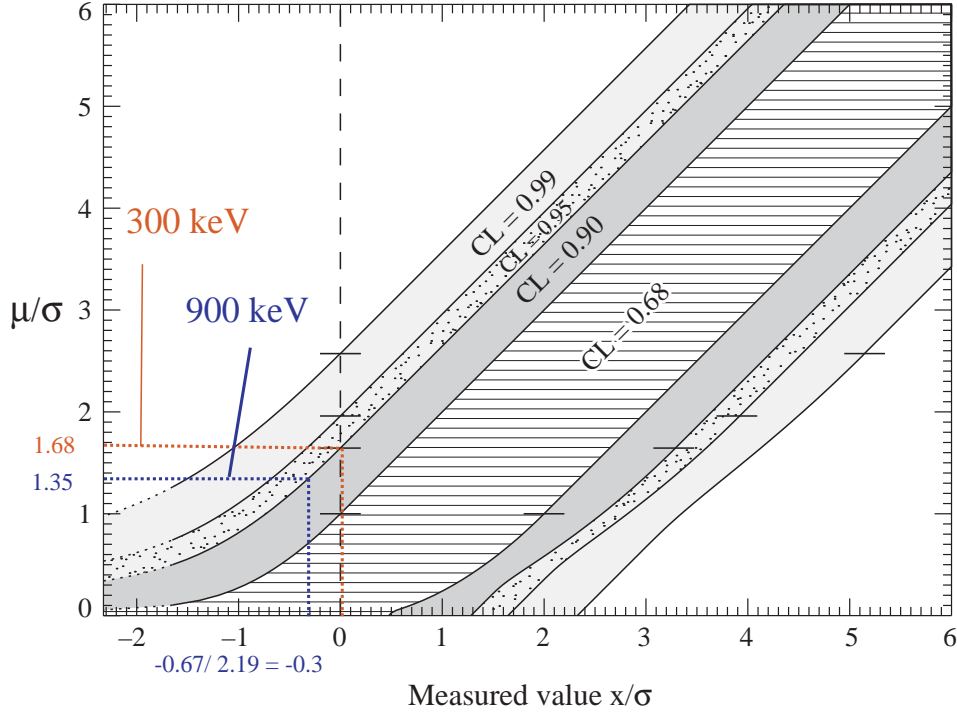


**Figure 6.5:** Upper limits for the  $\bar{\nu}_e e^-$  magnetic moment.

For a 300 keV threshold, the measured position of the parabola in standard deviations  $x$  is

$$\frac{0.02}{1.75} = 0.01 \quad . \quad (6.4)$$

Then, the physical value  $\mu$  in standard deviations is obtained at the 90% confidence limit, which is 1.68. Multiplication with the standard deviation ( $\sigma = 1.75$ ) gives 2.94, and the square root of this value is the upper limit in  $10^{-10} \mu_B$  units:

$$\sqrt{1.68 \cdot 1.75} = \sqrt{2.94} = 1.71 \quad . \quad (6.5)$$

For a 900 keV threshold, the measured position of  $\mu_\nu^2$  is negative (-0.67), corresponding to  $x = -0.67/2.19 = -0.3$  in standard deviations. This is non-physical. The unified method gives for this measurement outside the physical region a positive confidence limit in  $10^{-10} \mu_B$  units:

$$\sqrt{1.35 \cdot 2.19} = \sqrt{2.95} = 1.72 \quad . \quad (6.6)$$

The upper limits are summarised in the table 6.5, and are plotted versus the threshold of the electron energy  $T$  in figure 6.6. A 90% confidence level upper limit of

$$\mu_\nu < 1.7 \times 10^{-10} \mu_B$$

is obtained, which is independent of the chosen energy threshold. There is no evidence for a finite neutrino magnetic moment. The result is in good agreement with the expected value from weak interaction.

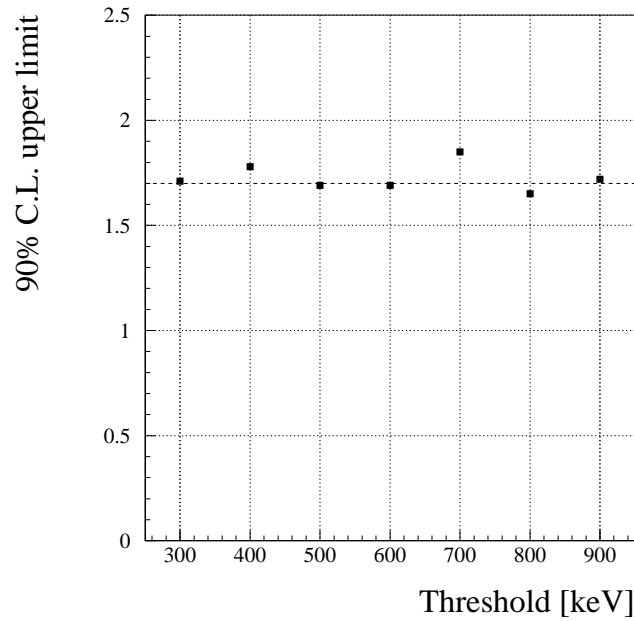


**Figure 6.6:** Upper limit on the magnetic moment as a function of energy threshold.

### 6.3.3 Total cross section measurement

The total cross section can be calculated with formula 1.15 given in section 1.1, which is obtained for the particular interval 300-1800 keV. With the measured magnetic moment squared from table 6.5 at the 300 keV threshold, the total cross section in this interval is, with a rather larger uncertainty

$$\sigma = (1.66 \pm 1.66) \cdot 10^{-20} \text{b/fission} \quad .$$

The predicted cross section for the weak interaction is  $1.65 \cdot 10^{-20}$  b/fission. Similarly, the cross sections for the other electron energy thresholds can be calculated, see table 6.6. The cross section of the electromagnetic interaction in this table is for a magnetic moment of  $10^{-10} \mu_B$ . The measurement of the cross section is compatible with the weak prediction, with admittedly large errors.

**Table 6.6:** Total cross sections, measured and predicted.

Threshold $T$ keV	$\sigma$ measured $10^{-20}$ b/fission	weak $\sigma$ $10^{-20}$ b/fission	e.m. (only) $\sigma$ $10^{-20}$ b/fission
300	$1.66 \pm 1.66$	1.64	0.95
400	$1.56 \pm 1.22$	1.37	0.69
500	$1.10 \pm 0.93$	1.14	0.52
600	$0.87 \pm 0.72$	0.95	0.39
700	$0.89 \pm 0.58$	0.80	0.31
800	$0.52 \pm 0.48$	0.67	0.24
900	$0.42 \pm 0.40$	0.55	0.18

## 6.4 Conclusions

The forward minus backward spectrum of the 19.3 days reactor OFF data is found to be symmetric for all energies, except for a statistical fluctuation at 550 keV. Table 6.7 summarises the forward minus backward subtraction at three particular energy thresholds.

**Table 6.7:** Reactor OFF. Total number of events in 19.3 days.

Threshold $T$ (keV)	forward - backward
300	$-153 \pm 111$
700	$-32 \pm 36$
1000	$-21 \pm 17.8$

The method of the automatic track reconstruction is applied to the total reactor ON data with a detection threshold at 300 keV. In the eye scanning, only events above 700 keV are analysed. The spectra obtained from the two methods are in good agreement above 700 keV, and the high bin at 750 keV is reproduced. This verifies the spectrum of the automatic tracking. The event selection at 700 keV energy threshold for 66.3 days reactor ON is summarised in table 6.8.

The signal to background ratio is  $7 \times 10^{-3}$  at 300 keV,  $5 \times 10^{-2}$  at 700 keV and  $10^{-1}$  at 1 MeV. The accuracy of the measurement at low energy is therefore limited by background. Consequently, the upper limit on the neutrino magnetic moment could not be improved at lower electron energy thresholds.

The upper limits at 90% confidence level on the neutrino magnetic moment are summarised in table 6.9 for various recoil electron energy thresholds. An upper limit on the neutrino magnetic moment of

$$\mu_\nu < 1.7 \cdot 10^{-10} \mu_B \quad (6.7)$$

**Table 6.8:** Event selection summary at 700 keV energy threshold for reactor ON.

Cut	Threshold 700 keV counts/day
Recorded events	4700
Electrical discharges	2850
Anode crossing	950
e- $\gamma$	740
Containment	490
Other (saturation, trigger time)	440
= Accepted events from offline filter	440
+ Vertex containment + weight p	400
+ Anode side	150
+ Forward cone	27
Forward - backward	$1.33 \pm 3.5$
Weak interaction prediction	1.6
Weak + e.m interaction prediction	2.65

at 90% confidence level is obtained. The result is in good agreement with the weak interaction, and there is no indication for a finite magnetic moment.

The total cross sections is measured and compared to the expected values from weak and electromagnetic interaction. The obtained cross sections are in good agreement with the weak interaction, see table 6.9.

**Table 6.9:** Upper limits and total cross sections.

Threshold $T$ keV	$\mu_\nu$ 90% CL $10^{-10} \mu_B$	$\sigma$ measured $10^{-20}$ b/fission	weak $\sigma$ $10^{-20}$ b/fission	e.m. (only) $\sigma$ $10^{-20}$ b/fission
300	1.71	$1.66 \pm 1.66$	1.64	0.95
400	1.78	$1.56 \pm 1.22$	1.37	0.69
500	1.69	$1.10 \pm 0.93$	1.14	0.52
600	1.69	$0.87 \pm 0.72$	0.95	0.39
700	1.85	$0.89 \pm 0.58$	0.80	0.31
800	1.65	$0.52 \pm 0.48$	0.67	0.24
900	1.72	$0.42 \pm 0.40$	0.55	0.18

The results from the visual scanning, see ref. [17] [60], are more stringent than then limits obtained by the automatic tracking. The recoil electron spectrum above 900 keV is in good agreement with the expectation assuming weak interaction alone. For a threshold at 900 keV the following limit on the neutrino magnetic moment is derived:  $\mu_\nu < 1.0 \cdot 10^{-10} \mu_B$  at 90% confidence level. At 750 keV, an excess in the forward minus backward dif-

ference compared to the weak interaction prediction is observed. A further rise at lower energies can be excluded with the spectrum obtained by the automatic tracking, however. The upper limit at a 700 keV threshold gives the limit  $\mu_\nu < 1.4 \cdot 10^{-10} \mu_B$  at 90% confidence level, still more stringent than the limit from the automatic tracking.

## APPENDIX A: Counting rates

### A.1 Anti Compton

The anti-Compton counting rates were measured during the reactor ON and OFF periods. The vertical line in the plots is marking the time of the reactor shutdown, at day 823. The anti-Compton AC is 710 Hz, and the muon veto 260 Hz. In addition to the muon veto counting, the muon trigger built from the TPC anode signal is shown. The counting rate was between 90-100 Hz.

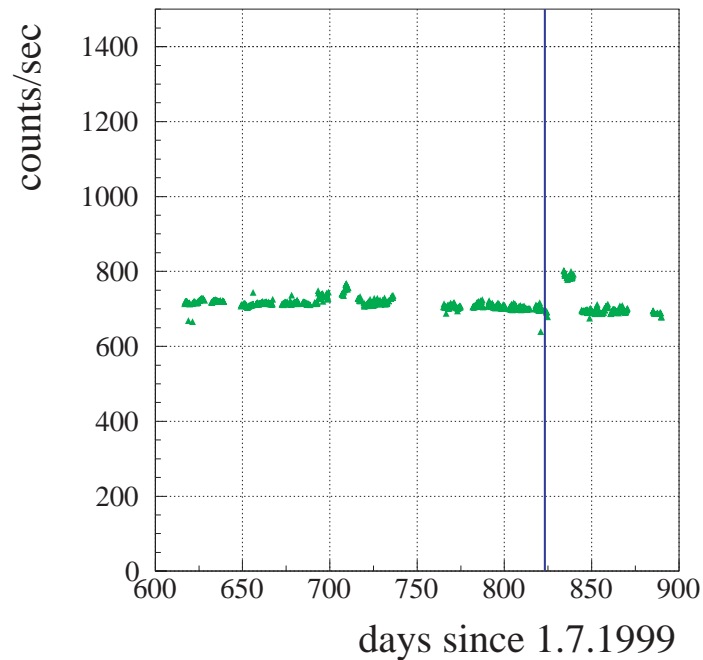


**Figure A.1:** Anti-Compton counting rate AC

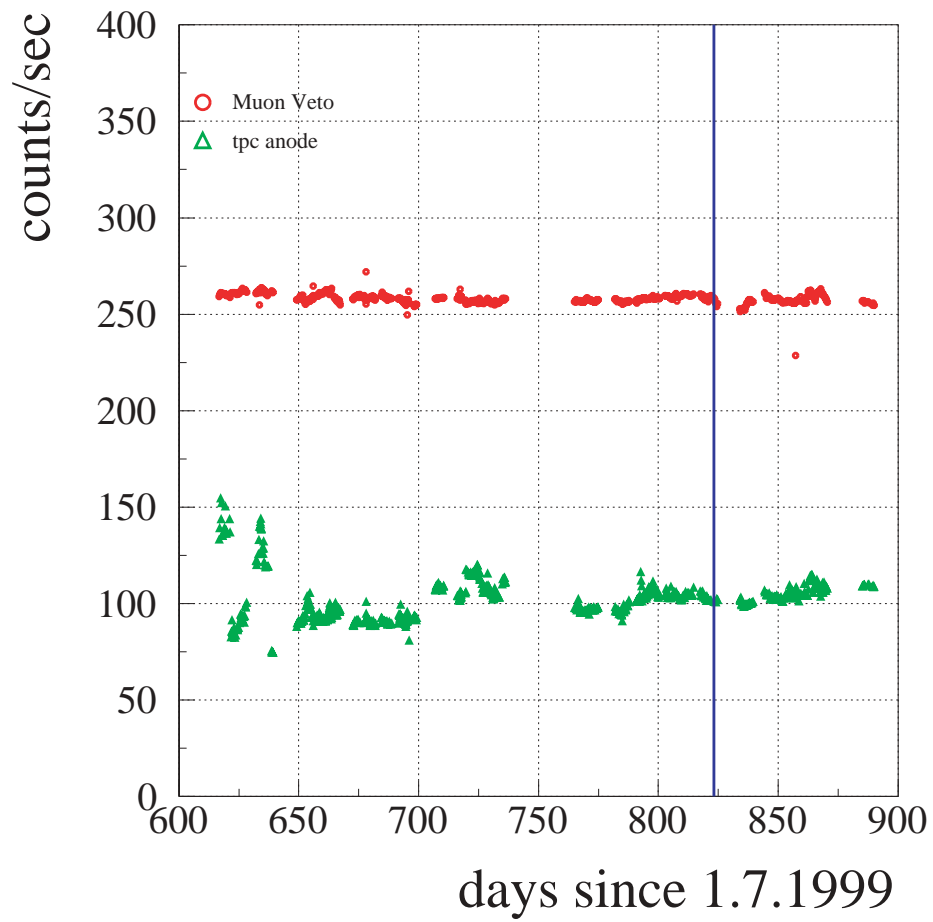


**Figure A.2:** Muon counting rates.

## A.2 The neutrino hardware trigger

The hardware trigger counting rates for the TPC anode signal, vetoed by the muon veto (0.86 Hz), and the anti-Compton AC (0.5 Hz) are shown. The events was written to disc with 0.14 Hz.

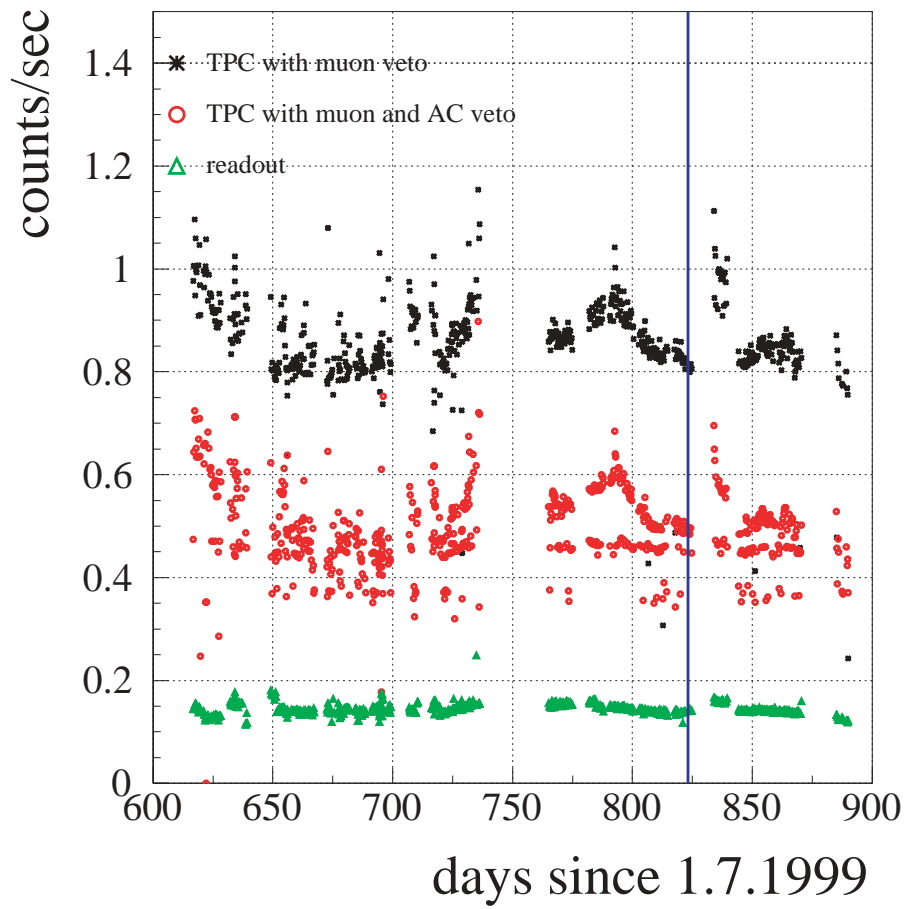
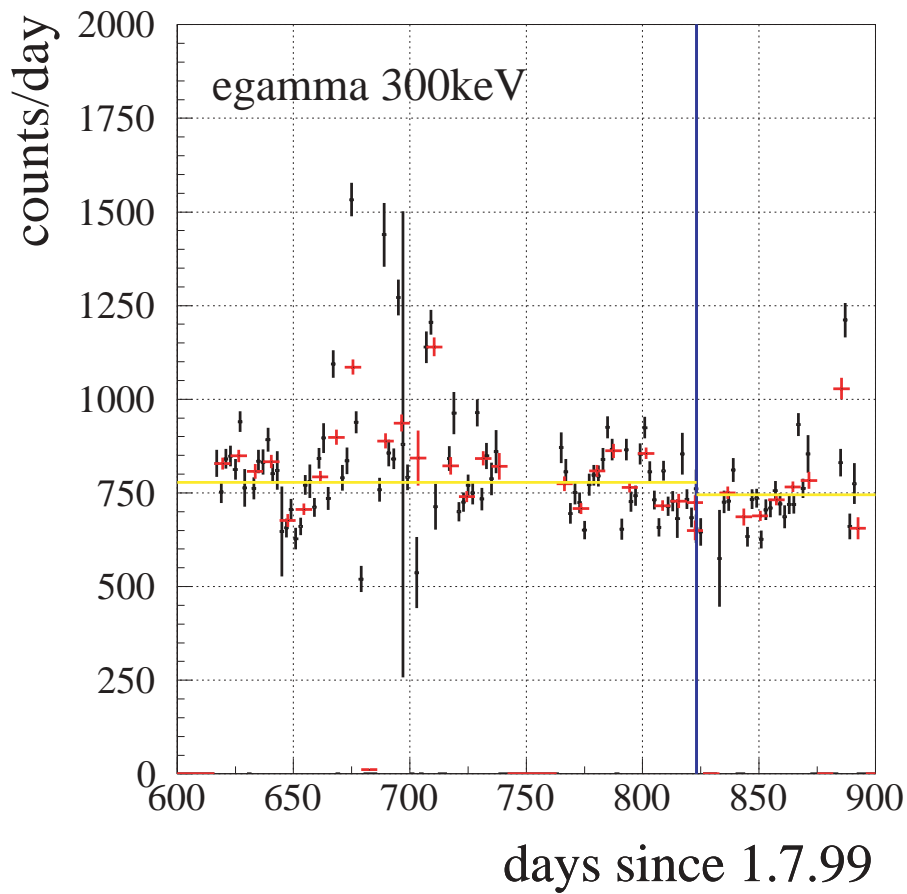


Figure A.3: Neutrino trigger counting rates

### A.3 Compton electrons

The counting rate of Compton electrons in the TPC for a neutrino trigger run was stable during the measurement, both at 300 and at 700 keV (threshold). The counting rate of electrons with  $\gamma$ -rays was found to be 770 counts per day at 300 keV and 320 counts per day at 700 keV.



**Figure A.4:** Electron with  $\gamma$ -ray above 300 keV.

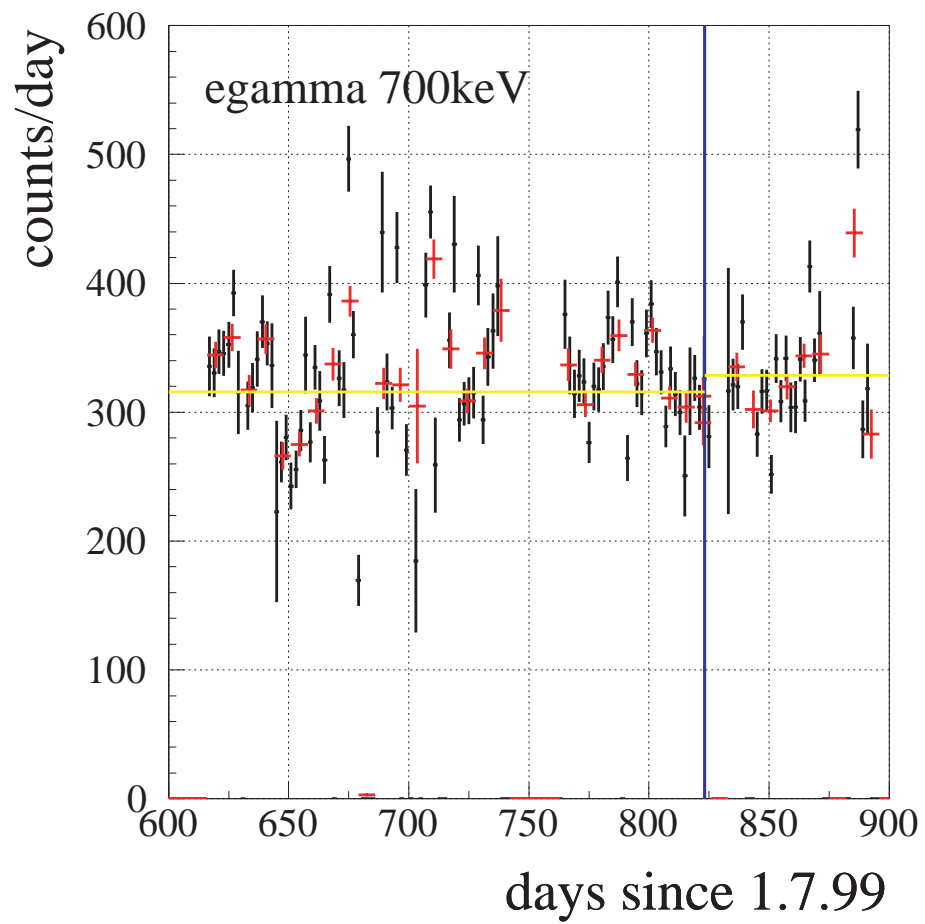


**Figure A.5:** Electron with  $\gamma$ -ray above 700 keV.

#### A.4 Electrons crossing the anode

Electrons crossing the anode plane, or the so-called biblob events, are an important contribution in the real data. The counting rate was found to vary from 10000 counts per day at 300 keV to 4000 counts per day at 700 keV. The time evolution is not stable, however.

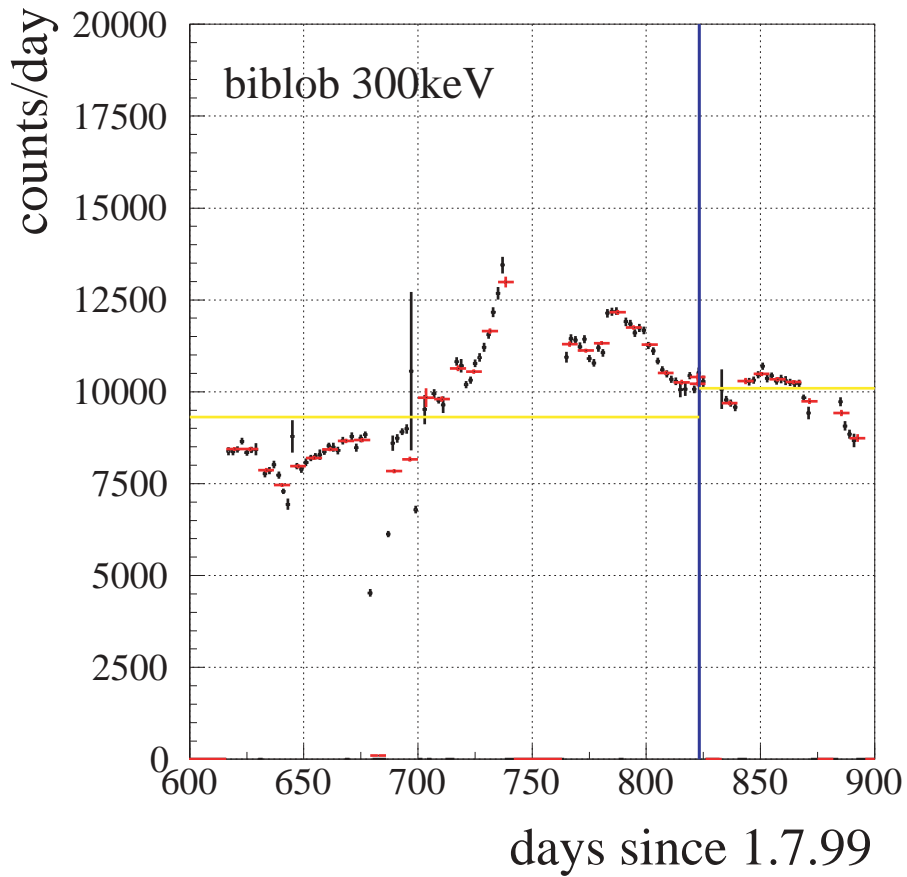


**Figure A.6:** Anode crossing filter at 300 keV.

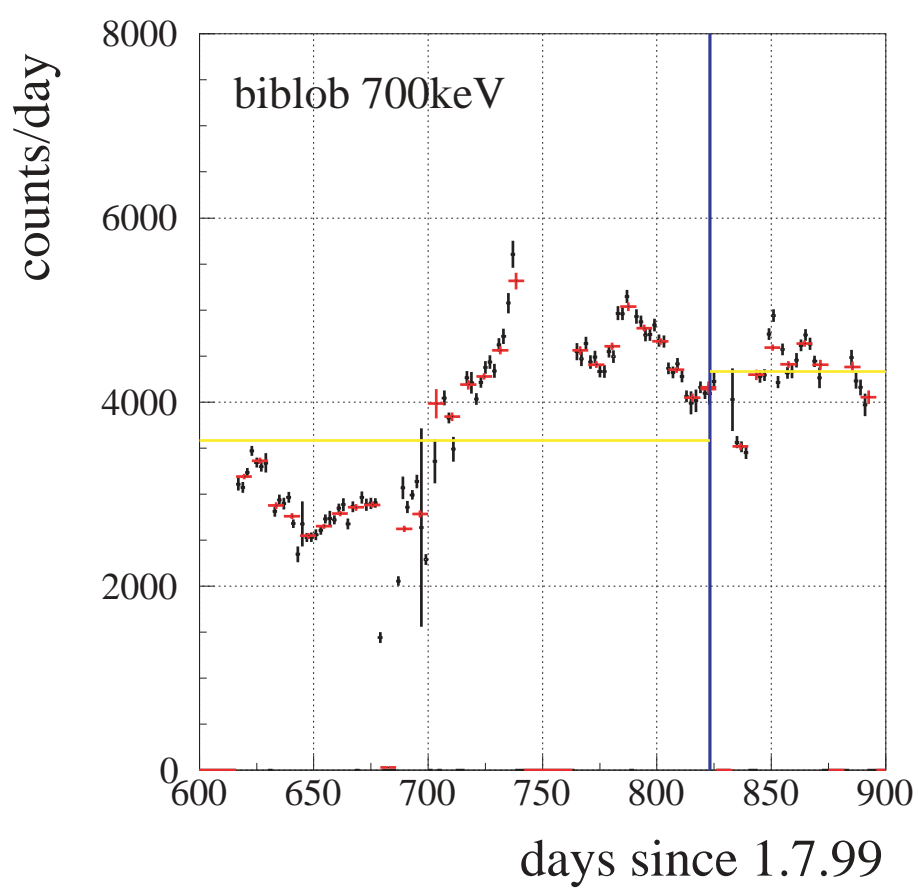
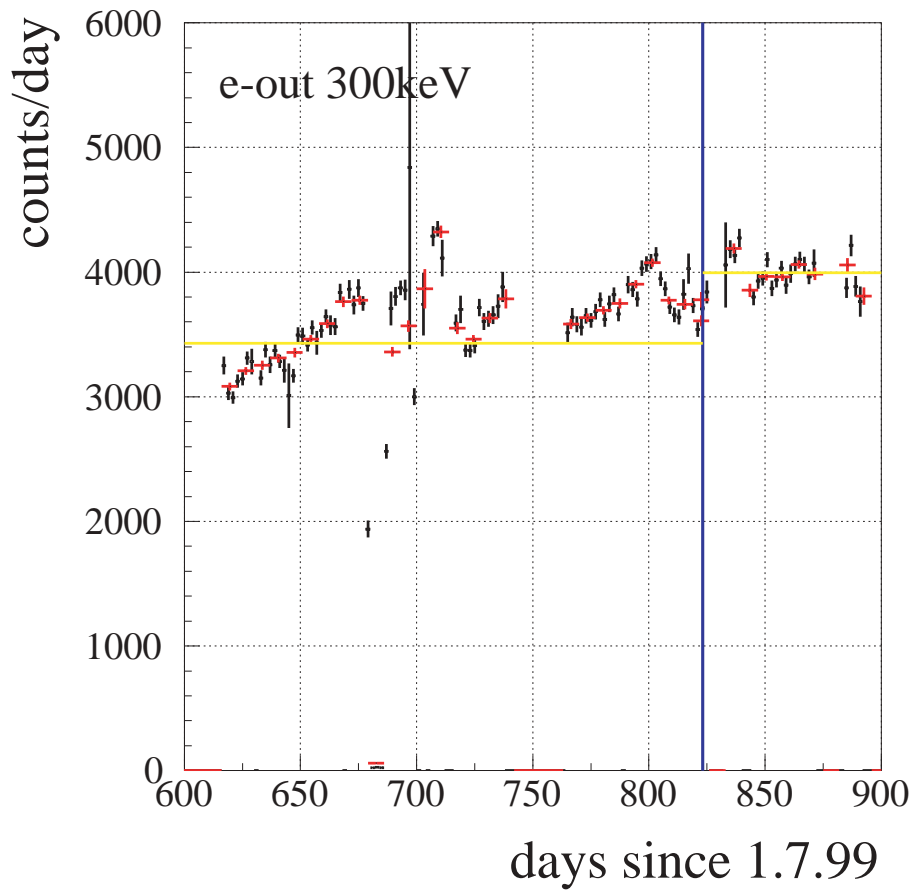


Figure A.7: Anode crossing filter at 700 keV.

### A.5 Electrons outside the containment

Electrons outside the containment are showing an increasing counting rate, similar to the accepted events. There are 3000-4000 electrons at a 300 keV threshold, and still 1000-1200 electrons above 700 keV.



**Figure A.8:** Electron outside the fiducial volume above 300 keV.

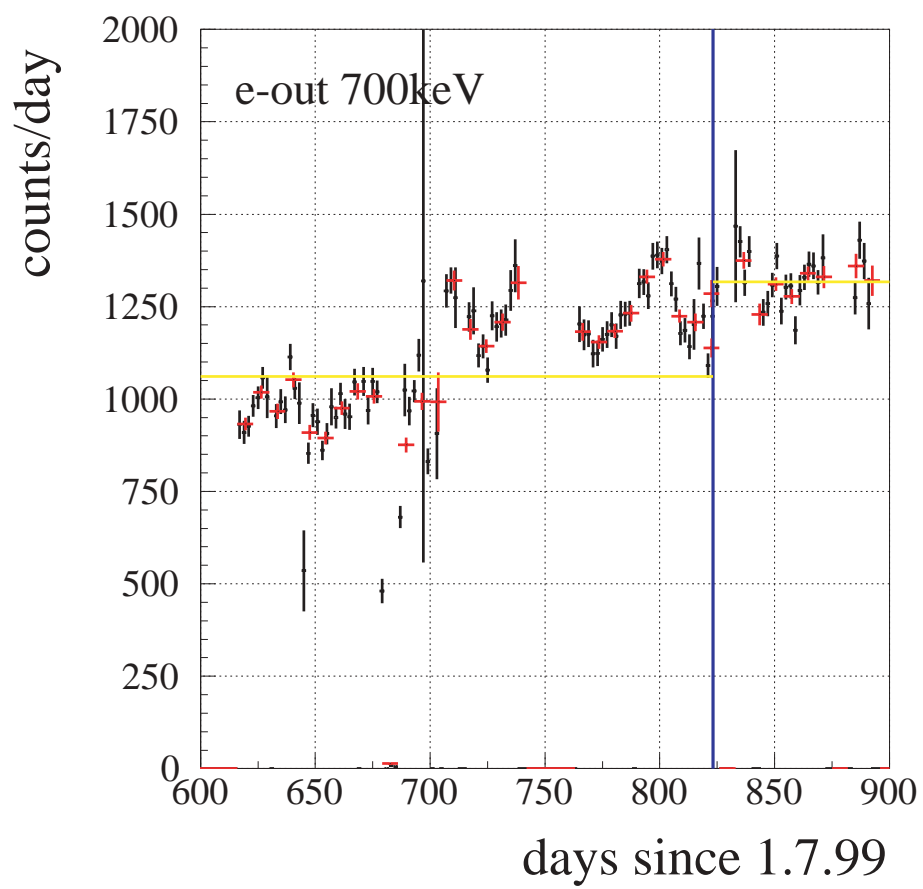


**Figure A.9:** Electron outside the fiducial volume above 700 keV.



## *APPENDIX B: Parameter optimisation*

The tracking parameters have to be tuned to the actual pressure in the TPC. Higher pressure means more multiple scattering but shorter tracks. For the data taking, the TPC was under 3 bar, which was the optimal pressure with respect to the track length and multiple scattering. However, the angular resolution at low pressure is improved due to less multiple scattering. The tracking is disturbed by the noise, especially by noise bands and pick-up inductions near the true track. In the automatic tracking, the noise produces fake starts, leading to completely wrong vertices. To reduce the noise a Fourier filter was used. The disadvantage of the frequency filtering is the loss of information in the signal, such as smearing and broadening the track. The Monte Carlo was tuned to the real data and noise, an important requirement for the optimisation of the tracking program. If the threshold IXYCUT is too high, the most faint part of the physical track, e.g. the vertex, will be below the threshold. If the threshold is too low, the electronic noise disturbs the track reconstruction. This degrades the angular resolution very fast. Therefore, carefully tuning the tracking parameters is crucial. For this task, we have first to ask about the criteria of the parameter optimisation. The angular resolution in space and the vertex resolution are the most important, followed by the acceptance. The parameters, summarized in 4.2 are important for the track reconstruction and direction fit.

In the following section, only a part of the parameters will be described and discussed. All parameters are tuned with the same method: for a given range of a parameter, e.g. RLENGTH varying from 4 strips up to 12 strips with a 1 strip step size, 3000 electrons were generated with GEANT and tracked with the corresponding parameter value. The resulting ntuples - one for each parameter value - were then analysed and the vertex and angular resolutions calculated. The resolution was determined as a function of the parameter, and a polynomial fit was applied to obtain the minimum value, if possible. In most cases, the function was constant or only weakly depending on the parameter. This stability is an important feature of the tracking program, because a quickly changing resolution would be difficult to handle in the true data. There are still improvements expected but, due to the stability, it will be in the order of a few percent only.

## B.6 Step size: RSTEP

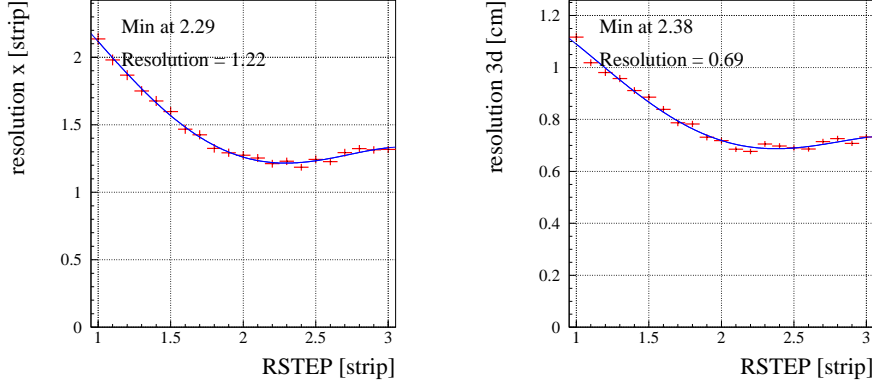


**Figure B.1:** Vertex resolution in  $x$  (left) and in space (right).

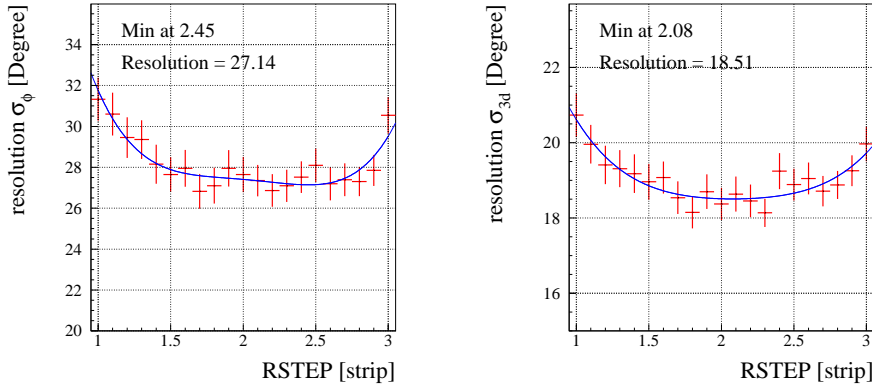


**Figure B.2:** Angular resolution as a function of the step size  $RSTEP$ . The left side shows the angular resolution in  $\phi_{\text{det}}$  and on the right side the spatial angular resolution is shown. Both resolutions are averaged over 0.3 MeV and 1.3 MeV. One strip corresponds to 0.35 cm, whereas the scaling to the  $z$  direction is taken into account.

The  $RSTEP$  parameter is the step size between two points in the track reconstruction. The range for the optimisation procedure was from 1 strip up to 3 strips, with a 0.1 strip step size. This range is sufficient, because a smaller step size is meaningless - we have a 1 strip binning in our detector - and for large sizes, the fine tuning is not possible. Remember, the width of a track is in the order of a few strips only. Figure B.1 (left side) shows the vertex resolution in  $x$  as a function of the parameter  $RSTEP$ . The res-

olution increases with decreasing step size due to the detector binning. The best vertex resolution in  $x$  was obtained at a step size of 2.3 strips, and a compatible 2.4 strips step size for the vertex resolution in space. The next figure B.2 shows the angular resolution for the same parameter values. The region around the step size 2 is more or less flat and the resolution is  $4^\circ$  better than at the borders. The variation of the resolution in the flat region is small; therefore, the step size 2 was selected.

### B.7 Length of the rotating box: RLENGTH

The parameter RLENGTH is, like RSTEP, responsible for the track reconstruction. It is the length of the rotation box at the position of the actual track point. All  $z$ -bins within the box of length RLENGTH in a given direction are summed up and compared. The next track point is reconstructed by going in the direction of the box with the largest contents. The distance to the next point is RSTEP, the parameter from the previous section. The

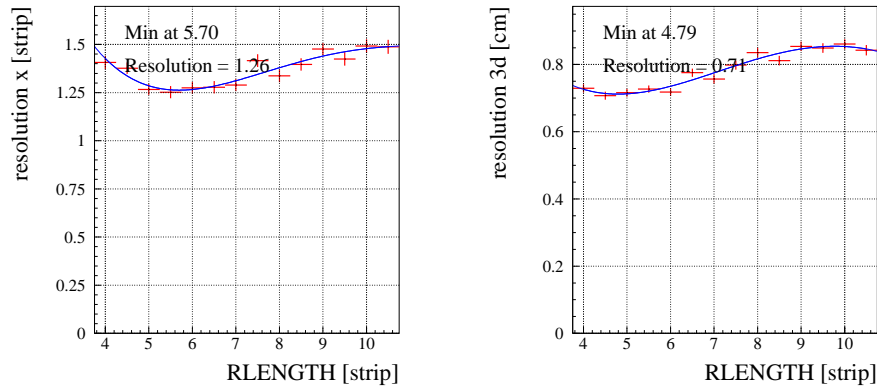


**Figure B.3:** Vertex resolution in  $x$  (left) and in space (right).

width of the box is fixed to 2 strips, no optimisation was made. Maybe there is still some improvement possible. Figure B.3 contains the vertex resolutions in  $x$  and in space, both with a minimum between 5 and 6 strips. With a small box length, only the neighbourhood of the actual position is taken into account for the direction to the next point. At higher values for the length, the direction determination is disturbed mainly by noise and complicated track topologies, like tracks covering themselves or going back in both projections. Figure B.4 show the dependency of the angular resolution for the angle  $\phi_{\text{det}}$  and in space. The parameter RLENGTH was set to 6 strips in the final tracking process.

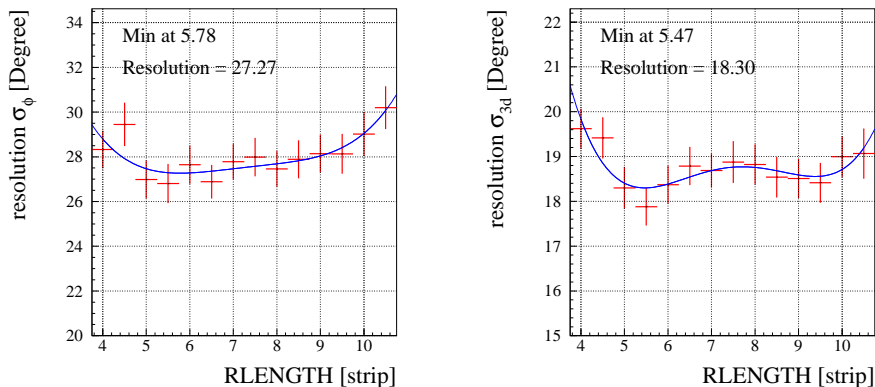


**Figure B.4:** Angular resolution as a function of the *RLENGTH* parameter. The left side shows the angular resolution in  $\phi_{\text{det}}$  and on the right side the spatial angular resolution is shown. Both resolutions are averaged over 0.3 MeV and 1.3 MeV. One strip corresponds to 0.35 cm, whereas the scaling to the *z* direction is taken into account.

## B.8 Reconstruction threshold: *IXYCUT*

The parameter *IXYCUT* is used to control the reconstruction of the event in 3 dimensions. In the event-display, shown in figure B.5, two bands in *x* and *y* are marked with lines. One band corresponds to one bin in the *z* direction. In the picture, the band is made larger for visibility. For each band, only the strips with amplitudes above the threshold *IXYCUT* are used to reconstruct the event. In band A, the *x*-strips close to the number 165 are above the threshold, or 120 for the *y*-strips respectively. After the combination of the strips of this band, a visualisation in the *xy*-projection is possible, as seen the event-display. The reconstructed event band A is localised in the *xy*-projection in a small region. The second band B has a larger range in the *x*-strips and *y*-strips, as shown in the display. In this band, almost 20 strips are above the threshold *IXYCUT*, and therefore more combinations have to be performed for the reconstruction. The resulting region in the *xy*-projection consequently is larger; hence, a rectangular box is created, filled with approximately the same amplitude in each pixel. If the threshold is lowered, more strips have to be combined together and the event disappears in the noise. This degrades the angular resolution. On the other hand, having a high threshold to suppress the noise may swallow the signal, especially the vertices. For that reason, the threshold has to be tuned carefully. The parameter *IXYCUT* is only important for the angular fit, the vertex itself is already found by the reconstruction. Thus, we have to study only the angular resolution as a function of the parameter. In figure B.6 we see the resolution of the angle  $\phi_{\text{det}}$  (left plot), and the angular resolution in space (right plot). Both resolutions have a minimum close to 60 mV, increasing at

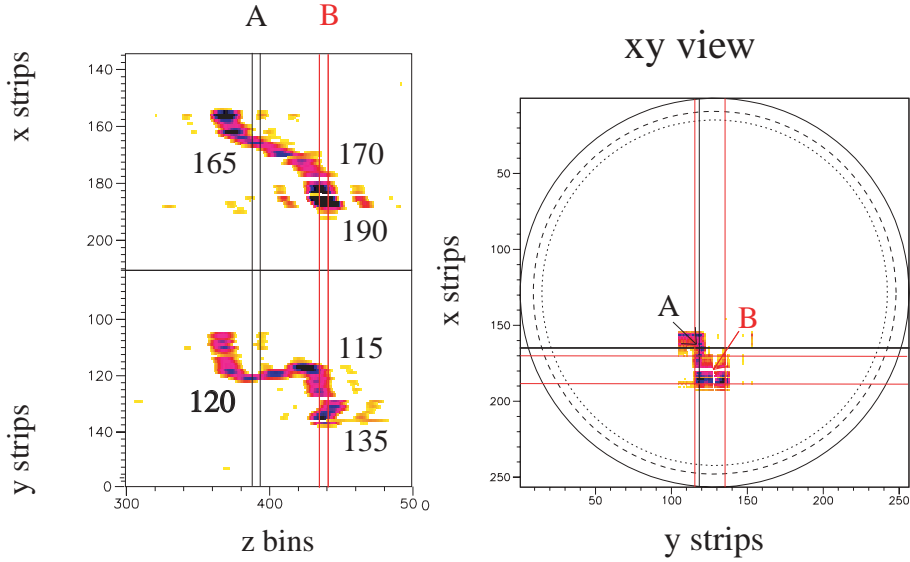


**Figure B.5:** Reconstruction of the event in 2 dimensions.

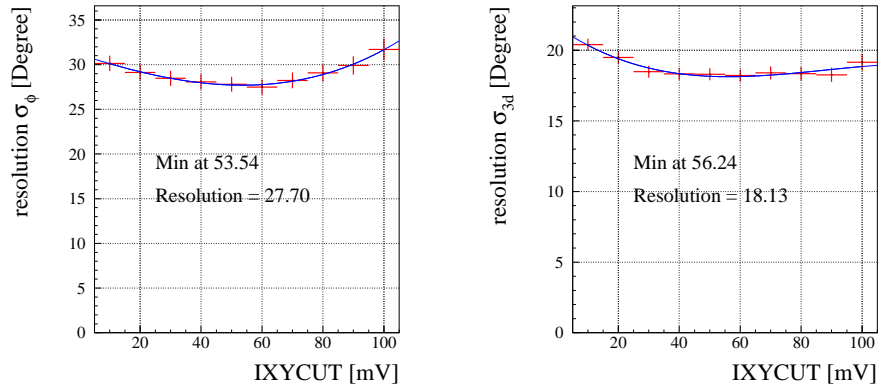


**Figure B.6:** Angular resolution as a function of the reconstruction parameter IXYCUT. The plot on the left side shows the angular resolution in  $\phi_{\text{det}}$  and on the right side the spacial angular resolution is shown. Both resolutions are averaged over 3 MeV and 1.3 MeV. One strip corresponds to 0.35 cm, whereas the scaling to the z direction is taken into account.

lower and higher values. The range between 0 mV and 100 mV was scanned with a 10 mV binning.

### B.9 Fit radius: RCIRCLE

With the parameter RCIRCLE, the radius of the direction fit can be changed. Only the amplitude  $A_{xyz}$  of pixel-elements with a distance  $d$  smaller than RCIRCLE from the vertex position are summed up to build the  $\chi^2$ :

$$\chi^2 = \sum d^2 * A_{xyz} \quad . \quad (\text{B.1})$$

Other  $\chi^2$  definitions was tested, especially to reduce the influence of noise near the vertex, all without significant improvement. MINUIT was used to make the straight line fit, as explained in section 4.2. As for the threshold IXYCUT, the vertex position does not depend on the parameter RCIRCLE. Therefore, only the angular resolution as a function of the parameter is analysed. The scan-range starts at 6 strips length and ends at 16 strips, with a 0.5 strip binning. The scaling between the strips and the z-direction is taken into account. For a typical drift time, one strip corresponds to 2-3 z-bins, and the sphere in the xyz picture is deformed to an ellipsoid. If the

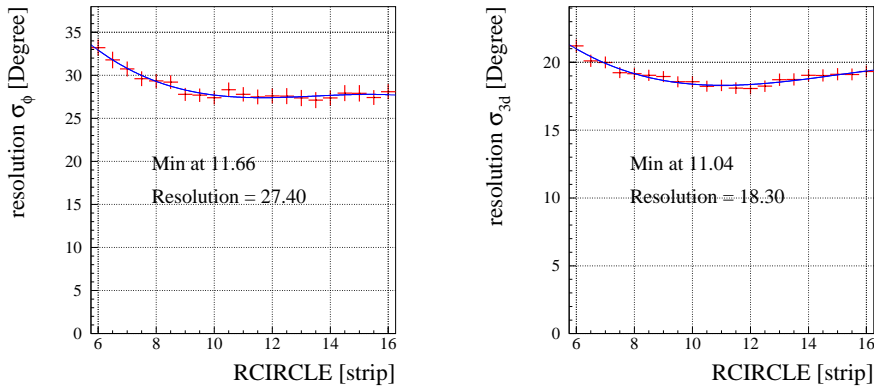


**Figure B.7:** Angular resolution as a function of the fit radius. The plot on the left side shows the angular resolution in  $\phi_{\text{det}}$  and on the right side the spatial angular resolution is shown. Both resolutions are averaged over 3 MeV and 1.3 MeV. One strip corresponds to 0.35 cm, whereas the scaling to the z direction is taken into account.

track reconstruction gives a vertex near the true vertex, then the position is only smeared out due to the track width, corresponding to 4-5 strips corresponding to 1.2 cm. The angular resolution is degraded, if the fit radius is in the order of the track width. For a longer fit radius, multiple scattering becomes the limiting factor for the angular resolution. Electronic noise near the vertex and some rare event topologies are degrading the resolution in addition.

## APPENDIX C: Visual Scanning

### C.10 Comparison between the eye and the automatic classification

The automatic tracking has the two classes for electrons inside (e-in) and outside (e-out) the fiducial volume containment. There is a class for events with an empty projection in  $xz$  or  $yz$ , but there are only very few events fulfilling this condition. In the following, the automatic and visual classification are compared and discussed for e-in and e-out electrons. For electrons e-in the angular distributions are compared and a possible reduction for the visual scanning work is proposed at lower energies. The data used for this comparison are the accepted events after the offline filter, see chapter 3.

#### C.10.1 Electrons outside the containment

Let us start with the study of the e-out events. The electrons outside the fiducial volume have to be rejected because of two reasons:

- An electron crossing the walls deposits a part of its energy outside the TPC. Hence, the energy cannot be determined correctly, leading to a wrong energy spectrum. The energy of an event is important for the kinematical cut.
- Events from outside, crossing the TPC walls, are not due to an neutrino-electron scattering in the TPC gas volume. These events have to be considered as background, and have to be rejected.

Both tracking methods give the same amount of events in the class e-out, 9.5% of the events are classified as e-out by eye, and 8.6% by the automatic tracking respectively. The main questions are:

- How many of the visual e-out electrons are recognised as e-out by the automatic scanning as well? This corresponds to the **efficiency**  $\epsilon$  of

the automatic e-out scanning to find a e-out event of the eye scanning. The efficiency is therefore defined as:

$$\epsilon = \frac{\text{number of visual e-out which are also e-out by tracking}}{\text{number of visual e-out}} . \quad (\text{C.1})$$

- How many of the visual e-in are classified by the automatic tracking as e-in electrons? This corresponds to the **acceptance**  $\alpha$  of the automatic tracking.

$$\alpha = \frac{\text{number of visual e-in which are e-in by tracking}}{\text{number of visual e-in}} . \quad (\text{C.2})$$

The efficiency above 700 keV, as shown in C.1, is around 50%. This means that 40-50% of the visual e-out events are classified as e-out by the automatic tracking, whereas the other 50% are classified mistakenly as e-in. If we ask about the classification by eye of the automatic e-out events, we expect 50% e-out, and vice versa.

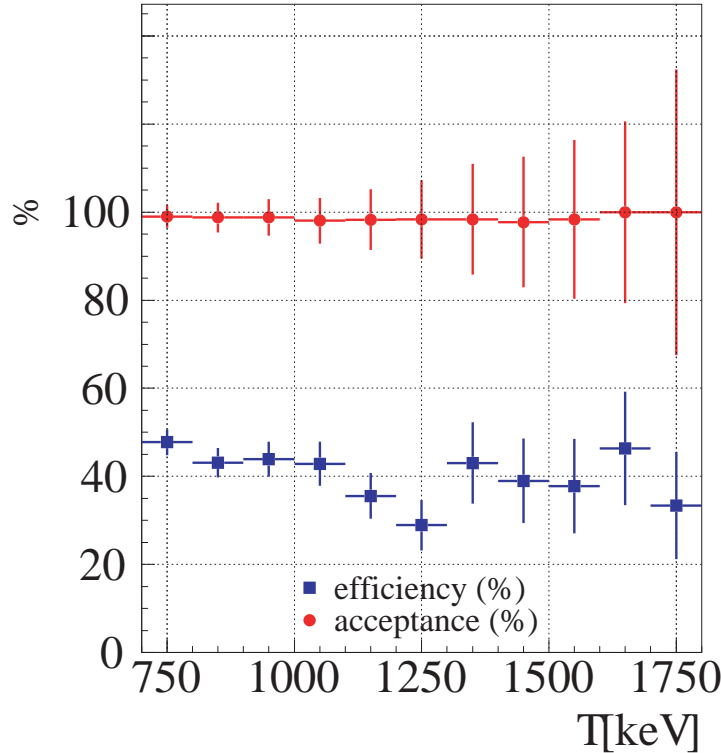


**Figure C.1:** Acceptance and efficiency of the automatic tracking of electrons outside the containment.

A summary of the event classification by eye of the automatic e-out events is given in table C.10. In the class e-strange are the second most events.

This class was used in the visual scanning for all electrons coming from the anode side, without asking for containment.

**Table C.10:** Eye classification of the events identified as e-out by the automatic tracking.

e-out	46.8%
e-strange	19%
muons	6.5%
e-gamma	5.6%
biblobs	5.5%
e-in	3.9%

Almost all of the electrons classified by eye inside the fiducial volume are classified correctly as e-in by the tracking program. This holds for all energies, as documented in figure C.1. Hence, the e-out classification of the automatic tracking does not discard the electrons inside the fiducial volume; only background electrons near the wall are rejected. This is an important feature of the automatic classification. Note that the offline filter eliminated already events outside the containment.

### C.10.2 Electrons inside the containment

Now we have to look at the electrons, which are classified by the tracking inside the fiducial volume. How are those events classified by the visual scanning? In figure C.2 the eye classification of the (tracking) e-in electrons shows, that there are only 30% electron e-in, but more than 50% biblobs. The rest (10%) is classified as electron outside the fiducial volume.

The most important difficulty of the automatic tracking is an electron with two blobs inside the fiducial volume. In this case, the vertex determination is impossible, because the low ionisation vertex does not exist. In 50% of all biblobs, the vertex will be on the wrong side. Consequently, the direction (scattering angle) is completely wrong, and a subsequent selection or rejection with the angle  $\theta_{\text{det}}$  is impossible. Remember, that the biblob electrons are mostly originating from the anode, hence having an angle  $\theta_{\text{det}}$  larger than  $90^\circ$ . In the section 4.2 we motivated a rejection of events with an angle  $\theta_{\text{det}}$  higher than  $100^\circ$ . If we apply this cut on the biblob events with the automatic fitted angle  $\theta_{\text{det}}$ , the biblobs are reduced by 50%. This is compatible with the vertex argument given above.

The advantage of the eye scanning is a much better biblob recognition, which reduces the background events from the anode side significantly.

The automatic tracking could be improved with an additional biblob detection routine. In the actual version of the Monte Carlo program, biblobs are not generated in the strip signals, and the derivative sum of the PM (scirise)

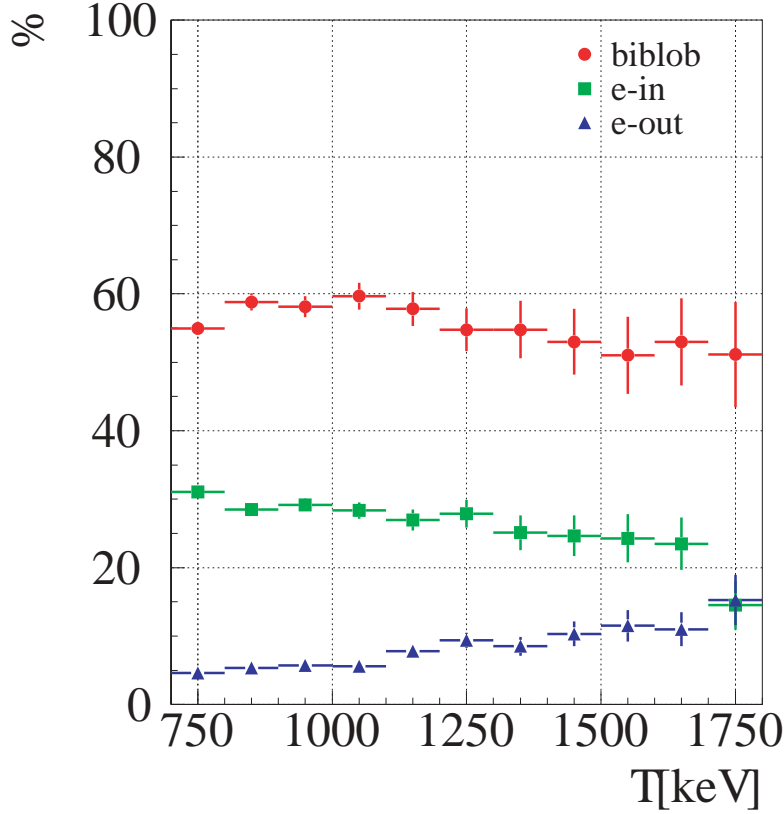


**Figure C.2:** Electrons classified as inside the containment by the track reconstruction, seen by the eye

is not available. Therefore, the determination of acceptance and efficiency of the new biblob recognition would be difficult.

An alternative would be the use of the visual information, such as vertex position and classification, for the automatic direction fit. By replacing the visual angular fit with the automatic version, at the visual vertex position, a better angular resolution is expected. Afterwards, the acceptance can be determined with a standard Monte Carlo simulation. This method is restricted to energies above 700 keV, however.

### C.11 Angular distributions

In the visual scanning, the angles  $\phi_{\text{det}}$  and  $\theta_{\text{det}}$  are determined from the projections  $xz$  and  $yz$ , no 3 dimensional fit is performed. This works as follows: In one arbitrary projection, e.g. the  $xz$  projection, a line from the vertex position in the direction of the event is drawn manually. The length

of this line can be chosen freely. The projection on  $z$  gives  $\Delta z$ , and the projection on  $x$  gives  $\Delta x$ . In the remaining projection  $yz$ , the second straight line is drawn with the condition, that the  $\Delta z$  has to be equal in both projections. With the second line,  $\Delta y$  is determined, as illustrated in figure C.3. After the graphical determination of the three directions  $\Delta x$ ,  $\Delta y$  and  $\Delta z$ ,

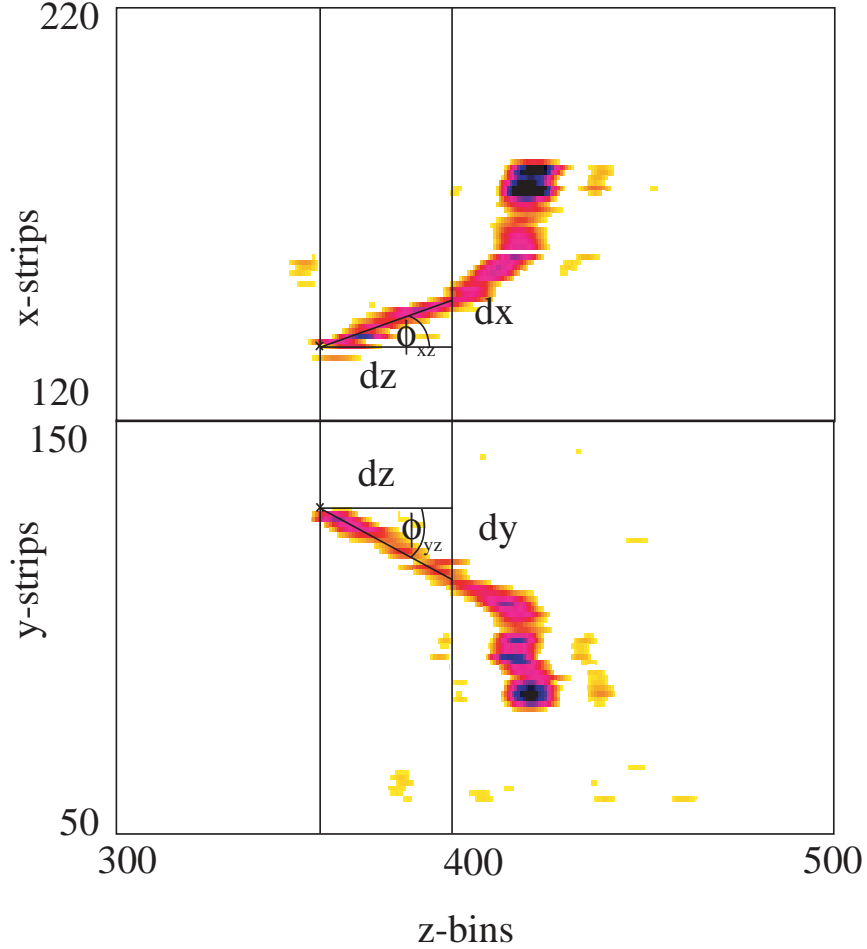


**Figure C.3:** Event display of an electron with a manual vertex and direction fit. The  $dz$  has to be the same in both projections. The angles  $\phi_{xz}$  and  $\phi_{yz}$  are defined from the negative  $z$ -axis.

the angles  $\phi_{\text{det}}$  and  $\theta_{\text{det}}$  are calculated with the following formulas:

$$\phi_{\text{det}} = \arctan \frac{\Delta x}{\Delta y} \quad , \quad (\text{C.3})$$

and

$$\theta_{\text{det}} = \arccos \frac{\Delta z}{\sqrt{\Delta x^2 + \Delta y^2 + \Delta z^2}} \quad . \quad (\text{C.4})$$

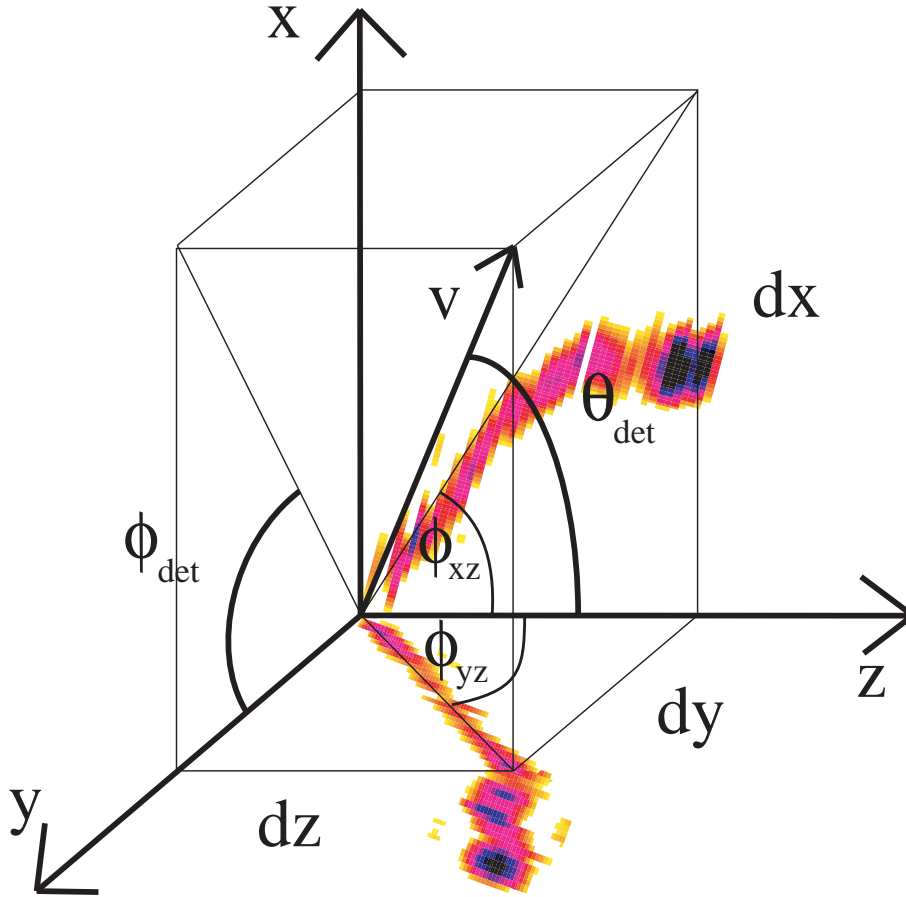


**Figure C.4:** Reconstruction of the angles  $\phi_{\text{det}}$  and  $\theta_{\text{det}}$  from the vector  $\vec{v}$ , given by the coordinates  $\Delta x$ ,  $\Delta y$  and  $\Delta z$ . The length  $\Delta z$  has to be the same for both projections  $xz$  and  $yz$ . The scattering angle is then calculated with the formulas given in the section 4.2 for the automatic tracking.

The resulting angular distributions for the 700 keV reactor ON data is shown in figure C.5, corresponding to 66.3 days effective measurement. The distribution of  $\phi_{\text{det}}$  is peaked at  $45^\circ$ , similar to the automatic tracking.

The detector response is the origin of the structure in the angle  $\phi_{\text{det}}$ . With two different methods, automatic and visual scanning, one obtains a comparable angular distribution. We have explained the structure in the case of the automatic scanning with the ambiguity for events parallel to the  $xy$ -plane. This is the origin of the structure in the eye scanning as well.

To explain the distribution in  $\phi_{\text{det}}$  of the visual scanning, we consider an event parallel to the  $xy$ -plane. At least one of the angles  $\phi_{xz}$  and  $\phi_{yz}$  is close to  $90^\circ$ , as shown in figure C.6. In the visual scanning, the scale is the same for both projections. This aspect ratio is important for the eye scanning,

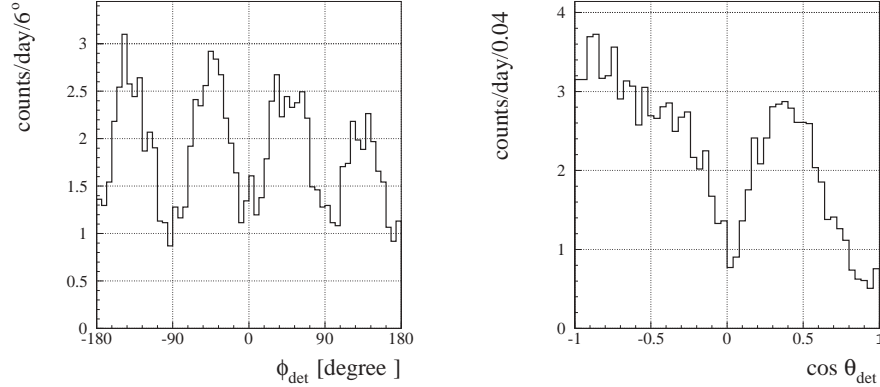


**Figure C.5:** Angular directions in the detector frame. The left plot shows the angle  $\phi_{\text{det}}$  and the right plot the angle  $\text{tzdet}$

because it allows seeing an event in the same scale in  $xz$  and  $yz$ . For events with a small  $\Delta z$ , the second point after the vertex is difficult to obtain. Typically, one tends to choose equally length distances for  $\Delta x$  and  $\Delta y$  in the event-display. Due to the aspect ratio, the two distances  $\Delta x$  and  $\Delta y$  are the same. With the formula C.3, the angle  $\phi_{\text{det}}$  becomes:

$$\phi_{\text{det}} = \arctan \frac{\Delta x}{\Delta y} \approx \arctan \frac{\Delta x}{\Delta x} = \arctan 1 = 45^\circ \quad . \quad (\text{C.5})$$

For events parallel to the  $xy$ -plane, the  $\Delta z$  is small, and the two distances  $\Delta x$  and  $\Delta y$  are equal. This leads to a systematic attraction to angles close to  $45^\circ$ , creating the typical structure in the  $\phi_{\text{det}}$  distribution. The angular distribution in  $\cos \theta_{\text{det}}$ , see figure C.5, is not flat. There are at least two times more events coming from the anode side, a possible leftover of the biblob electrons. A full understanding of this distribution is still missing; more scanning of Monte Carlo simulated events is required.

The scattering angle  $\theta$  is calculated for every event with the formula 4.6, given in section of the automatic scanning, and the resulting angular distribution is plotted in figure C.7. The distribution from the visual and automatic scanning are similar, because the underlying angular distributions in  $\phi_{\text{det}}$  and  $\theta_{\text{det}}$  are similar too.

## C.12 Filtering for the visual scanning

The automatic tracking, including the vertex reconstruction and direction fit, could be used as a filter for the visual scanning at lower energies. This would reduce the number of events to be scanned, and hence making it possible to access the low energy region for the eye scanning. The efficiency

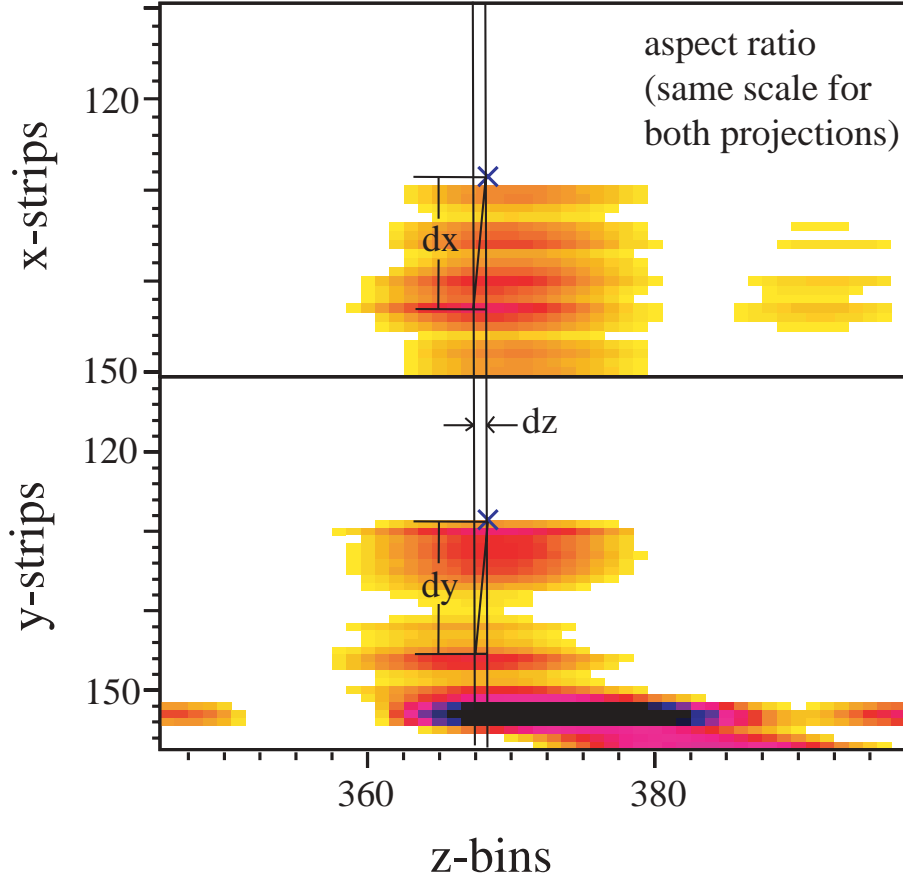


**Figure C.6:** Display of an event parallel to the  $xy$ -plane, with visual vertex determination and angular fit. The  $\Delta z$  for this event is small, making it difficult to place the points for  $\Delta x$  and  $\Delta y$  correctly. The aspect ratio in the visual scanning mode is the same for both projections, per default.

$\epsilon$  to recognise an electron coming from the anode side - this means with an angle  $\theta_{\text{det}}$  larger than  $90^\circ$  - with the automatic tracking is defined as:

$$\epsilon^{100} = \frac{\text{Number of visual e-in with } \theta_{\text{det}}^{\text{vis}} > 90 \text{ and } \theta_{\text{det}}^{\text{auto}} > 100}{\text{Number of visual e - in with } \theta_{\text{det}}^{\text{vis}} > 90} . \quad (\text{C.6})$$

The angle from the visual scanning is indexed with "vis", whereas the automatic one with "auto". In the formula C.6, the efficiency at the angle  $100^\circ$  is given as an example, while the efficiencies for the other angles are defined analogous.

In figure C.8, the efficiency is plotted as a function of the angle  $\theta_{\text{det}}^{\text{auto}}$  for a fixed visual angle  $\theta_{\text{det}}^{\text{vis}}$  ( $90^\circ$ ). The efficiency was found to vary from 80% at  $100^\circ$ , 50% at  $120^\circ$ , to 30% at  $140^\circ$ . By decreasing the angle  $\theta_{\text{det}}^{\text{auto}}$ , hence increasing the opening angle of rejection, the number of electrons from the anode becomes larger, and consequently the efficiency is higher. As a result,

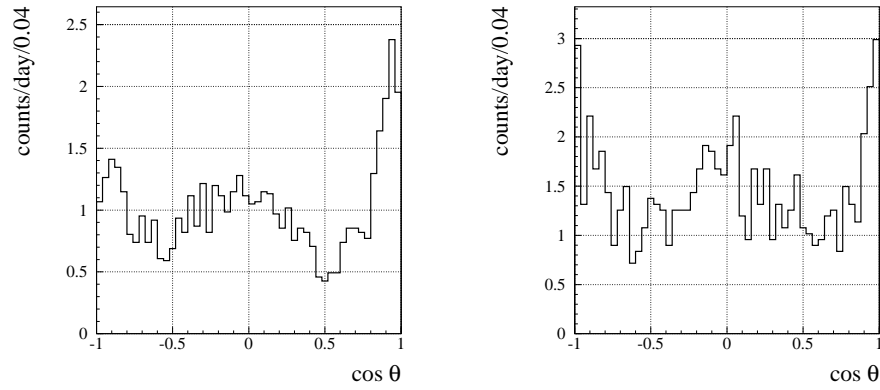


**Figure C.7:** Scattering angle for reactor ON (left) and reactor OFF (right).

we can recognise and eliminate electrons from the anode side with a high efficiency (80%) for angles  $\theta_{\text{det}}^{\text{auto}}$  around  $100^\circ$ - $110^\circ$ .

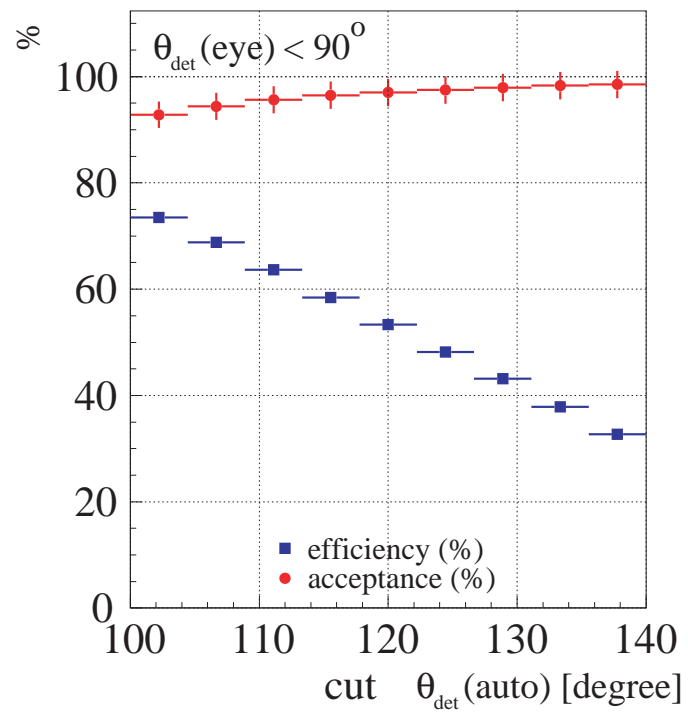


**Figure C.8:** Acceptance and efficiency as a function of  $\theta_{\text{det}}^{\text{auto}}$ .

This encourages the use of an angular filter for the visual scanning, based on the automatic tracking. For that purpose, we have to study the acceptance of the filter. The acceptance is defined by

$$\alpha^{100} = \frac{\text{Number of visual e-in with } \theta_{\text{det}}^{\text{vis}} < 90 \text{ and } \theta_{\text{det}}^{\text{auto}} > 100}{\text{Number of visual e-in with } \theta_{\text{det}}^{\text{vis}} < 90} . \quad (\text{C.7})$$

This formula uses the same naming scheme as above. The acceptance is the fraction of electrons from the cathode side, which are not rejected by the angular cut on  $\theta_{\text{det}}^{\text{auto}}$ . The acceptance is 90% for  $\theta_{\text{det}}^{\text{auto}} = 100^\circ$ , and 100% at  $140^\circ$ . The efficiency is better at low cut, but the acceptance is worse. Good efficiency means bad acceptance, and vice versa.

For a successful filter, we have to define our objective first. If we want to reduce the amount of data to scan considerably, then we should use a cut around  $100^\circ$ , with a still reasonable acceptance around 90%. On the other hand, if we want no loss in the signal, then a high acceptance and therefore a high cut angle around  $140^\circ$  with a low efficiency is the answer. This filter has not been used yet, but it would be a good possibility to access the data at low energies by the visual scanning method. The acceptance is well known, and the neutrino electron counting rate of the Monte Carlo prediction could be corrected easily.

Other filters were investigated, without similar success. A cut on the angle  $\theta$  is not favoured, because the filter should not go directly on the kinematics of the scattering process. The acceptance in this case was reduced significantly.

## APPENDIX D: BIBLIOGRAPHY

- [1] **K. Fujikawa, R. Schrock**, *Phys. Rev. Lett.* **45** (1980) 963
- [2] **Ch. Weinheimer**, *Direct neutrino mass experiments Proceedings XX-th International Conference of Neutrino Physics and Astrophysics (May 25-30, 2002, Munich, Germany) to be published.*
- [3] **V.M. Lobashev et. al**, *Phys. Lett.* **B460** (1999) 227
- [4] **F. Ould-Saada**, *Electromagnetic Properties of Neutrinos. PSI Proceedings 96-03 (1996) 191*
- [5] **MUNU Collaboration, Brogгинi et al**, *Proposal. A gas detector to measure the  $\bar{\nu}_e$  magnetic moment at a nuclear reactor. Nucl. Instr. Meth. A* **311** (1992) 319-326
- [6] **P. Vogel und J. Engel**, *Phys. Rev.* **D39**(1989) 3378
- [7] **F. Reines, H.S. Gurr and H.W. Sobel**, *Phys. Rev. Lett.* **37** (1976) 315
- [8] **I.I. Gurevitch et al**, *I.V Kurtchatov Institute of Atomic Energy, 123182 Moscow, Russia, 1991.*
- [9] **G.S. Vidyakin et. al**, *JETP Lett.* **49** (1989) 740
- [10] **A.I. Derbin**, *JETP Lett.* **57** (1993) 76
- [11] **The TEXONO Collaboration (H.B.Li et al.)**, *Phys. Rev. Lett.* **90** (2003) 131
- [12] **J. Pulido, A.M. Mourao**, *Phys. Rev.* **D57** (1998) 1794
- [13] **J.F. Beacom, P. Vogel**, *Phys. Rev. Lett.* **83** (1999) 5222
- [14] **J. Morgan**, *Phys. Lett.* **102B** (1990) 559
- [15] **R. Barbieri and R. Mohapatra**, *Phys. Rev. Lett.* **61** (1988) 27
- [16] **G. Raffelt**, *Phys. Rev. Lett.* **64** (1990) 2856

- 
- [17] **Z. Daraktchieva et al.**, *Limits on the neutrino magnetic moment from the MUNU experiment Submitted to Phys. Lett. B*
- [18] **MUNU Collaboration, C. Amsler et al**, *The MUNU Experiment, General Description, NIM A 369 (1997) 115-129*
- [19] **MUNU Collaboration, M. Avenier et. al**, *Sub MeV particles detection and identification in the MUNU detector. Nucl. Instr. Meth. A 482 (2001) 408-424*
- [20] **G. Charpak et. al**, *Nucl. Instr. Meth. 62 (1968) 235*
- [21] **F. Sauli**, *Principles of Operation of Multiwire Proportional and Drift Chambers. CERN 77-09, 1977. Publ. Ref.: Experimental techniques in high-energy nuclear and particle physics T Ferbel World Sci., Singapore, (1991)79.*
- [22] **L.G. Christophourou, J.K. Olthoff and M.V.V.S. Rao**, *J. Phys. Chem. Ref Data 25 (1996) 1341*
- [23] **Pure Gas, Inc. San Luis Obispo, California (USA) Monotorr Purifiers**
- [24] **Patrick Janneret**, *Time Projection Chambers and detection of neutrinos. Thesis, Physics Departement, Neuchâtel University, 2001*
- [25] **G.F. Reinking, L.G. Christophourou and S.R. Hunter**, *J Appl. Phys. 60 (1986) 499*
- [26] **H.A.Van Sprang et. Al**, *Chemical Physics 35 (1978) 51*
- [27] **P. Giarritta**, *Aufbau eines Flash-ADC Auslesesystems für die Messung des magnetischen Moments des Neutrinos Diploma thesis, University of Zurich (1994)*
- [28] **S. Iseli**, *Messung und Studium von Elektronenspuren in einer CF<sub>4</sub> Zeitprojektionskammer. Diploma thesis, University of Zurich (1996)*
- [29] **O. Link**, *Entwicklung des Triggersystems für das MUNU Experient. Diploma thesis, University of Zurich (1998)*
- [30] **Cedric Cerna**, *MUNU: Etude de la diffusion neutrino-électron. Thèse à l'Institut des Sciences Nucléaires de Grenoble, 2000.*
- [31] **THORN EMI Electron Tubes Limited.**, *200 mm 8" hemispherical Photomultiplier Type 9354. Electron Tubes Limited. Bury Street Ruislip Middlesex HA4 7TA England.*
- [32] **Cascade. Users'Guide**, *CERN ECP/FEX-CA 96-1, Revision 2.01, March 1996. <http://cascade.cern.ch/Documentation>*

- 
- [33] **Creative Electronics Systems S.A**, *The RCB 8047 VME Read-Out Control Board. User's Manual*. Creative Electronics Systems S.A., 1994.
- [34] **STRUCK**, *DL362/DL363 Flash ADC Modules, Technical Manual*. Dr. B. Struck, Tangstedt/Hamburg.
- [35] **LeCroy**, *Operator's Manual. Model 2366 universal programmable logic module*. LeCroy, April 1996.
- [36] **LeCroy**, *Scaler 2551 and Latching Scaler 4434*. LeCroy, 1983
- [37] **Xilinx**, *The Programmable Logic Data Book*. 2100 Logic Drive, San Jose, CA 95124, 1994.
- [38] **Xilinx**, *XACTStep Foundation Series. Quick Start Guide*. 2100 Logic Drive, San Jose, CA 95124, 1997.
- [39] **Jacob Lamblin**, *Performances du détecteur MUNU et Perspectives en vue de la détection des Neutrinos solaires*. Thèse à l'Institut des Sciences Nucléaires de Grenoble, 2002.
- [40] **Encyclopédie des gaz**, *L'Air liquide*
- [41] **Function Minimization and Error Analysis**, *CERN Program Library Long Writeup D506 Computing and Networks Division, CERN Geneva, Switzerland*
- [42] **Oxisorb filter by Messer Griesheim GmbH**, *47805 Krefeld, Germany*
- [43] **A. Tadsen**, *Angular resolution in MUNU*. Internal note. INFN Padova (1997).
- [44] **Detector Description and Simulation Tool**, *CERN Program Library Long Writeup W5013 Application Software Group, CERN Geneva*
- [45] **B.D. Wilkins et al.**, *Phys. Rev.* **C14** (1976) 1832
- [46] **Ch. Straede et al.**, *Nuclear Physics* **A462** (1987) 85
- [47] **M.F. James**, *Journal of Nuclear Energy* **23** (1969) 517
- [48] **K. Schreckenbach et al.**, *Phys. Letters* **B99** (1981) 251
- [49] **K. Schreckenbach et al.**, *Phys. Letters* **160B** (1985) 325
- [50] **A.A. Hahn et al.**, *Phys. Letters B* **218** (1989) 365
- [51] **F. von Feilitsch et al.**, *Physics Letters* **118B** (1982) 162
- [52] **J.L. Vuilleumier et al.**, *Physics Letters* **114B** (1982) 298

- 
- [53] **K. Gabathuler et al.**, *Physics Letters* **138B** (1984) 449
  - [54] **J.-F. Cavaignac et al.**, *Phys. Letters* **B148**, (1984) 387
  - [55] **G. Zacek et al.**, *Phys. Rev. D* **34** (1986) 2621
  - [56] **B. Achkar et al.**, *Nuclear Physics B* **434** (1995) 503
  - [57] **V.I.Kopeikin, L.A. Mikaelyan and V.V. Sinev**, *Phys. of Atomic Nuclei* **60** (1997) 172
  - [58] **C. Amsler et al.**, *A new measurement of the  $\bar{\nu}_e e^-$  elastic cross section at very low energy* *Phys Lett. B* **545** (2002) 57
  - [59] **G.J. Feldman and R.D. Cousins**, *Phys. Review D* **57** (1998) 3873
  - [60] **Z. Daraktchieva**, *Thesis, University of Neuchatel, in preparation*

## *ACKNOWLEDGEMENT*

This thesis is the result of four years of work whereby I have been accompanied and supported by many people. It is a pleasant aspect that I have now the opportunity to express my gratitude to all of them.

I am deeply indebted to my supervisor Claude Amsler whose help, stimulating suggestions and encouragement helped me in all the time of research for and writing of this thesis. I am also very grateful to Jean-Luc Vuilleumier from the University of Neuchâtel whose overly enthusiasm and integral view on research has made a deep impression on me.

I am bound to Jose Busto from the University of Neuchâtel who kept an eye on the progress of my work and who always was available when I needed his advices. Especially the many discussions and the interactions with him had a direct impact on the quality of this thesis.

I am very indebted to Henk Pruys for his strict and extensive comments and for carefully reading the manuscript. I would like to thank him for our many discussions and providing me advices and tips that helped me in staying on the right track.

I would like to acknowledge with much appreciation all my colleagues from the University of Neuchâtel who substantially contributed to the development of this work, namely Zori Daraktchieva, Frederic Juget and Patrick Jeanneret. I also wish to thank all my colleagues from the MUNU collaboration.

I want to thank all my colleagues from the University of Zürich group at CERN, namely Thomas Speer for his help, interest and valuable hints, but of course also the rest of the group. I am very grateful to Farid Ould-Saada, who was my supervisor during my diploma work on MUNU.

A special thanks goes to Uli for having shared many experiences and thoughts with me throughout the last years and who showed to be a kind, helpful and trustful friend. I would also like to thank Christoph who provided me various bits of knowledge during our many discussions.

I feel a deep sense of gratitude for my father and mother who formed part

of my vision and taught me the good things that really matter in life. I am grateful for my brother Michael for rendering me the sense and the value of brotherhood.

*This thesis was supported by the Swiss National Science Foundation*

## *CURRICULUM VITAE*

Oliver Link  
Born 4. April 1972 in Solothurn  
Citizen of Zürich, Switzerland

### **Education**

- 1979 - 1985 Primary school Solothurn
- 1985 - 1987 Bezirks school Solothurn
- 1987 - 1992 Gymnasium Kantonsschule Solothurn
- 1992 - 1997 University of Zürich, studies of physics (principal subject), mathematics and informatics (subsidiary subjects)
- 1997 - 1998 Diploma work at the European Organisation for Nuclear Research (CERN) in Geneva
- 1999 - 2003 Scientific assistant and PhD student at the University of Zürich and at the European Organisation for Nuclear Research (CERN) in Geneva

### **Qualifications**

- 1992 Matura typus E
- 1999 Diploma in physics (master degree)